Transition-metal dichalcogenides and the scanning tunnelling microscope: the creation and imaging of vacancy defects

A thesis submitted for the degree of

Doctor of Philosophy

by

John Christopher Caulfield

Condensed Matter & Materials Physics

Department of Physics and Astronomy

University College London

England

December 22, 1997

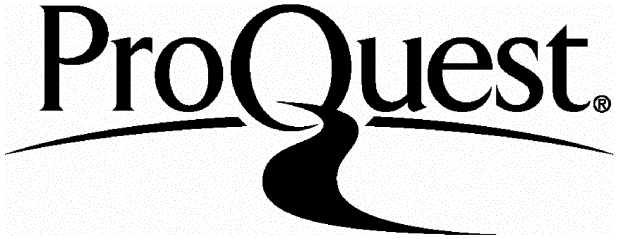

Abstract

This thesis is concerned with the investigation of the creation and imaging of monatomic defects on the surfaces of the transition-metal dichalcogenides with the Scanning Tunnelling Microscope (STM).

The *ab-initio* Projector Augmented Wave (PAW) method is used to study single-atom vacancies on the MoS_2 and $MoTe_2$ surfaces. The presence of the vacancies results in localised electronic states in the surface band-gap which, according to the Tersoff-Hamann approximation, will affect the STM image. Based upon the results, the 'trimer' and monatomic hole defects previously created and observed on WSe_2 and MoS_2 can be explained as monatomic metal and chalcogen vacancies respectively. It is also found that, while the chalcogen vacancy systems behave in a qualitatively similar manner for both MoS_2 and $MoTe_2$, different ordering of the gap-states of the two metal vacancy systems leads to a Jahn–Teller effect in the $MoTe_2$–metal vacancy system. The effects this has on the ground-state atomic and electronic structure are discussed.

The mechanisms behind surface modification using the STM are then examined for the specific case of the MoS_2 surface. The PAW method is used to simulate the MoS_2 surface in the presence of a Mo tip under an electric field; the barriers against extraction of single Mo and S atoms are calculated with and without the field. The temperatures required to extract Mo and S atoms from the surface by the STM tip with an applied bias are found to be around 5100K and 1600K respectively. It therefore seems unlikely that thermal activation alone can explain the atom-transfer process and alternatives are discussed.

Contents

Abstract **1**

List of Tables **6**

List of Figures **8**

Acknowledgements **13**

1 Introduction **14**

2 Electronic Structure **18**

2.1 Introduction 18

2.2 Density Functional Theory 20

2.3 Exchange and Correlation 24

2.4 Solving the Kohn-Sham Equations 28

2.5 Describing the Wavefunctions 33

2.6 The Pseudopotential Technique 36

2.7 The Projector Augmented Wave Method 39

2.8 Tight-Binding Methods 45

3 The Scanning Tunnelling Microscope **49**

3.1 Introduction 49

3.1.1 Uses of the Scanning Tunnelling Microscope 49

3.1.2 STM Structure 51

3.1.3 STM Operation and Imaging Modes 52
3.1.4 Other Operating Modes 55
3.2 STM Image Calculation 56

4 The Transition-Metal Dichalcogenides 65
4.1 Introduction 65
4.1.1 Atomic Structure 65
4.1.2 Uses and Literature Survey 67
4.2 Bulk MoS_2 and $MoTe_2$ 72
4.3 The Perfect Surfaces of MoS_2 and $MoTe_2$ 73
4.4 Conclusions 80

5 Electronic Structure and STM Images of Vacancy Defects on the MoS_2 and $MoTe_2$ Surfaces 81
5.1 Introduction 81
5.2 Chalcogen Vacancies on MoS_2 and $MoTe_2$ 82
5.3 Metal Vacancies on MoS_2 and $MoTe_2$ 87
5.3.1 Metal Vacancies on MoS_2 87
5.3.2 Metal Vacancies on $MoTe_2$ 92
5.4 Conclusions 101

6 STM-Induced Vacancy Formation on the MoS_2 Surface 104
6.1 Introduction 104
6.2 Electric field in PAW 108
6.3 Simulation Details 110
6.4 Zero-Field Atom Extraction 113
6.4.1 Atom-Extraction Barriers 113
6.4.2 Bond-Breaking and Gap-State Formation 118
6.4.3 Electronic Potential *vs.* Tip–Sample Separation 125
6.5 Field Effects in Atom Extraction 126

6.5.1 Effect on the Extraction Barrier 126
6.5.2 Polarisation Charge and Electric Field 130
6.6 Conclusions 136

7 Conclusions **141**

Appendices **146**

A Figure Conventions **146**
A.1 STM Images 146
A.2 Charge Density Slices 146
A.3 Atomic Representation 148

B The Jahn–Teller Effect and the D_{3h} Point-Symmetry Group **149**

C Mo-Cluster Tip Calculations **153**
C.1 Tip Only Calculations 153
C.1.1 Tip Geometry 153
C.1.2 Electric Field with Tip 153
C.2 Calculations of the Tip and Adsorbates 154
C.2.1 Equilibrium Tip–Adsorbate Separation 154
C.2.2 3D Structure of the Tip–Adsorbate Potential 157

D Extra MoS_2 Slab Calculations **160**
D.1 Surface Polarisation and Effective Electric field 160
D.2 Evaporation of Mo and S Atoms from the MoS_2 Surface 162
D.3 Surface Relaxation During Atom Extraction 163
D.4 Effects of Surface Charging and Electric Field on the Atom-Extraction Barrier 165

E Acronyms **167**

F Atomic Units **169**

F.1 Useful Conversions 169

Bibliography **170**

List of Tables

4.1 Comparison of calculated and experimental bond lengths for bulk MoS_2 and $MoTe_2$. 72

4.2 Bulk MoS_2 and $MoTe_2$ lattice parameters used in all simulations. 73

5.1 Lattice distortions on MoS_2 and $MoTe_2$ around chalcogen vacancies. 83

5.2 Symmetry-projected lattice distortion of the $MoTe_2$ surface with a Mo vacancy. 94

6.1 Zero-field barrier height against extraction of single Mo and S atoms from the MoS_2 surface 117

6.2 Local surface temperatures required to extract S and Mo atoms from the MoS_2 surface (zero field). 118

6.3 Local surface temperatures required to extract S and Mo atoms from the MoS_2 surface (finite field). 129

B.1 Character table of the D_{3h} point-symmetry group. 151

B.2 The behaviour of the irreducible representations of the D_{3h} group as the symmetry is reduced. 151

C.1 Equilibrium tip–adsorbate separations and binding energies for S and Mo adsorbed on the Mo cluster tip. 156

C.2 Relaxation energy and motion of S and Mo atoms adsorbed on a Mo tip. 157

C.3 Energy change after allowing tip–adsorbed S and Mo atoms to relax fully from their equilibrium apex positions. 158

D.1 Evaporation energy for S and Mo from the MoS_2 surface. 163

D.2 Tip, charging and field effects on the molybdenum-extraction barrier height. 166

List of Figures

2.1 Supercell representation of a surface. 34
2.2 Schematic representation of the PAW wavefunction. 42

3.1 STM tips and mini-tips. 52
3.2 Schematic of the STM tip and sample bands for a metallic tip and a semi-conducting sample. 53
3.3 The STM operating in constant current mode. 54
3.4 Schematic of the system considered in the Bardeen tunnelling formalism. 57
3.5 Assumed geometry in the Tersoff-Hamann approximation. . . . 58
3.6 Geometry in the Pendry tunnelling-current method. 61

4.1 Schematic diagrams of the atomic structure of the 2H transition-metal dichalcogenides. 66
4.2 Brillouin Zone of the 2H transition-metal dichalcogenides. 67
4.3 Constant height STM images of defects on WSe_2. 70
4.4 Characters etched onto the surface of MoS_2. 70
4.5 Contour plots of the total charge densities of bulk MoS_2 and $MoTe_2$. 74
4.6 Band-structures of bulk MoS_2 and $MoTe_2$. 75
4.7 Unit cell used in the PAW calculations on the perfect MoS_2 and $MoTe_2$ surfaces. 76

4.8 Full surface Brillouin Zone. 76
4.9 Total charge density of the single-slab surfaces of MoS_2 and $MoTe_2$. 77
4.10 Calculated filled-state STM images of the MoS_2 and $MoTe_2$ surfaces. 78
4.11 Calculated filled-state STM scan-lines of the perfect MoS_2 and $MoTe_2$ surfaces. 79

5.1 Chalcogen vacancy simulation cell. 82
5.2 Gap-state eigenvalues for chalcogen vacancies on MoS_2 and $MoTe_2$ surfaces. 83
5.3 Charge-density isosurfaces for the gap-states of MoS_2 and $MoTe_2$ with chalcogen vacancies. 84
5.4 Charge-density contours of MoS_2 and $MoTe_2$ with chalcogen vacancies. 85
5.5 Calculated STM images for MoS_2 and $MoTe_2$ with chalcogen vacancies. 86
5.6 Constant-current scan-lines of MoS_2 and $MoTe_2$ with chalcogen vacancies. 86
5.7 Simulation cell used for the MoS_2, Mo-vacancy system. 88
5.8 Eigenvalues and charge-density isosurfaces of MoS_2 with a metal vacancy. 89
5.9 Charge-density contours of MoS_2 with a metal vacancy. 90
5.10 STM image and scan-lines of MoS_2 with a metal vacancy 91
5.11 Simulation cell used for the $MoTe_2$, Mo-vacancy calculations. . . 92
5.12 Atomic structure of $MoTe_2$ with a metal vacancy before and after atomic relaxation. 93
5.13 Gap-state eigenvalues for $MoTe_2$ with Mo vacancy before and after atomic relaxation. 94

5.14 The symmetry projected distortions for $MoTe_2$ with a Mo vacancy. 96
5.15 The gap-states for $MoTe_2$ with a Mo vacancy. 97
5.16 Total and gap-state charge density of $MoTe_2$ with a Mo vacancy. 98
5.17 Calculated STM image and scan-lines for $MoTe_2$ with a Mo vacancy. 99
5.18 Empty-state Tersoff–Hamann STM image of the $MoTe_2$ surface with a single Mo vacancy 100

6.1 Schematic of the atomic potentials for an adsorbate-tip-sample system. 105
6.2 Schematic of the potentials for transfer of an atom and an ion between the tip and sample. 106
6.3 Geometry of the simulations carried out by Tsukada et al. . . . 107
6.4 Rounded-sawtooth external potential and plane-averaged total potential for MoS_2. 109
6.5 The atomic structure of the Mo-cluster tip used in the atom-extraction simulations. 111
6.6 Simulation cell used for the atom-extraction calculations. 111
6.7 Slab spacing in the atom-extraction simulations. 112
6.8 Zero-field barriers against extraction of single molybdenum and sulphur atoms from the MoS_2 surface. 114
6.9 Charge density as a S atom is extracted from the MoS_2 surface (tip at 10au). 119
6.10 Charge density as a S atom is extracted from the MoS_2 surface (tip at 11au). 120
6.11 Charge density as a Mo atom is extracted from the MoS_2 surface (tip at 11au). 121
6.12 Charge-density contours showing 'gap-state' formation a S atom is extracted from the surface of MoS_2. 123

6.13 Charge-density contours showing 'gap-state' formation as a Mo atom is extracted from the surface of MoS_2. 124
6.14 Self-consistent electronic potential in a line through the tip apex and a surface Mo atom. 126
6.15 Charge-density tails as a function of tip–sample separation . . . 127
6.16 Barriers against extraction of single Mo and S atoms from MoS_2 in an external field. 129
6.17 Charge density contours for a MoS_2 surface and Mo tip in an external field. 131
6.18 Polarisation charge density for a MoS_2 surface as a S atom is removed. 132
6.19 Polarisation charge density for the MoS_2 surface as a Mo atom is removed. 133
6.20 Electrostatic potential difference for the MoS_2 surface in an external field. 134
6.21 Naïve representation of the processes occurring in a dynamic tunnelling current situation. 135

A.1 Schematic showing the slice used throughout this thesis to show charge densities. 147
A.2 The atomic representation used in this thesis. 148

B.1 A simple Jahn–Teller potential. 150

C.1 Initial and relaxed geometry of the Mo cluster tip used in the simulations. 154
C.2 Electrostatic potential difference and polarisation charge density for a cluster Mo tip in an electric field. 155
C.3 Electrostatic potential difference for a tip in an electric field in a line through the tip apex. 155

C.4 Equilibrium tip–adsorbate structure for adsorbed S and Mo. . . 156

C.5 Preferred structure of S and Mo atoms adsorbed on a Mo-cluster tip. 158

D.1 Effective field in the supercell geometry. 161

D.2 The MoS_2 surface in the presence of an external applied field. . 162

D.3 Relaxed structure for the MoS_2 surface with one of the Mo atoms displaced by 2.8au in the c direction. 164

Acknowledgements

Many people have helped me through the three years of my PhD and I would particularly like to thank the following:

- Andrew Fisher, my PhD supervisor, for putting up with me for three years and always being available for advice and guidance;
- Carl Sofield, my CASE supervisor at AEA Technology in Harwell, for his encouragement and interest;
- The Engineering and Physical Science Research Council for the grant, and AEA Technology for the supplementary CASE award;
- Tony Harker, my co-supervisor at University College London;
- All the folks in the Condensed Matter & Materials Physics group at UCL;
- All the guys at Durham, where I spent my first year;
- and last, but definitely not least, my family, girlfriend and friends for keeping me at it.

Chapter 1

Introduction

Surfaces, and the processes which can occur on them, are important in many areas of science and engineering. With the invention of the Scanning Tunnelling Microscope (STM) by Binnig & Rohrer (1987) in the early 1980's, and the resulting family of Scanning Probe Microscopes (SPM) (Pool 1990), it has become possible to study many surface properties (*e.g.*, electronic density of states, topography, hardness, magnetic dipole ...) locally—in some cases with atomic scale resolution. On top of this, clever use of the STM has, amongst other things, made selective atomic-scale surface modification a reality, and has provided a means with which to watch processes such as chemical etching in real time. While the Scanning Probe Microscopes are extremely powerful surface science tools and have been instrumental in a number of important scientific breakthroughs, they often pose as many questions as they answer. For example, the STM is often used to study the topography of surfaces on the atomic scale, but even on perfect clean surfaces the images may not reflect the true topography. A thorough understanding of the processes occurring during SPM operation is essential if the SPM family is to be utilised to its maximum potential—theory and simulation must therefore be carried out alongside experimental work.

This thesis is concerned with the Scanning Tunnelling Microscope and the

transition-metal dichalcogenides (TX_2 where T represents the metal (group IVB, VB or VIB) and X represents the chalcogen (S, Se, Te)). The TX_2s are important materials used for solid lubrication and catalysis (see Section 4.1), and are well suited to SPM studies including surface modification—this has lead to a number of theoretical studies and simulations being carried out. This thesis reports electronic structure calculations of the surfaces of MoS_2 and $MoTe_2$, with particular regard to vacancy defects, defect imaging and the mechanisms via which vacancies can be produced with the STM tip.

The electronic structure of the surfaces was obtained via the *ab-initio* Projector Augmented Wave (PAW) method developed by Blöchl (1994). The PAW technique relies on Density Functional Theory (DFT) within the Local Density Approximation (LDA) and uses a combination of planewave and atom-centred basis sets to describe the full valence wavefunctions, including core region oscillations. Chapter 2, after a brief introduction (Section 2.1), discusses in detail the theory behind DFT (Section 2.2) and the LDA (Section 2.3). The basic techniques used to solve the electronic structure problem within DFT and a discussion of the pros and cons of a planewave basis set are covered in Sections 2.4 and 2.5 respectively. Section 2.6 explains the basics of the pseudopotential technique, upon which the PAW technique is built, and Section 2.7 covers the PAW method itself. Section 2.8 contains a brief introduction to the tight-binding electronic structure method (which has previously been used to study some of these systems), and describes some of its major advantages and disadvantages over *ab-initio* methods.

Chapter 3 is concerned with the Scanning Tunnelling Microscope. Section 3.1 covers the uses, basic structure, and usual methods of operation (with regard to imaging) of the STM. Section 3.2 provides a summary of some of the theoretical methods developed to calculated STM images, including the Tersoff–Hamann approximation which is used in this thesis.

Simulations of the perfect bulk and surfaces of MoS_2 and $MoTe_2$ are re-

ported in Chapter 4. The electronic and atomic structure of bulk MoS_2 and $MoTe_2$ are compared to those of other calculations and where possible, experiment (Section 4.2). The electronic structure, atomic structure and STM images of the perfect MoS_2 and $MoTe_2$ surfaces are examined in Section 4.3. Chapter 5 reports calculations on single, neutral metal and chalcogen vacancies on the MoS_2 and $MoTe_2$ surfaces. Section 5.2 covers the chalcogen vacancy and Section 5.3 covers the metal vacancy calculations. The effects of the vacancies on electronic and atomic structure are examined in detail, and STM images are obtained for the defective surfaces and compared with those of other calculations and experiments. Section 5.4 concludes the chapter.

The vacancies on the MoS_2 and $MoTe_2$ surfaces reported in Chapter 5 can be produced by voltage-pulsing with the STM tip at small tip–sample separation ($\lesssim$ 5Å), but so far the mechanisms behind the process are not fully understood. Chapter 6 reports calculations on the MoS_2 surface in the presence of a Mo-cluster tip and an external electric field—these are believed to be the first calculations of their kind to include both the tip and electric field for a non-metallic, partially-ionic surface. Section 6.1 contains a more detailed introduction and the motivation behind these simulations. The method used to include the external field in the PAW calculations is discussed in Section 6.2. The simulation details are covered in Section 6.3 and the results for atom-extraction under zero-field conditions are reported in Section 6.4. The effect of the external field on the atom-extraction barriers and the charge distribution, and the effective electric-field are discussed in Section 6.5. Section 6.6 concludes the chapter and summarises the results.

Chapter 7 contains a discussion and summary of the results of the previous chapters and includes some recommendations for further work.

This thesis contains many images of atomic and electronic structure as well as several calculated STM images—where possible the same conventions are used throughout. Appendix A summarises the colours/ sizes used to represent

atoms of various types, the conditions under which STM images were obtained, and the 2D slice used to show charge densities.

Appendix B contains a brief explanation of the Jahn–Teller effect which is found to occur for the metal vacancy in $MoTe_2$ (Section 5.3) as well as useful information on the D_{3h} point-symmetry group which is relevant to this vacancy. Appendices C and D describe supplementary calculations on a Mo-cluster tip and the MoS_2 surface respectively which are useful to the arguments of Chapter 6 but would interrupt the flow of the chapter. Appendix E contains a summary of the acronyms used in this thesis.

Atomic units (au) are used throughout this thesis, but where appropriate the equivalent in terms angströms and/or electron volts are given in brackets following the atomic units. Appendix F contains a conversion table between atomic and S.I. units, as well as some other useful conversions.

Much of the material in Chapters 4 and 5 has been published in *J. Phys.: Condens. Matter* (Caulfield & Fisher 1997); a brief summary of Chapter 6 has been submitted for publication in *Appl. Phys. A* (Proceedings of the 9th International Conference on Scanning Tunneling Microscopy/Spectroscopy and Related Techniques, Hamburg, Germany, 1997), with an extended report to be submitted to *J. Phys.: Condens. Matter.*

Chapter 2

Electronic Structure

2.1 Introduction

Knowledge of the behaviour of materials on the quantum-mechanical scale is important in both science and industry where the size of the systems under consideration approaches the nanometer. The electronics industry for example is facing a potential problem where the devices such as the Metal-Oxide-Semiconductor Field-Effect Transistor (MOSFET) can now be fabricated with features so small that their operation is no longer governed by the principles on which they were designed (Goldhaber-Gordon, Montemerlo, Love, Opiteck, & Ellenbogen 1997). Similarly, properties such as friction, which on the macroscopic scale obey simple rules, become much more difficult to predict as the size of the contact region becomes small. Of course, the definition of 'contact' itself becomes subjective at length-scales of the order of typical bond-lengths. The difference in behaviour of systems on the macro- and nano-scale can be both a good and a bad thing. Whilst the breakdown of conventional microelectronic devices at the nano-scale may cause problems in the short term, it means that attention must turn to investigating novel and potentially superior devices based on, for example, self-assembling molecular structures, or

single-electron transistors. Furthermore, devices such as the Scanning Probe Microscopes (Chapter 3), which can probe almost any property of a surface on the atomic scale, rely on quantum-mechanical effects for their operation. Hence, the ability to model systems on the atomic scale is of fundamental importance to the advancement of technology.

The behaviour and properties of any system can, in principle, be obtained by solving the many-body Schrödinger equation. In practice however, the intractability of the many-body Schrödinger equation for systems more complex than simple molecules means that alternative methods of finding the properties of a given system must be found. There are two basic ways to proceed in this case; the first is to introduce approximations to the Schrödinger equation. For example, in Hartree-Fock theory (Ashcroft & Mermin 1976a) the many-body problem is reduced to a set of coupled single-body problems by representing the wavefunctions with a Slater determinant of single particle wavefunctions. This Slater determinant is operated on by a single particle Hamiltonian of the form

$$\hat{H} = -\frac{1}{2}\nabla^2 + V_{\mathrm{EXT}} + V_{\mathrm{HART}} + V_{\mathrm{X}} \tag{2.1}$$

where V_{EXT} is the potential felt by the electrons due to the ions,

$$V_{\mathrm{HART}} = \int d\mathbf{r} \frac{n(\mathbf{r})}{|\mathbf{r} - \mathbf{r}'|} \tag{2.2}$$

is the electron–electron interaction potential within the Hartree approximation for a system with electronic density n, and V_{X} is the exchange potential arising from the anti-symmetric nature of the wavefunctions. The problems with this method are the lack of screening effects and an approximate representation of the many-body wavefunction. The advantage of the approximation methods is that they can be systematically improved by increasing the basis set (*e.g.*,

multi-configuration Hartree-Fock uses a small number of determinants to represent the wavefunction) and adding correction terms to the Hamiltonian, but at the cost of increased calculation time.

The alternative is to find a different representation of the problem, bypassing the many-body Schrödinger equation, and (hopefully) simplifying the problem in the process. Density Functional Theory (DFT) (Jones & Gunnarsson 1989) provides one such alternative representation which is widely used and has proven to be an extremely effective tool. Section 2.2 summarises the principles behind DFT; an explanation of the exchange-correlation energy, and the approximation used in this work (Local Density Approximation) can be found in section 2.3; the mechanics behind obtaining electronic structure within DFT is described in section 2.4. The techniques used to describe the wavefunctions are described in Section 2.5, followed by a description of the pseudopotential technique which is used to reduce the amount of information required to describe the wavefunctions (Section 2.6). Section 2.7 describes the theory behind the Projector Augmented Wave technique, used throughout this thesis, and the implementation of the methods discussed in the previous sections. In later chapters, comparisons will be made to results from tight-binding calculations, so the chapter is rounded off with a summary of the tight-binding method of calculating electronic structure (Section 2.8).

2.2 Density Functional Theory

Density Functional Theory (DFT) eliminates the need to solve the many-body Schrödinger equation directly, instead expressing observables in terms of the total electronic density $n(\mathbf{r}) = N \int d\mathbf{s}_2 \ldots d\mathbf{s}_N \, |\Psi(\mathbf{s}_1, \mathbf{s}_2, \ldots, \mathbf{s}_N)|^2$, where $\Psi(\mathbf{s}_1, \mathbf{s}_2, \ldots, \mathbf{s}_N)$ is the N-body wavefunction and the $\mathbf{s}_i$ represent the spin and spatial coordinates of the ith electron.

The basis of DFT comes from Hohenberg & Kohn (1964) who stated that

1) any (observable) ground-state property of a system can be expressed in terms of the ground state electronic density, and 2) the energy of a system is minimised by the ground-state density. The first point can be justified by noting that the ground-state density $n_0(\mathbf{r})$ is unique to a given potential $V(\mathbf{r})$, *i.e.*, two systems with differing potentials cannot have the same ground-state electronic density. Thus the density $n(\mathbf{r})$ uniquely determines the potential and hence all other properties of the system, including the total energy. The second point follows logically on from the first—since $n_0(\mathbf{r})$ determines the ground state energy $E_0 = E[n_0]$, and E_0 is by definition the lowest energy the system can have, then no other density n can produce a lower energy, *i.e.*, $E[n] \geqslant E_0$ for all densities n. Therefore minimisation of the density functional $E[n]$ with respect to n will yield the ground-state energy and density.

Kohn & Sham (1965) devised a useful way of writing the energy functional, isolating several terms that are easily calculated and bundling all unknown quantities into one term:

$$E[n] = E_{\mathrm{KE}}[n] + E_{\mathrm{HART}}[n] + E_{\mathrm{EXT}}[n] + E_{\mathrm{XC}}[n] \tag{2.3}$$

where

$$E_{\mathrm{KE}}[n] = \sum_{i=1}^{N} \langle \psi_i(\mathbf{r}) | \frac{1}{2} \nabla^2 | \psi_i(\mathbf{r}) \rangle \tag{2.4}$$

is the kinetic energy of a set of N non-interacting electrons having the same density $n(\mathbf{r}) = \sum_{i=1}^{N} |\psi_i(\mathbf{r})|^2$ as the full interacting system; E_{HART} is the electron–electron interaction energy within the Hartree approximation

$$E_{\mathrm{HART}}[n] = \frac{1}{2} \int d\mathbf{r} d\mathbf{r}' \frac{n(\mathbf{r}) n(\mathbf{r}')}{|\mathbf{r} - \mathbf{r}'|}; \tag{2.5}$$

E_{EXT} is the electron–ion Coulomb interaction term (Section 2.6)

$$E_{\mathrm{EXT}}[n] = \int d\mathbf{r}\; V_{\mathrm{EXT}}(\mathbf{r})n(\mathbf{r}); \tag{2.6}$$

and E_{XC} is the so-called the exchange-correlation (XC) energy which includes all other energy terms. Application of the variational principle (Goldstein 1950) with the condition of conserved particle number leads to

$$\frac{\delta E[n]}{\delta n(\mathbf{r})} = \frac{\delta E_{\mathrm{KE}}[n]}{\delta n(\mathbf{r})} + V_{\mathrm{EXT}} + V_{\mathrm{HART}} + \frac{\delta E_{\mathrm{XC}}[n]}{\delta n(\mathbf{r})} = \mu, \tag{2.7}$$

where μ is the Lagrange multiplier arising from the constraint. The crucial observation here is that equation (2.7) for the interacting system is of exactly the same form as that of a non-interacting system with an effective external potential $V_{\mathrm{EFF}}(\mathbf{r})$ given by

$$V_{\mathrm{EFF}}(\mathbf{r}) = V_{\mathrm{EXT}} + V_{\mathrm{HART}} + \frac{\delta E_{\mathrm{XC}}[n]}{\delta n(\mathbf{r})}. \tag{2.8}$$

The implication is that the ground-state charge density associated with equation (2.8) can be obtained via a self-consistent solution to the independent-particle Schrödinger equation

$$\left[-\frac{1}{2}\nabla^2 + V_{\mathrm{EFF}}(\mathbf{r})\right]\psi_i(\mathbf{r}) = \epsilon_i\psi_i(\mathbf{r}) \tag{2.9}$$

and using the standard relation between the eigenfunctions and density

$$n(\mathbf{r}) = \sum_{i=1}^{N} |\psi_i(\mathbf{r})|^2, \tag{2.10}$$

where the ψ_i are subject to the orthonormality constraint

$$\langle\psi_i|\psi_j\rangle = \delta_{ij}. \tag{2.11}$$

The same single-particle Schrödinger equation (2.9) can be obtained via direct minimisation of the density functional (Equation (2.3)) with respect to the conjugate single-electron wavefunctions ψ_i^* under the constraints of equation (2.11).

The set of equations (2.9) are known as the Kohn-Sham (KS) equations and there are some important points to note: firstly, the KS eigenfunctions, ψ_i, are those of a fictitious single-particle Hamiltonian and therefore there is not necessarily any relation between $n_i(\mathbf{r}) = |\psi_i(\mathbf{r})|^2$ and any real single-particle state in the interacting system. Similarly, the KS eigenvalues ϵ_i, which arose as a result of enforcing conservation of charge, need not reproduce the density of states or define the electron transport properties of the full interacting system. The only definite relation between the fictitious system described by the KS equations and the many-body system, other than equation (2.10), is that the eigenvalue of the highest occupied eigenstate is equal to the chemical potential for the electrons (Jones & Gunnarsson 1989). In practice, for reasons still not fully understood, the exact KS eigenvalues and state-densities can often closely match those obtained by other methods such as Hartree-Fock and the agreement with experiment in areas such as photoelectron spectra for weakly correlated systems are usually very good (Jones & Gunnarsson 1989). Hence DFT is regularly used to predict behaviour beyond its obvious boundaries of applicability; for example, the work of the author reported in later chapters assumes that the STM images can be predicted from the density of states implied by the KS eigenvalues.

The density-functional formalism described above is in principle exact. For this to remain the case, the exchange-correlation energy E_{XC} will need to include effects due to the Pauli exclusion principle (exchange), charge screening (correlation) and must cancel the self-interaction energy implicit in E_{HART}. However, an exact form of E_{XC} is only known for very simple systems; even the free-electron gas problem proves too difficult to solve analytically and the

exact results can only be calculated via Monte-Carlo simulations (Ceperley & Alder 1980). In general then, approximations to E_{XC} must be made.

2.3 Exchange and Correlation

An exact expression for the exchange-correlation energy can be obtained by considering the transition from a non-interacting to an interacting system, *i.e.*, replacing the Coulomb interaction with $\lambda/\left|\mathbf{r}-\mathbf{r}'\right|$ where the coupling constant λ varies from 0 to 1. The true Coulomb interaction energy (with $\lambda = 1$) can be written as

$$E_{\mathrm{INT}} = \frac{1}{2}\int \frac{d\mathbf{r}d\mathbf{r}'}{|\mathbf{r}-\mathbf{r}'|}\left[\langle\hat{n}(\mathbf{r})\hat{n}(\mathbf{r}')\rangle - \delta(\mathbf{r}-\mathbf{r}')\langle\hat{n}(\mathbf{r})\rangle\right] \tag{2.12}$$

where the notation $\langle\hat{a}\rangle$ represent the expectation value of the operator $\hat{a}$, *i.e.*, $\langle\hat{a}\rangle = \sum_i \langle\psi_i|\hat{a}|\psi_i\rangle$, and $\hat{n}(\mathbf{r})$ is the operator for the density $n(\mathbf{r})$.

Following Gunnarsson & Lundqvist (1976), the Hamiltonian

$$H(\lambda) = E_{\mathrm{KE}} + V_{\mathrm{EXT}} + \frac{\lambda}{2}\sum_{i\neq j}\frac{1}{|\mathbf{r}_i-\mathbf{r}_j|} \tag{2.13}$$

is defined such that $H(1)$ is the Hamiltonian of the interacting system, defined to have a ground-state density $n(\mathbf{r})$, and $H(0)$ represents a non-interacting system. Furthermore, define the potential $V[n,\lambda]$ such that for all λ

$$\tilde{H}(\lambda) = H(\lambda) + V[n,\lambda] \tag{2.14}$$

has the same ground-state density $n(\mathbf{r})$. Then we have

$$\begin{aligned} E(\lambda) &= \langle \tilde{H}(\lambda) \rangle \\ &= E(0) + \int_0^\lambda d\lambda \frac{dE(\lambda)}{d\lambda} \\ &= E(0) + \int_0^\lambda d\lambda \left\langle \frac{dV[n,\lambda]}{d\lambda} \right\rangle + \int_0^\lambda \frac{d\lambda}{\lambda} E_{\mathrm{INT}}, \end{aligned} \tag{2.15}$$

where $E_{\mathrm{INT}}(\lambda)$ is the Coulomb interaction energy

$$E_{\mathrm{INT}}(\lambda) = \left\langle \frac{\lambda}{2} \sum_{i \neq j} \frac{1}{|\mathbf{r}_i - \mathbf{r}_j|} \right\rangle \tag{2.16}$$

and is equivalent to that of the true interacting system (equation (2.12)) for $\lambda = 1$. Since $V[n,\lambda]$ is a one-electron operator, $V[n,1] = 0$ and the density $n(\mathbf{r})$ does not depend on λ we have

$$\int_0^1 d\lambda \left\langle \frac{dV[n,\lambda]}{d\lambda} \right\rangle = \int_0^1 d\lambda \int d\mathbf{r} \frac{dV[n,\lambda]}{d\lambda} n(\mathbf{r}) \tag{2.17}$$

$$= -\int d\mathbf{r} V[n,0]\, n(\mathbf{r}). \tag{2.18}$$

Similarly, equations (2.13), (2.14) and (2.15) give

$$E(0) = E_{\mathrm{KE}}[n] + \int d\mathbf{r} \left\{ V_{\mathrm{EXT}}(\mathbf{r}) + V[n,0] \right\} n(\mathbf{r}). \tag{2.19}$$

Rearranging equation (2.3) and substituting for equations (2.15), (2.18) and (2.19) leads to

$$\begin{aligned} E_{\mathrm{XC}}[n] &= \int_0^1 \frac{d\lambda}{\lambda} E_{\mathrm{INT}}(\lambda) - \frac{1}{2} \int d\mathbf{r} d\mathbf{r}' \frac{n(\mathbf{r}) n(\mathbf{r}')}{|\mathbf{r} - \mathbf{r}'|} \\ &= \frac{1}{2} \int \frac{d\mathbf{r} d\mathbf{r}'}{|\mathbf{r} - \mathbf{r}'|} \int_0^1 d\lambda \left[\langle \tilde{n}(\mathbf{r}) \tilde{n}(\mathbf{r}') \rangle_{n,\lambda} - \delta(\mathbf{r} - \mathbf{r}') n(\mathbf{r}) \right], \end{aligned} \tag{2.20}$$

where $\tilde{n}(\mathbf{r}) = \hat{n}(\mathbf{r}) - n(\mathbf{r})$ is the operator returning the fluctuations of the

instantaneous density about its mean distribution $n(\mathbf{r}) = \langle \hat{n}(\mathbf{r}) \rangle$. Putting equation (2.20) another way: if we write

$$n_{xc}(\mathbf{r}, \mathbf{r}'; \lambda) = \frac{\langle \tilde{n}(\mathbf{r}) \tilde{n}(\mathbf{r}') \rangle_{n,\lambda}}{n(\mathbf{r})} - \delta(\mathbf{r} - \mathbf{r}') \tag{2.21}$$

as the exchange-correlation hole (*i.e.*, depletion of charge) at $\mathbf{r}'$ associated with the presence of an electron at $\mathbf{r}$, then the exchange-correlation energy can be thought of as the interaction between an electron and its associated exchange-correlation hole,

$$E_{\mathrm{XC}}[n] = \frac{1}{2} \int \frac{d\mathbf{r} d\mathbf{r}'}{|\mathbf{r} - \mathbf{r}'|} \int_0^1 d\lambda \; n(\mathbf{r}) n_{xc}(\mathbf{r}, \mathbf{r}'). \tag{2.22}$$

It is clear that integration of equation (2.21) gives the total charge associated with the hole as

$$\int d\mathbf{r} d\mathbf{r}' n_{xc}(\mathbf{r}, \mathbf{r}'; \lambda) = -1. \tag{2.23}$$

An exact evaluation of equation (2.20) would require knowledge of the pair-correlation function at all points in space, which implies the problem is already solved, so it is this point that approximations must be introduced. One common approximation, and the one used throughout this work, is the Local Density Approximation (LDA) whereby $\langle \tilde{n}(\mathbf{r}) \tilde{n}(\mathbf{r}') \rangle_{n,\lambda}$ of equation (2.20) is replaced by $\langle \tilde{n}(\mathbf{r}) \tilde{n}(\mathbf{r}') \rangle^h_{n,\lambda}$, the correlation function of a homogeneous electron-gas with density n and coupling constant λ. This quantity can be shown to be related (Jones & Gunnarsson 1989) to the homogeneous electron-gas pair-correlation function at density n, $g(\mathbf{r}; n)$, so that E_{XC} is now

$$E_{\mathrm{XC}}[n] \approx \frac{1}{2} \int \frac{d\mathbf{r} d\mathbf{r}'}{|\mathbf{r} - \mathbf{r}'|} \int_0^1 d\lambda \left\{ n^2(\mathbf{r}) \left[g\left(|\mathbf{r} - \mathbf{r}'| ; n(\mathbf{r}) \right) - 1 \right] \right\}. \tag{2.24}$$

The LDA is in principle only valid in the regime where the density $n(\mathbf{r})$ varies slowly on the scale of the Fermi wavelength—in most real systems this is not the case, and in many cases, in particular for isolated atoms, the LDA does not do a very good job of describing the exact structure of the exchange-correlation hole (Jones & Gunnarsson 1989). However, the Coulomb interaction is spherically symmetric and it can therefore be shown (Jones & Gunnarsson 1989) that only the spherical average of n_{xc} enters E_{XC}. Since the LDA is based on the homogeneous electron gas, the exchange-correlation hole itself is spherically symmetric and furthermore obeys equation (2.23). As a result the LDA provides a much better description of the exchange-correlation energy than might initially be expected, and provides accuracy at least rivaling that of other electronic structure methods (*e.g.*, Self-consistent Hartree-Fock) for many systems (Godby, Schlüter, & Sham 1986).

There are still several problems with the LDA as it stands, nicely summarised by Perdew & Zunger (1981). These include the underestimation of the band-gap in insulators; the lack of any stable negative ions and poor description of charged point-defect states; underestimation of the total energy of a metal surface; and overestimation of the total energy of isolated atoms. It is possible to include corrections to the energy functional in order to reduce the errors on some of these problems. One such correction is the Self-Interaction Correction (Perdew & Zunger 1981) which reduces the spurious self-energy by introducing an orbital-dependent correction. However, this has the disadvantage of making the effective potential orbital-dependent, increasing the complexity of the problem. It is also possible to include corrections due to the local gradient of the density, but the benefits in terms of accuracy are not as great as one might expect and there is an increase in the cost of the calculations.

Despite the above deficiencies of the LDA, it is extremely effective in the simulation of most systems of interest to solid-state science. For example,

energy differences and bond lengths of solids and molecules can typically be expected to be accurate to better than 5% (often better than 2%). The current work does not include any corrections to the LDA, but implements the Perdew & Zunger (1981) parameterisation of E_{XC} obtained via the solution of the many-body Schrödinger equation for the free-electron gas obtained via Monte-Carlo methods (Ceperley & Alder 1980).

2.4 Solving the Kohn-Sham Equations

The density-functional formalism provides the methods needed to calculate the ground-state properties of a system of electrons in an external potential V_{EXT}. Given this, there arises the question of how to relax the electrons from some initial-guess configuration to the ground-state structure. Furthermore, whilst calculations on systems of fixed atoms can provide a great deal of information, the ability to propagate the nuclei according to the forces acting on them (Molecular Dynamics (MD)) is useful for the study of, for example, surface reconstructions and the vibrational modes of molecules and solids.

The initially obvious method via which to obtain the ground-state KS wavefunctions and eigenvalues is diagonalisation of the KS Hamiltonian (Equation (2.9)). The problem with this method is the rate at which the diagonalisation proceeds—it is very difficult to converge the electronic degrees of freedom to such an extent that the forces on the nuclei are accurate enough for energy-conserving dynamics in a reasonable amount of time (However, see (VASP 1997) where extremely efficient diagonalisation routines and Vanderbilt pseudopotentials are combined to produce an efficient electronic structure code). This time problem is compounded by the fact that the Hamiltonian would have to be diagonalised every time the density is updated, and leads to the conclusion that the diagonalisation method is not ideally suited molecular dynamics. Coming to the rescue, Car & Parrinello (1989) produced a

scheme which combined density-functional theory and molecular dynamics in a way that made it possible to propagate/ relax the atomic and electronic degrees of freedom simultaneously, enabling relatively quick and easy solution of the Kohn-Sham equations and energy-conserving motion along the Born-Oppenheimer (BO) energy surface. An outline of the procedure, known as the Car-Parrinello (CP) algorithm, follows.

The minimisation of the density functional $E[n]$ with respect to n can also be considered as minimisation of a functional $E[\psi_i]$ with respect to the KS wavefunctions ψ_i. Rewriting equation (2.3) in this manner and including the nuclear–nuclear interaction energy gives

$$\begin{aligned} E[\psi_i, \mathbf{R}_I] &= E_{\mathrm{KE}}[\psi_i] + E_{\mathrm{HART}}[\psi_i] + E_{\mathrm{XC}}[\psi_i] \\ &\quad + E_{\mathrm{EXT}}[\psi_i, \mathbf{R}_I] + E_{\mathrm{ION}}(\mathbf{R}_I) \end{aligned} \tag{2.25}$$

where

$$E_{\mathrm{ION}}(\mathbf{R}_I) = \frac{1}{2} \sum_{I \neq J} \frac{Z_I Z_J}{|\mathbf{R}_I - \mathbf{R}_J|}, \tag{2.26}$$

where Z_I is the charge on ion I. The summation over i and I in the energy arguments is implicit (*e.g.*, $E_{\mathrm{EXT}}[\psi_i, \mathbf{R}_I]$ is a functional of the complete set of KS eigenstates $\{\psi_i\}$ and a function of all atomic coordinates $\{\mathbf{R}_I\}$).

The next step is to introduce a fictitious mass μ and a time-dependence to the electronic degrees of freedom. It is then possible to assign a classical 'fictitious kinetic energy' E_{FKE} to the electronic wavefunctions

$$E_{\mathrm{FKE}}[\psi_i] = \frac{1}{2} \mu \sum_i \langle \dot{\psi}_i | \dot{\psi}_i \rangle, \tag{2.27}$$

and hence, using equations (2.25) and (2.27), to write down a classical Lagrangian which describes the motion of the electronic and nuclear degrees of

freedom

$$\mathcal{L} = T - V = E_{\mathrm{FKE}}[\psi_i] + E_{\mathrm{IKE}}[\mathbf{R}_I] - E[\psi_i, \mathbf{R}_I], \tag{2.28}$$

where $E_{\mathrm{IKE}} = \frac{1}{2}\sum_I M_I \dot{\mathbf{R}}_I^2$ is the kinetic energy of the ions. Solving this Lagrangian (Car & Parrinello 1989) subject to the orthonormalisation constraints (Equation (2.11)), leads to the following equations of motion for the wavefunctions and nuclei:

$$\mu\ddot{\psi}_i(\mathbf{r},t) = -\hat{H}\psi_i(\mathbf{r},t) + \sum_j \Lambda_{ij}\psi_j(\mathbf{r},t) \tag{2.29}$$

$$M_I\ddot{\mathbf{R}}_I = -\frac{\partial E[\psi_i, \mathbf{R}_I]}{\partial \mathbf{R}_I}, \tag{2.30}$$

where the relation $\frac{\delta E[\psi_i, \mathbf{R}_I]}{\delta \psi_i^*} = 2\hat{H}\psi_i(\mathbf{r},t)$ has been used, and the Λ_{ij} are the Lagrange multipliers arising from the constraints. Taking the overlap of equation (2.29) with some wavefunction ψ_k and using the orthonormality relation leads to an expression for the Lagrange multipliers

$$\Lambda_{ij} = H_{ji} - \langle\dot{\psi}_j|\dot{\psi}_i\rangle \tag{2.31}$$

The important point about these 'fictitious' equations of motion is that they produce the same dynamics as would be obtained via the Hellmann-Feynman theorem (where the motion is assumed adiabatic, *i.e.*, the ions move on a potential surface where the electrons remain in the ground-state configuration—the Born-Oppenheimer (BO) surface) provided

$$\nu_e \gg \nu_I, \tag{2.32}$$

where ν_e and ν_I represent the frequencies of oscillation of the electronic and ionic degrees of freedom respectively. In this case, the electrons oscillate rela-

tively rapidly about the ground-state for the current ionic configuration so that the average force on the ions is that which would be obtained if the electrons were actually on the BO surface. Equation (2.32) can often be fulfilled by manipulation of the fictitious electron mass μ (but difficulties arise for metallic systems).

The Car–Parrinello algorithm, then, has reduced the problem of solving the KS equations to one in classical mechanics; integration of the equations of motion can now proceed by any standard MD technique. The Verlet Algorithm (Allen & Tildesley 1987) is one well-used method which, for a simulation time-step Δt, gives

$$\begin{aligned} \psi_i(\mathbf{r}, t+\Delta t) &= 2\psi_i(\mathbf{r}, t) - \psi_i(\mathbf{r}, t-\Delta t) - \\ &\quad \frac{(\Delta t)^2}{\mu}\left(\hat{H}\psi_i(\mathbf{r}, t) + \sum_j \Lambda_{ij}\psi_j(\mathbf{r}, t)\right) \qquad (2.33) \\ \mathbf{R}_I(t+\Delta t) &= 2\mathbf{R}_I(t) - \mathbf{R}_I(t-\Delta t) + \frac{(\Delta t)^2}{M_I}\frac{\delta E[\psi_i, \mathbf{R}_I]}{\delta \mathbf{R}_I}. \qquad (2.34) \end{aligned}$$

The initial approach to the BO surface and simulated annealing can be implemented under the same scheme if $\dot{\psi}_i$- and/or $\dot{\mathbf{R}}$-dependent damping terms are added to equations (2.33) and (2.34) respectively. The velocities of the degrees of freedom do not explicitly appear within the standard Verlet algorithm, but they can be approximated by

$$\dot{\psi}_i(\mathbf{r}, t) = \frac{\psi(\mathbf{r}, t+\Delta t) - \psi(\mathbf{r}, t-\Delta t)}{2\Delta t}, \qquad (2.35)$$

with a similar expression for $\dot{\mathbf{R}}_I(t)$. The time-step Δt must be chosen small enough so that the deviation from the BO surface is small and hence the system's total energy energy (Equation (2.25)) is conserved. In practice, choosing too large a value of Δt will cause the total energy of the fictitious system to increase exponentially with time as the system strays further away from the

BO energy surface. Typical DFT MD simulations use time-steps $\Delta t \sim 10$au (sufficient to integrate systems with frequencies $\lesssim 10$au which is of the order of a typical plasmon frequency).

Direct implementation of the Verlet algorithm as it stands in equations (2.33) and (2.34) however would lead to deterioration of the ($\dot{\psi}_i$-dependent) constraints and the simulation would become unstable after just a few time-steps. Instead an alternative formulation, discussed by Ryckaert, Ciccotti, & Berendsen (1977) in relation to solving the general problem of MD with constraints, is used. Initially the wavefunction is calculated at time $t + \Delta t$ without considering the constraints; *i.e.*, one calculates

$$\bar{\psi}_i(\mathbf{r}, t + \Delta t) = 2\psi_i(\mathbf{r}, t) - \psi_i(\mathbf{r}, t - \Delta t) - \frac{(\Delta t)^2}{\mu}\hat{H}\psi_i(\mathbf{r}, t). \tag{2.36}$$

It is then possible to calculate the constraints Λ_{ij} to arbitrary accuracy by an iterative equation (Car & Parrinello 1989) dependent only on the known quantities $\bar{\psi}_i(\mathbf{r}, t + \Delta t)$ and $\psi_i(\mathbf{r}, t)$:

$$\begin{aligned} \Lambda^{(n+1)} &= \frac{1}{2}\left[\frac{\mu}{(\Delta t)^2}(1 - \mathrm{A}) + \Lambda^{(n)}(1 - \mathrm{B})\right. \\ &\quad \left. + \left(1 - \mathrm{B}^{\dagger}\right)\Lambda^{(n)} - \frac{(\Delta t)^2}{\mu}\Lambda^{(n)2}\right], \end{aligned} \tag{2.37}$$

where A and B are the matrices whose elements are

$$\begin{aligned} \mathrm{A}_{ij} &= \langle\bar{\psi}_i(\mathbf{r}, t + \Delta t)|\bar{\psi}_j(\mathbf{r}, t + \Delta t)\rangle \\ \mathrm{B}_{ij} &= \langle\psi_i(\mathbf{r}, t)|\bar{\psi}_j(\mathbf{r}, t + \Delta t)\rangle \end{aligned} \tag{2.38}$$

Using an initial guess $\Lambda^{(0)} = \frac{1}{2}(1 - \mathrm{A})$ equation (2.37) often reaches a machine-accurate solution in one iteration (Car & Parrinello 1989).

The Car–Parrinello algorithm is an effective and now widely-used algorithm

via which to solve the Kohn–Sham equations. However, it is not the only way to proceed and there is now a move towards the so-called 'Conjugate-Gradients' techniques (Press, Flannery, Teukolsky, & Vettering 1986) which utilise information on the energy gradient to choose a quicker route to the Born-Oppenheimer surface. This method is particularly advantageous where the energy surface has regions of shallow gradient where the steepest descent algorithms can take an unnecessarily large amount of time to approach the energy minimum. It is now also possible, through the development of extremely efficient diagonalisation routines and effective pseudopotentials (see Section 2.6), to diagonalise the Hamiltonian directly. The Vienna *Ab-initio* Simulation Package (VASP 1997) uses such a technique.

2.5 Describing the Wavefunctions

The backbone of a method via which atomic and electronic structure can be calculated has been presented and now attention must turn to the scheme used to describe the wavefunctions. In principle, any wavefunction could be expanded in an infinite set of linearly independent functions such as plane-waves or atomic orbitals. In reality, infinite expansions are not practical and some finite set of functions must be used to provide an approximation to the wavefunction. The idea then, is to choose a set of functions able to describe the wavefunctions to within the desired accuracy and which are also amenable to computer calculations in terms of storage and ease of manipulation.

When choosing a basis set in which the wavefunctions are to be expanded it is important to consider the type of systems which will be simulated. For the solid-state physicist the systems of most interest are extended, possibly crystalline, systems consisting of order 10^{23} atoms (*cf.* quantum chemists who may be interested in the interactions of a small number of molecules). A quantum mechanical simulation on this scale would be beyond the scope of

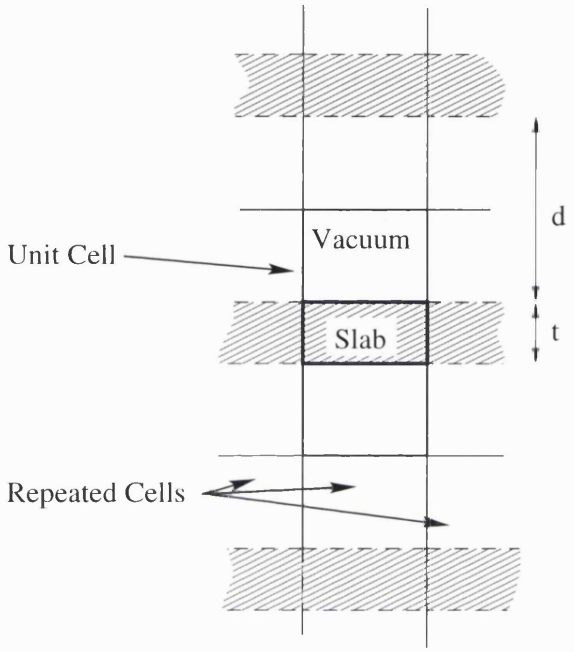

Figure 2.1: Schematic of the supercell representation of a surface. The periodic boundary conditions force the use of slabs to approximate surfaces and care must be taken in choosing the slab thickness t and vacuum gap size d to minimise surface–surface interactions.

today's computers and most solid-state calculations rely on the use of periodic boundary conditions. Periodic boundary conditions are ideal for the study of perfect crystalline materials which are inherently periodic, however the situation is more complicated for the study of defects in solids and/or surfaces (the subject of most of the work presented in later chapters). The problem is that introducing a defect into the unit cell of a periodic simulation implicitly introduces a defect into all other cells, producing an infinite array of defects. The solution is to ensure that the simulation cell is large enough such that the interaction between the defects of adjacent cells is small enough to be ignored. In addition, surfaces must be approximated by a supercell structure, *i.e.*, slabs of material surrounded by vacuum (see Figure 2.1). Care must be taken in this case when choosing the thickness of the slabs and the size of the simulation cell

in the direction perpendicular to the surface—the slab must be thick enough and the vacuum gap large enough so that the interactions between adjacent surfaces (both through the material itself, and across the vacuum gap) are negligible.

Given that periodic boundary conditions are being used, one can make use of Bloch's theorem which says that any wavefunction in a periodic potential takes the form of a plane wave multiplied by a functions with the periodicity of the potential, *i.e.*,

$$\psi_j^{\mathbf{k}}(\mathbf{r}) = e^{i\mathbf{k}.\mathbf{r}} U_j^{\mathbf{k}}, \tag{2.39}$$

where $\mathbf{k}$ is the quantum number which determines the transport properties of an electron via the 'crystal momentum' $\mathbf{p} = \hbar\mathbf{k}$. The decision must now be made how to describe the $U_j^{\mathbf{k}}$. The most common choice, and the one used for this work, is the plane-wave, *i.e.*, the wavefunctions are written as

$$\psi_j^{\mathbf{k}}(\mathbf{r}) = \sum_{\mathbf{g}} c_j^{\mathbf{k},\mathbf{g}} e^{i(\mathbf{k}+\mathbf{g}).\mathbf{r}}, \tag{2.40}$$

where the $\mathbf{g}$ are the reciprocal lattice vectors of the unit cell. In practice the summation over $\mathbf{g}$ is truncated so that only plane waves with $\frac{1}{2}|\mathbf{k}+\mathbf{g}|^2 \leqslant E_{\text{cut}}$ are considered. The code used in relation to this work (see section 2.7) makes the further simplification that $\mathbf{k}$ is restricted to the centre and corners of the reciprocal cell, where the wavefunctions are purely real, enabling the FFT to operate on two wavefunctions simultaneously and reducing the wavefunction-storage requirement by a factor of two.

The most valuable advantage bestowed by the use of a plane-wave basis set is that it is possible to transform the ψ_i from real to reciprocal space via the Fast Fourier Transform (FFT). The ability to use the FFT means that gradients, and hence E_{KE}, can be calculated efficiently and with no loss of

accuracy. In addition, by using planewaves no assumptions are made as to the form of the wavefunctions as is the case for, say, atomic orbital basis sets—this is good, but results in the requirement that a large number of planewaves are needed to describe the wavefunctions and this is a particular problem for the heavier elements. In their case, owing to the fermionic nature of electrons, the higher level (valence) wavefunctions must be orthogonal to those of the lower (core) levels, *i.e.*, the valence-electron wavefunctions must have a node around the 'centre of mass' of the core wavefunctions with lower energy, but same angular momentum. Since the core electrons are localised around the nucleus this implies that the valence electrons must oscillate rapidly in the vicinity of the nucleus—Heine (1970) showed that for aluminium, the electron–nuclear interaction matrix $v_{\mathbf{gg'}} = \langle c_i(\mathbf{g})|V_{\mathrm{EXT}}|c_i(\mathbf{g'})\rangle$ would need dimensions of order $10^6 \times 10^6$ per unit cell in order to describe accurately the valence-wavefunction oscillations. Since the CPU time required to solve the problem scales with the cube of the matrix size, if plane-waves are to be of any real use, a method of calculating E_{EXT} which reduces the size of $v_{\mathbf{gg'}}$ is required. The pseudopotential technique does just this.

2.6 The Pseudopotential Technique

The main motivations behind the introduction of pseudopotentials (Heine 1970) are twofold. First, as mentioned above, plane-waves cannot be used to describe the full valence wavefunctions of the heavier atoms owing to their rapidly oscillating nature, or the lighter atoms owing to their localisation around the nucleus. Secondly, it is only the valence electrons that are important in determining the bonding and chemical behaviour of atoms and solids under 'normal' conditions—treating the core electrons with the same rigour as the valence wavefunctions is often unnecessary.

A pseudopotential is a replacement for the full atomic potential and core

electrons that does not contain the Coulomb singularity at $\mathbf{r} = 0$, but which adequately reproduces the electronic structure and transport properties of a real system. There are in principle an infinite number of ways of defining a pseudopotential, but there are a few conditions that a useful pseudopotential must meet:

1. the pseudowavefunctions (*i.e.*, solutions to the Schrödinger equation with the atomic potential replaced by the pseudopotential) must be smooth and preferably nodeless;

2. outside some cutoff region Ω_{R} the pseudowavefunctions must be equal to the true valence wavefunctions;

3. inside Ω_{R} the scattering properties of the pseudopotential should match those of the full potential; and

4. the pseudopotential must be transferable—it must produce the correct valence wavefunctions and core scattering properties in a range of environments (*i.e.*, over a range of state energies and site symmetries).

The condition that the scattering properties of the pseudopotential match those of the full potential is satisfied provided the logarithmic derivatives of the pseudo- and full-wavefunctions are equal at the cutoff boundary. By imposing the further constraint that the correct charge be present within the cutoff region (norm-conservation), the relation (Bachelet, Hamann, & Schlüter 1982)

$$-2\pi \left[r\phi \frac{d}{dE} \frac{d}{dr} \ln \phi \right]_{\Omega_{\mathrm{R}}} = 4\pi \int_{\Omega_{\mathrm{R}}} r^2 \left|\phi\right|^2 dr, \tag{2.41}$$

where ϕ is a solution to the radial Schrödinger equation at some energy ϵ, implies that the scattering properties of the pseudopotential are, to first order variations in energy about ϵ, equal to those of the full potential. Therefore, the pseudopotential is transferable with regard to changes in the eigenvalues and

the range of energies over which this is the case depends on the smoothness of the pseudowavefunctions (Bachelet et al. 1982).

Most modern pseudopotentials are generated by a method based on that described by Bachelet et al. (1982). The radial Dirac equation is solved for the isolated atom to provide a set of radial wavefunctions $\psi_i(r)$ and eigenvalues ϵ_i. An alternative potential (the pseudopotential) is then found such that the pseudowavefunctions $\tilde{\psi}_i(r)$ equal the correct wavefunctions for $r > R$, but are smooth for $r < R$, where R is the cutoff radius, and have the same eigenvalues as the full one-electron eigenstates.

However, there are still some situations in which the pseudopotentials as described above are not a particularly effective method of reducing the number of plane-waves required to describe the wavefunctions. In particular, problems arise when attempting to describe the transition-metal elements—here, the core s and p levels force the use of a large cutoff, but the outer d level is then poorly described owing to its localisation around the nucleus. Therefore, despite the introduction of a pseudopotential, a small cutoff radius and a large cutoff energy are still required. This is also the case for the first row elements which have their valence electrons localised around the nucleus. There are a number ways of improving the pseudopotential technique such that this problem is reduced. One such method is the ultra-soft pseudopotential method of Vanderbilt (1990). The Vanderbilt technique is based on the conventional pseudopotential technique, but the norm-conservation condition is relaxed and as a reult the usual orthogonality condition $\langle\tilde{\psi}_i|\tilde{\psi}_j\rangle = \delta_{ij}$ becomes instead the more general condition

$$\langle\tilde{\psi}_i|S|\tilde{\psi}_j\rangle = \delta_{ij} \tag{2.42}$$

where S is a basis-dependent operator such that $S(\mathbf{r}, \mathbf{r}') = \delta(\mathbf{r} - \mathbf{r}')$ outside the cutoff region. This allows the electronic density to be described as the combina-

tion of a smooth (pseudo) part and an atom-centred part (the wavefunctions, however, are not similarly described). This enables previously troublesome elements to be treated without using small cutoff radii or a large planewave basis, but increases the complexity of the calculation (Laasonen, Pasquarello, Car, Lee, & Vanderbilt 1993).

The Augmented Plane Wave (APW) method is another electronic-structure technique which can be shown to be similar to the pseudopotential approach. Here the wavefunction is assumed to be easily described by plane waves outside some sphere—the augmentation sphere, and inside this sphere the potential is assumed to be spherically symmetric so that the wavefunctions are solutions to the radial Schrödinger equation. The logarithmic derivatives of the pseudowavefunctions are matched onto those of the solutions to the radial Schrödinger equation at the edge of the augmentation sphere. In contrast to the conventional pseudopotential techniques, with the APW method the full valence wavefunctions are known (including core oscillations) making it a so-called 'all-electron' method.

The work described here uses the Projector Augmented Wave (PAW) method which is based on a conbination of the pseudopotential and APW techniques—like the APW method, the PAW method is an all-electron technique.

2.7 The Projector Augmented Wave Method

The Projector Augmented Wave (PAW) (Blöchl 1994) technique is a Car–Parrinello-based, All-Electron (AE) method combining many of the useful properties of both the pseudopotential and the Augmented Plane Wave methods. 'All-Electrons' here means that the complete single-electron valence wavefunctions are calculated, including the core-region oscillations—core level electrons are currently treated within the frozen-core approximation, although the PAW formalism is not restricted to such a description. The idea behind the

PAW method is to split the wavefunction into smooth and oscillatory components so that the smooth (pseudo) component of the wavefunction may be expanded in plane waves on a regular grid and the oscillatory component, which is localised in the atomic-core regions, can be described by some localised basis set. The crux of the problem is to find a transformation $\mathcal{T}$ which maps the pseudo (PS) wavefunctions $|\tilde{\psi}\rangle$ onto the AE wavefunctions $|\psi\rangle$ according to $|\psi\rangle = \mathcal{T}|\tilde{\psi}\rangle$ (where the valence level suffix i has been dropped for simplicity). Assuming this transformation exists, the expectation value of any operator A can then be obtained directly from the PS wavefunctions according to $\langle A\rangle = \langle\tilde{\psi}|\tilde{A}|\tilde{\psi}\rangle$ where $\tilde{A} = \mathcal{T}^\dagger A\mathcal{T}$ is the pseudo-operator. In the PAW method, the operator $\mathcal{T}$ is taken to be a linear transformation of the form

$$\mathcal{T} = 1 + \sum_R \mathcal{T}_R, \tag{2.43}$$

where $\mathcal{T}_R$ is an operator whose influence is restricted to some atom-centred augmentation region Ω_R. Outside this augmentation region, then, the PS and AE wavefunctions must coincide (as with most pseudopotential methods). Within the augmentation region, the AE and PS wavefunctions are expanded in terms of localised AE and PS 'partial waves' $|\phi_{\mathbf{R}i}\rangle$ and $|\tilde{\phi}_{\mathbf{R}i}\rangle$ respectively, where the index $\mathbf{R}$ represents the atomic position about which they are centred, and the index i runs over the components of the partial-wave basis sets. In the current implementation, the AE partial waves are chosen to be solutions to the radial Schrödinger equation for the isolated atom—the index i therefore spans the principal and angular-momentum quantum numbers (see later).

So, within some Ω_R centred on $\mathbf{R}$,

$$|\tilde{\psi}\rangle = \sum_i |\tilde{\phi}_{\mathbf{R}i}\rangle c_{\mathbf{R}i}, \text{ and} \tag{2.44}$$

$$|\psi\rangle = \mathcal{T}|\tilde{\psi}\rangle = \sum_i |\phi_{\mathbf{R}i}\rangle c_{\mathbf{R}i}, \tag{2.45}$$

where the $c_{\mathbf{R}i}$ are the expansion coefficients to be determined. Since the transformation is required to be linear, the coefficients $c_{\mathbf{R}i}$ will be linear functionals of the PS wavefunctions:

$$c_{\mathbf{R}i} = \langle \tilde{p}_{\mathbf{R}i} | \tilde{\psi} \rangle, \tag{2.46}$$

where the $\tilde{p}_{\mathbf{R}i}$ are the so-called 'projector' functions. Combining equations (2.44) and (2.46) leads to the condition on the projector functions

$$\langle \tilde{p}_{\mathbf{R}i} | \tilde{\phi}_{\mathbf{R}j} \rangle = \delta_{ij}; \tag{2.47}$$

there are many ways in which the projector functions may be defined such that (2.47) is satisfied. In practice, one applies the further constraint that the PS and AE partial waves coincide outside Ω_{R}, then the transformation $\mathcal{T}$ can take the form

$$\mathcal{T} = 1 + \sum_{\mathbf{R},i} \left(|\phi_{\mathbf{R}i}\rangle - |\tilde{\phi}_{\mathbf{R}i}\rangle \right) \langle \tilde{p}_{\mathbf{R}i}|, \tag{2.48}$$

and the AE wavefunction over all space may be written as

$$|\psi\rangle = |\tilde{\psi}\rangle + \sum_{\mathbf{R},i} \left(|\phi_{\mathbf{R}i}\rangle - |\tilde{\phi}_{\mathbf{R}i}\rangle \right) \langle \tilde{p}_{\mathbf{R}i} | \tilde{\psi} \rangle. \tag{2.49}$$

Figure 2.2 shows a schematic representation of the three terms in equation (2.49)—from the above definitions of the partial waves it is obvious that within the augmentation region the first and third terms cancel, and outside Ω_{R} the second and third terms cancel.

Given this expression for the full wavefunctions, the pseudo-operators $\tilde{A}$

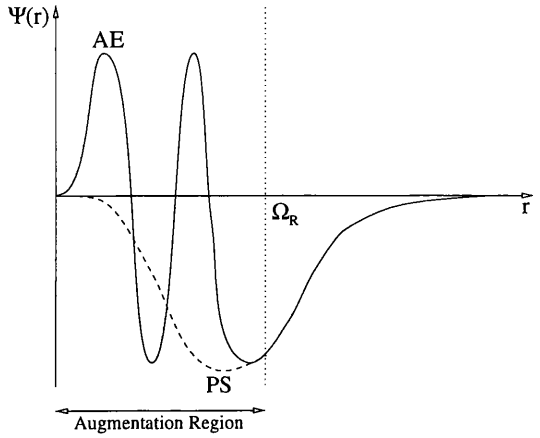

Figure 2.2: Schematic representation of the terms in the PAW expansion of the electron wavefunctions (Equation (2.49)). The solid line represents a full, all-electron (AE) wavefunction, and the dotted line represents the corresponding pseudo (PS) wavefunction.

are found to be

$$\tilde{A} = A + \sum_{\mathbf{R}\mathbf{R}',ij} |\tilde{p}_{\mathbf{R}i}\rangle \left(\langle \phi_{\mathbf{R}i}|A|\phi_{\mathbf{R}'j}\rangle - \langle \tilde{\phi}_{\mathbf{R}i}|A|\tilde{\phi}_{\mathbf{R}'j}\rangle \right) \langle \tilde{p}_{\mathbf{R}'j}| + \tilde{A}^{\mathrm{nl}}, \tag{2.50}$$

where $\tilde{A}^{\mathrm{nl}}$ is the non-local term (zero for local operators). Since $\tilde{A}$ operates only on the PS wavefunctions, it is possible to add an extra term of the form

$$B - \sum_{\mathbf{R}\mathbf{R}',ij} |\tilde{p}_{\mathbf{R}i}\rangle \langle \tilde{\phi}_{\mathbf{R}i}|B|\tilde{\phi}_{\mathbf{R}'j}\rangle \langle \tilde{p}_{\mathbf{R}'j}| \tag{2.51}$$

to equation (2.50), where B is any operator localised within Ω_{R}, without changing the expectation value of A. This can be used, for example, to modify the effect of the Coulomb potential within the cutoff region, in much the same way as with traditional pseudopotential techniques, to allow a smaller planewave expansion for the pseudowavefunctions.

The above describes the basic ideas behind the PAW method. Implementation of the method requires expressions for the charge density, the total-energy

functional and the Hamiltonian. These can each be shown to consist of three terms:

$$n(\mathbf{r}) = \tilde{n}(\mathbf{r}) + n^1(\mathbf{r}) - \tilde{n}^1(\mathbf{r}), \tag{2.52}$$

$$E = \tilde{E} + E^1 - \tilde{E}^1, \text{ and} \tag{2.53}$$

$$H = \tilde{H} + H^1 - \tilde{H}^1. \tag{2.54}$$

(note that terms on the left represent the pseudo-operators; the tilde now represents the fact that the term depends on the pseudowavefunctions and the superscript '1' indicates dependence on the partial waves). The first terms of equations (2.52) to (2.54) depend only on the smooth part of the wavefunction and can therefore be safely evaluated on a regular mesh; the second and third terms are one-centre terms containing the partial-wave contributions and can be evaluated on atom-centred radial grids. The forces on the electron wavefunctions (or more correctly, the planewave components) can now be calculated using equation (2.29). The forces on the nuclei are complicated by the atom-centred basis set which must be adjusted as the nucleus moves, and the core charge which moves with the nucleus. As a result of this, the nuclear force contains two extra terms known as the Pulay force; furthermore, if MD is to be accurate, the atomic masses must be adjusted to account for the increased effective mass of the ion relative to the bare nucleus.

All that remains then is to provide a method of calculating the partial waves and the projector functions. In the current implementation of the code the AE partial waves $|\phi_i\rangle$ are obtained via self-consistent solution of the radial Schrödinger equation for the free atom at chosen energies ϵ_i^1:

$$\left(-\frac{1}{2}\nabla^2 + v_{\text{at}} - \epsilon_i^1\right)|\phi_i\rangle = 0, \tag{2.55}$$

where v_{at} represents the self-consistent atomic potential. The energies ϵ_i^1 are

chosen such that the scattering properties of the atom are well described for a range of energies around the valence level energy. For an exact description of an arbitrary AE wavefunction within Ω_{R} at a particular energy ϵ_i^1, the index i representing angular momentum must, in principle, range over all possible values of quantum numbers l and m (see equation (2.45)). In practice however, the AE valence wavefunctions in most systems are adequately described by including only the angular momenta of the atomic configuration. It is worth noting that the energies ϵ_i^1 need not be atomic eigenvalues (although they are often chosen as such) and that it is possible to define partial waves for a number of different energies to improve the transferability of the pseudopotential. The PS partial waves are constructed in a manner similar to that by which traditional pseudopotentials are constructed. A PS potential is created by fitting a curve to the AE potential such that the fit is exact outside the augmentation region Ω_{R} and produces the correct logarithmic derivative of the wavefunctions at the cutoff boundary, but does not contain the Coulomb singularity at $\mathbf{r} = 0$. The radial Schrödinger equation is then solved for the PS potential at the AE energies ϵ_i^1. There is no need to enforce the norm-conservation condition on the PS partial waves with the PAW method, although this is always done for those used with this work. The projector functions are then chosen to fulfill the condition $\langle \tilde{p}_i | \tilde{\phi}_j \rangle = \delta_{ij}$.

There are a number of advantages associated with the Projector Augmented Wave method. Firstly, it overcomes the failing of traditional pseudopotential methods with regard to the poor description of first-row and transition-metal valence wavefunctions. The all-electron nature of the technique means that it is also possible to study hyperfine structure (Vanderwalle & Blöchl 1993) where the value of the electron spin near the nucleus is important. Also, the atom-centred partial waves, which have the angular character of spherical harmonics, provide a convenient method of determining the orbital nature of the electrons associated with a particular atom. This property will be used in Chapter 5 to

determine the symmetry of various electronic states in a Jahn–Teller system.

2.8 Tight-Binding Methods

The PAW and general pseudopotential techniques described in the previous sections are all so-called *ab-initio* techniques, *i.e.*, the only parameters of the simulations are the atomic numbers of the constituent atoms and the cell parameters. These *ab-initio* techniques have a number of advantages, the main one being that, for a suitable set of pseudopotentials, they produce extremely accurate electron wavefunctions. High accuracy, however, always carries a price; in this case it is the amount of computer power (time and storage) required to carry out an *ab-initio* simulation. The use of a planewave basis set, being totally 'impartial' (*i.e.*, containing no preconceptions as to the form of wavefunctions), means that fairly large numbers of planewaves are required to describe the wavefunctions. One way around this situation is to use a different basis set, such as atomic orbitals as used in the tight-binding methods (Sutton 1993, McWeeny 1979).

The basic idea behind tight-binding is fairly simple: for each valance electron associated with each atom, assign a probability of that electron 'hopping' to one of the other atoms in the system. In the simplest case it is assumed that the electrons may only hop between two adjacent atom sites and that the overlap between orbitals at adjacent sites is zero. The simplest periodic example is that of a ring of N hydrogen atoms with the atomic basis set limited to one s-state per atom, denoted $|q\rangle$ for the s-state on atom q. Following Sutton (1993) the full wavefunction of the system is then a linear combination of the basis functions:

$$|\Psi\rangle = \sum_{q=1}^{N} c_q |q\rangle, \tag{2.56}$$

and the equation describing the system is

$$\sum_{q=1}^{N} c_q \langle p|H|q\rangle = E \sum_{q=1}^{N} c_q \langle p|q\rangle, \tag{2.57}$$

for some arbitrary state $|p\rangle$. Now, using the orthogonality condition $\langle p|q\rangle = \delta_{pq}$ and assigning the Hamiltonian matrix elements as

$$H_{pq} = \langle p|H|q\rangle = \begin{cases} \alpha & \text{if } p = q, \\ \beta & \text{if } |p-q| = 1, \\ 0 & \text{otherwise,} \end{cases} \tag{2.58}$$

then, since all sites are equivalent, the problem becomes one in solving

$$\beta c_{q-1} + \alpha c_q + \beta c_{q+1} = E c_q. \tag{2.59}$$

The solution to equation (2.59) is

$$c_q^{(n)} = N^{-\frac{1}{2}} \exp\left(i\frac{2\pi qn}{N}\right), \tag{2.60}$$

with eigenvalues

$$E^{(n)} = \alpha + 2\beta \cos\left(\frac{2\pi n}{N}\right), \tag{2.61}$$

where $i = \sqrt{-1}$ and n is the set of integers (quantum numbers) $0 \leqslant n \leqslant N-1$ arising from the periodicity of the cell. Taking this to the limit $N \to \infty$ and assigning the continuous variable $k = 2\pi n/N$ gives

$$c_q(k) = N^{-\frac{1}{2}} e^{iqk} \tag{2.62}$$

and

$$E(k) = \alpha + 2\beta \cos k. \tag{2.63}$$

Combining Equation (2.62) with (2.56) shows how the system obeys Bloch's theorem, and Equation (2.63) gives the E-k dispersion relation.

The above description can easily be expanded in order to describe real 3D lattices containing different atoms by including extra orbitals in the basis set, more off-diagonal (longer-range hopping) elements in the Hamiltonian and correcting for the overlap of the basis sets on adjacent atoms. The hopping parameters H_{pq} can be determined by fitting the band structure to experimental data or *ab-initio* simulations. Since the Tight-Binding methods (although they can in principle be regarded as approximations to *ab-initio* DFT) are based on fitted parameters, they are not as accurate as *ab-initio* methods when applied to different situations and therefore their predictive power is more limited. In addition, the orbital basis does not describe the vacuum tails of the wavefunctions at a surface very well, which is an important consideration when simulating the Scanning Tunnelling Microscope. They do, however, have several advantages over the *ab-initio* techniques. The atomic-orbital basis means that the number of electrons associated with a particular atom (and hence the atom charge) and the orbital nature of the electrons around the atom (useful for calculating the symmetry of a state) can easily be found. Tight-binding can also be use to calculate total energies (Sutton, Finnis, Pettifor, & Ohta 1988) and is particularly good at interpreting the features in band-structure; for example, high-frequency components in the band-structure imply the existence of long-range interactions within the material (*i.e.*, non-zero, long-range hopping terms in the Hamiltonian). There is also the advantage that tight-binding calculations are less computationally expensive and hence larger simulation cells may be used. This situation is improving further with

the development of so-called Order-n (written $O(n)$) methods (Galli 1996, Li, Nunes, & Vanderbilt 1993) where the computational resources required for a calculation scales linearly with the system size as opposed to conventional methods, such as Car–Parrinello, where the workload scales with the cube of the system size. The $O(n)$ techniques make use of the localised basis set, and the fact that the bonding is determined largely by short-range interactions, to eliminate the need to calculate the eigenvalues or eigenstates of the full single-particle Schrödinger equation. Instead, the system is split into several smaller, overlapping sub-systems and Schrödinger-like equations are solved for the (coupled) sub-systems. With the $O(n)$ methods simulations containing $\sim 10^4$ atoms may be carried out on parallel computers, compared to, *e.g.*, conventional DFT calculations where the upper bound is $\sim 10^2$ atoms.

Chapter 3

The Scanning Tunnelling Microscope

3.1 Introduction

The Scanning Tunnelling Microscope (STM) is arguably one of the most important developments for the study of surfaces in recent years. The STM was conceived by Binnig & Rohrer (1987) in the late 1970's with the intention that it would provide local spectroscopic information on sample surfaces on the nanometre scale. They soon realised, however, that the STM would also provide a real-space imaging device with a resolution capable of picking out individual atoms on a surface. They received the Nobel Prize for Physics in 1986. The STM is now just one of a large family of so-called Scanning Probe Microscopes (SPM) collectively capable of studying almost any property of a surface, often on the atomic scale.

3.1.1 Uses of the Scanning Tunnelling Microscope

The STM is in common use in experimental laboratories across many disciplines and has been instrumental in a number of important scientific advances.

For example, early use of the STM confirmed the nature of the reconstructions at the Si (111) 7×7 and the Si (100) 2×1 surfaces, as well as shedding light on the behaviour of materials at step edges—information virtually impossible to obtain with the same level of detail by any other technique. The STM has also found a great deal of use in studying adsorbates on surfaces, including organic and even biological molecules—the way molecules arrange on a surface is of particular importance to the liquid crystal and micro-electronics industries as well as to engineers interested in lubrication. For example, the work of Patrick, Victor, Thomas, & Beebe (1994) shows that a monolayer of large organic molecules self-assemble into a highly ordered structure inside 'molecular corrals' (circular monolayer etch pits) on the Highly Oriented Pyrolytic Graphite (HOPG) surface.

The imaging of surfaces on the atomic scale is of obvious importance to both pure science and industry, but the STM is by no means restricted to such uses. The pioneering work of Eigler et al. (1990, 1991) showed that it was possible to transfer reversibly a xenon atom from a nickel surface to a tungsten tip, effectively creating a monatomic switch. Many groups are now able to move adsorbates around on surfaces; for example individual C_{60} molecules, or even whole rows of molecules (Beton, Moriarty, Dunn, Ma, & Upward 1996) can be pushed along channels in the Si(001) surface with the STM tip. 'Bucky tubes' can be manipulated with the tip and disentangled in real time using a finger-controlled STM (Superfine 1997). Crommie, Lutz, Eigler, & Heller (1996) showed that rearranging iron atoms adsorbed on the copper surface into a ring caused the electrons to form a standing-wave pattern within the ring that could be imaged directly with the STM. Manipulation with the STM is not restricted to adsorbates though. Voltage-pulsing with the STM tip over various surfaces can produce structures varying in size from the nanometre sized mounds on gold (Mamin, Guethner, & Rugar 1990), to monatomic pits in silicon (Lyo & Avouris 1991, Uchida, Huang, Grey, & Aono 1993, Kobayashi,

Grey, Snyder, & Aono 1993) with obvious implications for the micro-electronics and micro-engineering industries.

3.1.2 STM Structure

Despite the variety of ways in which the STM family have been used, the constituent parts and general operating mechanism are quite simple. An (ideally) atomically sharp metallic tip, usually made of tungsten, is positioned above a conducting sample with either the tip or sample mounted on a piezoelectric positioning device (often a tripod, but other designs are possible (Weisendanger 1994)) allowing continuous motion in three dimensions. In reality an STM tip is not atomically sharp, but will look something like that shown in Figure 3.1, *i.e.*, a large-radius (blunt) bulk of metal with many 'mini-tips' protruding from the base. However, all that is required is that one of the mini-tips protrudes about 1Å further than the rest and this condition is often satisfied. A course-alignment screw allows medium-range motion of either the tip or the sample so that they can be brought to within a micrometre of each other. From there the piezoelectric drives can take over and vary the tip–sample separation continuously. The voltages across the various positioning piezoelectrics and between the tip and sample are controlled by some circuitry via a computer.

Under typical operating conditions, the tip–sample bias must be maintained to greater than millivolt accuracy, and the separation maintained to better than picometre accuracy. Hence, sophisticated feedback circuitry and vibration isolation are required (as pointed out in Weisendanger (1994), typical floor vibrations in a lab are of order 1μm). An effective method of damping background motion is mounting the STM on several slabs of viton- or rubber-separated metal and suspending the whole system from a set of springs. Ultra High Vacuum (UHV) conditions are also essential for the study of clean sur-

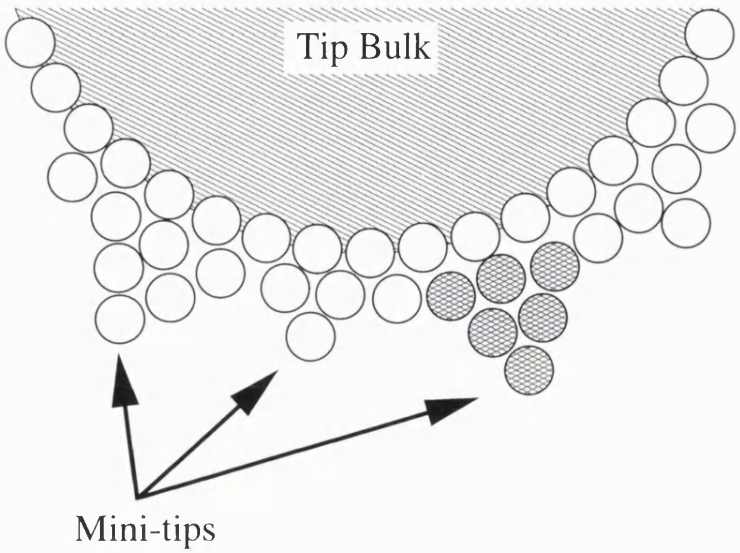

Figure 3.1: A real STM tip is not 'atomically sharp' in the obvious sense of the phrase, but in fact is rather blunt and covered with a series of small protrusions (mini-tips). Luckily, the (approximately) exponential dependence of the tunnelling current on tip–sample separation means that the majority of the tunnelling current flows through the mini-tip closest the surface (shaded atoms).

faces on the atomic scale, particularly with regard to reactive surfaces such as silicon. Any impurities (such as oxygen in the air) can seriously degrade the image quality and introduce doubt as to the exact nature of the surface under study. Mounting the STM in a UHV chamber is common practice, but this introduces problems related to placing the samples in the sample holders in the first place. Either samples must be grown in a UHV chamber adjoining the STM chamber and passed through, or grown elsewhere and capped with a layer of material which can then be etched away in the STM chamber.

3.1.3 STM Operation and Imaging Modes

In operation, the STM tip is moved to within a few angströms of the conducting sample surface such the the electronic orbitals of the tip and sample overlap.

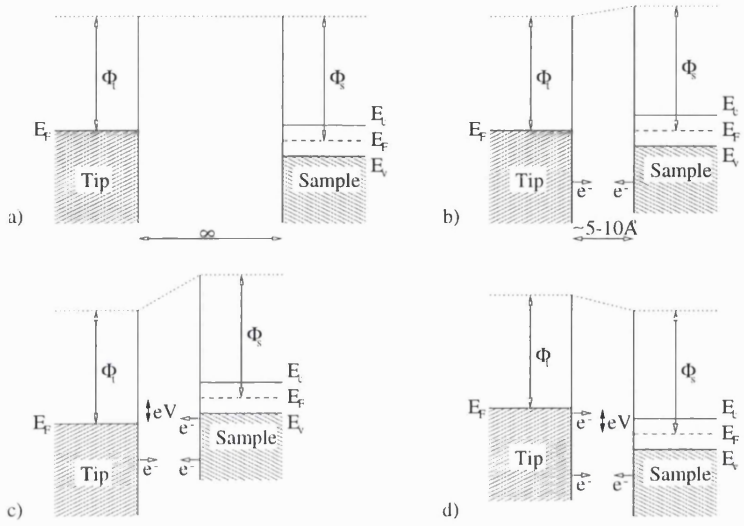

Figure 3.2: Schematic representation of the STM tip–sample bands for a metallic tip and semi-conducting sample. a) When the tip and sample are well-separated, their vacuum levels are equal; b) with the tip and sample close together under thermal equilibrium, their Fermi levels equalise by the transfer of charge between the two electrodes (setting up the 'contact potential'); c) under a tip-positive bias there will be a net current as the electrons from the sample valence levels flow into the tip conductance band; and d) with a tip-negative bias a net current will flow from the tip to the sample.

An overlap of electronic wavefunctions implies that a tunnelling current can flow between the two electrodes—of course, under equilibrium the net current between the tip and sample will be zero. However, upon application of a bias there will be a net flow of electrons from the negative electrode to the positive electrode as the electrons from the filled states in the negative electrode tunnel into the empty states of the positive electrode (Figure 3.2). The magnitude of this tunnelling current will depend on many things including the tip–sample separation (through the wavefunction overlap), the electronic density of states (DoS) of both the tip and sample, and the shape of the barrier between them. It is this complicated dependence on the local atomic and electronic structure that makes the STM so versatile. Spectroscopy (the reason that the STM was invented) relies on the fact that as the tip–sample bias varies, different tip and

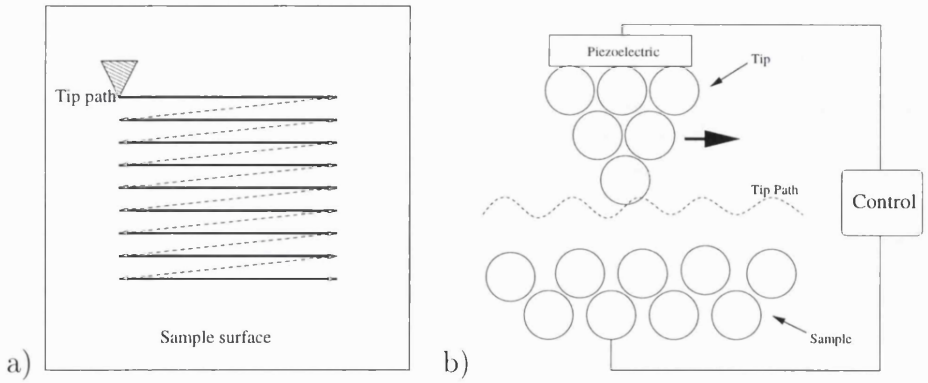

Figure 3.3: The Scanning Tunnelling Microscope operating in constant current mode. a) The tip is rastered across the surface and b) a feedback loop between the tip and sample varies the tip–sample separation in order to keep the tunnelling current constant.

surface states will contribute to the tunnelling current. Therefore an I–V curve will contain information related to DoS of the tip and sample; however, it is far from simple to regain the DoS from the STM data (Weisendanger 1994).

As already mentioned, the first popular use of the STM was to generate topographic images of surfaces on the atomic scale. There are two operating modes used for imaging surfaces. In the first, Constant Current (CC) mode, the tip is rastered across the surface and a feedback loop between the tip and sample varies the height of the STM tip in order to keep the tunnelling current constant (see Figure 3.3). The voltage applied across the z-piezo as a function of x- and y-piezo voltage forms the image of the surface. This mode is the most commonly used mode, but the speed of image production is limited by the response time of the height-controlling piezo. Constant Height (CH) mode gets around this limitation as the tip is rastered in a plane and the tunnelling current as a function of x and y piezo voltage forms the image. This will produce a topographic image that approximately exponentially exaggerates the surface corrugation (owing to the exponential separation dependence of the tunnelling current) compared to CC mode. CH mode also has the problem

that the tip may crash into the surface due to sample misalignment or may collide with a large surface feature. This effect is minimised in CC mode where the feedback loop will (for a suitable choice of gap resistance) ensure that tip–sample collisions do not occur. CC is also often used to position the tip before performing spectroscopy or surface modification.

Using these techniques, the surface topography of a sample can be obtained on the atomic scale. Since the current depends on the wavefunction overlap, it is roughly exponentially dependent on the tip–sample separation. This gives a vertical resolution of around 1pm (and explains why non-ideal tips work) and, since practically all current will flow through the tip apex atom, the lateral resolution is around 1Å. However, if the 'topographic' image generated with the STM really was related only to the atomic structure of the surface, the instrument would not be nearly as useful as it is. The complicated dependence of the tunnelling current on many variables means that in many cases, particularly where defects or adsorbates are present, direct interpretation of the STM data in terms of surface topography or surface DoS is not possible. As a result of this, a great deal of effort is being put into finding a general scheme to predict STM tunnelling current, and hence the STM images, which is also amenable to computer calculations.

3.1.4 Other Operating Modes

There are several other operating modes of the STM which are not of direct relevance to this thesis, but are of general interest. In Scanning Tunnelling Spectroscopy (STS), the d.c. bias voltage is modulated by a small, high frequency sinusoidal voltage (high enough so that the constant-current feedback amplifiers cannot react). The STM is then operated in CC mode, such that a normal topograph is obtained, but in addition the high-frequency modulation of the tunnelling current gives the differential current $\frac{dI}{dV}$ at the d.c. bias.

It is also possible to obtain the spectroscopic curve $\frac{dI(V)}{dV}$ over a range of bias voltages, V, by positioning the tip above the desired location and continuously varying the applied bias across the desired range with the feedback mechanism switched off. Combining this with the CC imaging mode, the tip can be stopped at regular intervals, but always at the same gap-resistance, and full I–V curves obtained. In this way a spectroscopic map of the entire surface may be obtained—this technique is known as Current Imaging Tunnelling Spectroscopy (CITS). For a more complete summary of the operating modes of the STM see, for example, Weisendanger (1994).

3.2 STM Image Calculation

In order to predict or explain the images produced by the STM one must have a means by which to calculate the tunnelling current. There are various methods which could be used, the simplest of which (used for this work) is the Tersoff-Hamann (TH) approximation (Tersoff & Hamann 1985) which is based on the perturbative Bardeen tunnelling formalism (Bardeen 1961). The Bardeen tunnelling formalism provides an expression for the tunnelling current between two semi-infinite conductors across a vacuum gap. Using first-order time-dependent perturbation theory to calculate the probability of electron transfer from a state ψ_s in one conductor to a state ψ_t in the other (Figure 3.4), Bardeen showed that the total tunneling current can be expressed as

$$I = 2\pi \sum_{s,\ t} f(E_s)\left[1 - f(E_t + eV)\right] |M_{st}|^2\, \delta\left(E_s - E_t\right). \tag{3.1}$$

Here, $f(E)$ is the Fermi function at energy E, V is the applied bias, and M is the transfer-Hamiltonian whose elements M_{st} are given by

$$M_{st} = -\frac{1}{2}\int \mathbf{ds}.\left(\psi_s^* \nabla\psi_t - \psi_t \nabla\psi_s^*\right), \tag{3.2}$$

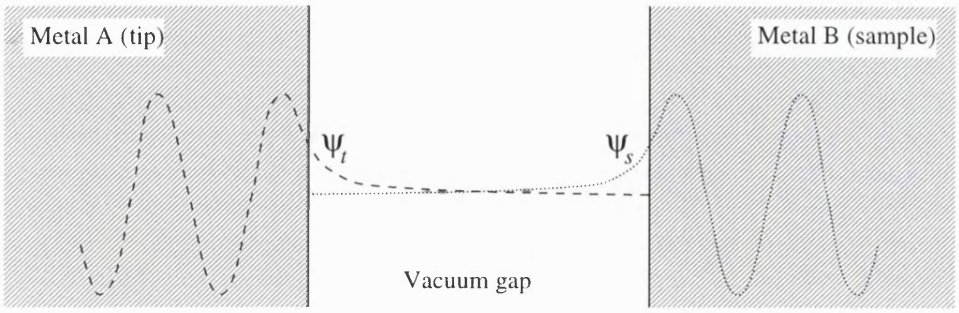

Figure 3.4: Schematic of the system considered in the Bardeen tunnelling formalism. The tip (sample) wavefunctions are only valid in the tip (sample) region and the vacuum gap. The tunnelling of an electron from state ψ_t in the tip to state ψ_s in the sample is determined only by the overlap in the gap region.

where the integration is over a surface spanning the vacuum gap. The ψ_t and ψ_s here are wavefunctions which are eigenstates of the Hamiltonian both in the metal from which they originate (Metal A and Metal B respectively in Figure 3.4) and the vacuum gap separating the two metals. What Equations (3.1) and (3.2) say is that the tunnelling current is proportional to the current operator evaluated between the states ψ_t and ψ_s. This formalism as described so far is geometry independent—Tersoff and Hamann (Tersoff & Hamann 1985) took the step of applying this formalism to the specific geometry of the Scanning Tunnelling Microscope.

The Tersoff-Hamann approximation is based on two main assumptions: first, the tip is assumed to be well-approximated by a spherical potential well, and secondly, the interaction between the tip and surface is assumed to be small. The sample surface is treated 'exactly' within whatever electronic structure scheme is desired. Figure 3.5 shows a schematic diagram of the assumed geometry. Assuming the surface normal points along the z direction, the surface wavefunctions in the vacuum gap (*i.e.*, where the vacuum Schrödinger

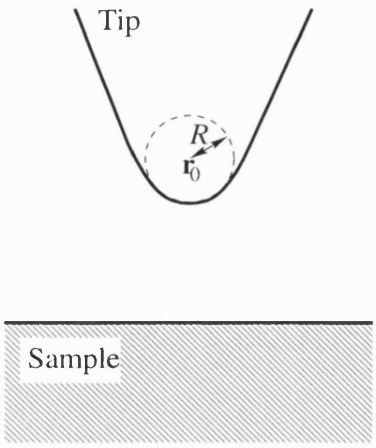

Figure 3.5: The Tersoff–Hamann approximation treats the surface exactly (within some electronic structure scheme) and assumes the tip may be approximated by a spherical potential well of radius R centred on $\mathbf{r}_0$.

equation applies) can be expanded as

$$\psi_s = \Omega_s^{-\frac{1}{2}} \sum_{\mathbf{G}} a_{\mathbf{G}} \exp\left[-(\kappa^2 + |\mathbf{k_G}|^2)^{\frac{1}{2}} z\right] \exp\left(i\mathbf{k_G}.\mathbf{x}\right) \tag{3.3}$$

where Ω_s is the sample volume; $\mathbf{k_G} = \mathbf{k}_{||} + \mathbf{G}$, where $\mathbf{k}_{||}$ is a surface Bloch wave vector of the state ψ_s; $\mathbf{G}$ is a surface reciprocal lattice vector; $\kappa = \sqrt{2\phi}$ is the minimum inverse decay length for a material with workfunction ϕ; and $\mathbf{x}$ is used to denote vectors parallel to the surface. Note that Equation (3.3) assumes a crystalline (*i.e.*, periodic) system, as is present in the calculations presented here, but the Tersoff–Hamann model is not restricted to crystals.

The tip wavefunctions are assumed to have the form of asymptotically decaying spherical waves (*i.e.*, the tip has s-state symmetry) centred on the centre of curvature of the tip, $\mathbf{r}_0$:

$$\psi_t = \Omega_t^{-\frac{1}{2}} c_t \kappa R e^{\kappa R} \frac{\exp\left(-\kappa|\mathbf{r} - \mathbf{r}_0|\right)}{\kappa|\mathbf{r} - \mathbf{r}_0|}, \tag{3.4}$$

where Ω_t is the tip volume, κ is the inverse decay length described above

(assuming the work functions of both tip and sample are equal), and c_t is a constant of proportionality dependent on the tip geometry and electronic structure.

Rewriting Bardeen's expression for the tunnelling current (Equation (3.1)) in the context of the STM with a small tip–sample bias V at low temperature gives

$$I = 2\pi V \sum_{s,\ t} |M_{st}|^2 \delta(E_s - E_F)\delta(E_t - E_F), \tag{3.5}$$

where a 'small' bias is one in the region where the system has a linear current–voltage curve. Now, expanding the tip wavefunctions (3.4) in the same form as the surface wavefunctions (3.3) and substituting into the Bardeen transfer matrix (3.2) leads to an expression for the tunnelling current of the form

$$I = 32\pi^3 V \phi^2 D_t(E_F) R^2 \kappa^{-4} n_s(\mathbf{r}_0, E_F), \tag{3.6}$$

where D_t is the tip density of states and

$$n_s(\mathbf{r}, E) = \sum_s |\psi_s(\mathbf{r})|^2 \, \delta(E - E_s) \tag{3.7}$$

is the surface electron density at energy E and position $\mathbf{r}$. The tunnelling current within the Tersoff–Hamann approximation then, is proportional to the surface electronic density of states at the Fermi level measured at the centre of curvature of the tip.

So, within the Tersoff–Hamann approximation, an STM operating in the constant current imaging mode will trace out a surface of constant density of states at the Fermi level. From this definition it is unsurprising that the STM images of surfaces, particularly those where defects or adsorbates may be present, cannot always be related to the actual 'surface topography'. The

Tersoff–Hamann approach is widely used in STM simulations to predict the STM image for the system under study and has been successful in many cases. There are of course still problems with the approximation. The assumption that the tip may be represented by s-like states is not likely to be valid given that most tips are made of tungsten, whose d states contribute most of the valence level density of states. This problem can in principle be tackled by simply including extra terms in the expansion of the tip wavefunctions. Tsukada & Shime (1987) have extended the Tersoff–Hamann approximation to treat the tip and sample equally, although still within perturbation theory, to give the differential tunneling current as

$$\frac{dI}{dV} \propto \sigma_{\mathrm{t}} \left(E_{\mathrm{F}} - eV\right) n_{\mathrm{s}} \left(\mathbf{r}_0, E_{\mathrm{F}} - eV\right), \tag{3.8}$$

where $\sigma_{\mathrm{t}}\left(E\right)$ is the effective density of tip states at energy E and other terms are as previously defined.

Both of the above theories are based on perturbation theory, and implicitly make the assumption that the tip–sample interactions will be small (more specifically, that the potential in the gap is vacuum-like). At the tip–sample separations in Scanning Tunnelling Microscopy ($\leqslant$ 10Å) this is not the case (see Section 6.4, Ciraci, Baratoff, & Batra (1990) and Hirose & Tsukada (1994)). Chen (1990) has extended the Bardeen formalism and solved (3.2) for a number of different tip states. The transition-Hamiltonian elements are calculated for an interacting tip–sample system, where the effect of the tip on the surface is treated as a perturbation. The interacting wavefunctions (modified wavefunctions) can then be obtained by solving a Dyson equation in the non-interacting wavefunctions. Using this approach, the transition-Hamiltonian elements turn out to be related to the partial (spatial) derivatives of the unmodified surface wavefunctions evaluated at the tip apex.

Pendry, Prêtre, & Krutzen (1991) have developed an exact formalism for

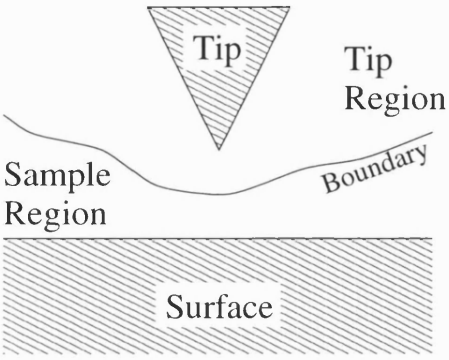

Figure 3.6: The assumed geometry in the Pendry tunnelling current method (Equation (3.9)). An impenetrable barrier is erected in the vacuum gap between the tip and sample, and then systematically removed in order to calculate the contributions of the tip and sample states to the wavefunction at the boundary.

the tunneling current. The theory starts by erecting an impenetrable barrier between the tip and sample (Figure 3.6) and proceeds by considering the effect on the wavefunctions as the barrier is removed by additional potentials v_s to the sample and v_t to the tip. The differential conductance can then be shown to be given by the Landauer (1957) formula

$$\frac{dI}{dV} = \frac{2}{\pi}\mathrm{Tr}\left(t^{\dagger}\Im\left(G_{\mathrm{t}}\right)t\Im\left(G_{\mathrm{s}}\right)\right), \tag{3.9}$$

where $\mathrm{Tr}\left(A\right)$ denotes the trace of the matrix A, G_{t} and G_{s} are the tip and sample Green's functions respectively when the impenetrable barrier is in place, $\Im\left(G\right)$ represents the imaginary part of the Green's function G (related to the electronic density of states), and

$$t = v_t\left(1 - G_s v_s G_t v_t\right)^{-1} \tag{3.10}$$

is the transition matrix when the connection between the tip and sample is restored. In other words, the matrix t is the operator which, when acting between the Green functions G_{s} and G_{t}, gives the mixing of the tip and sample

states as the barrier is removed.

Equation (3.9) in principle provides an exact method via which to calculate the tunnelling current. The problem with regard to simulation is that the potentials v_t and v_s are effectively infinite and vary at each tip position, making evaluation extremely difficult. Todorov, Briggs, & Sutton (1993) have improved the situation by obtaining essentially the same result (Equation (3.9)) by considering the elastic current flow between two semi-infinite systems through some 'small' (relative to the inelastic mean free path of the electrons) elastic scatterer. In this case though, the derivation was based on a tight-binding description of the electrons (but is not restricted to such), and the separating potential was not assumed to be infinite.

Ness & Fisher (1997b) have also proposed a convenient mechanism to obtain the tunnelling current from the Landauer formula (Equation (3.9)). Causal Green functions are used to obtain the probability of electrons tunnelling from a localised state in the tip, $|i\rangle$, to a localised state in the surface, $|f\rangle$, and a simple expression for the tunnelling current involving the overlap of $|i\rangle$ and $|f\rangle$ with the eigenstates of the system is obtained. Although the method currently lacks a full description of the tip, it enables direct calculation of STM images from the results of total-energy calculations, without the need to resort to more simplistic perturbative methods such as the Tersoff–Hamann approximation.

Doyen (1996) reports an exact method of calculating the tunnelling current more amenable to calculations than the Pendry method. Here 'exact' means exact for any given potential, within the one-electron approximation. The tip and surface are assumed to be planar electrodes and the tip apex is assumed to be a single atom or cluster of atoms adsorbed on the tip electrode. The tip is in effect a localised perturbation to what is otherwise merely a capacitor, and hence the exact Green function of the tip–sample system can be obtained from a Dyson equation in terms of the Green function of the capacitor. The

tunnelling current can then be calculated using scattering theory.

As described, the above methods are merely mechanisms via which to calculate the tunnelling current for a given surface (and tip) geometry. They do not explicitly take into account the fact that the presence of the tip may well have a measurable effect on the actual atomic, as well as electronic, structure of the surface. If a lattice distortion occurs, then any of the above methods could produce an incorrect STM image. The only complete solution to this problem is to explicitly include a tip and full tip–surface relaxation in the STM image calculation. Altibelli, Joachim, & Sautet (1996) have gone part of the way by carrying out STM image calculations on MoS_2 which included the bulk and apex of the tip as well as the sample bulk and surface, but no atomic relaxation. The technique is based on a tight-binding description of the electrons and the current is calculated using a multi-channel scattering approach similar to that of Doyen (1996). In principle, the technique is not restricted to a tight-binding description of the electrons, but a more accurate alternative would result in each image taking longer to generate. Since, as it stands, each image required around 100 CPU hours on a Cray C98 this is impractical for most purposes. (This work is discussed further in Chapter 5.)

Where the calculation of STM images is required, the work described in this thesis uses Equation (3.8) with the tip assumed a perfect metal (*i.e.*, constant DoS) and the surface electronic density of states approximated by

$$n_{\mathrm{s}}(\mathbf{r}, E) = \frac{1}{\pi} \lim_{\eta \to 0} \sum_{i} \frac{\eta}{(E - \epsilon_i)^2 + \eta^2} |\psi_i(\mathbf{r})|^2 \tag{3.11}$$

where η is a Lorentzian broadening factor, in effect simulating the effect of dispersion on the Kohn-Sham orbitals, and all other symbols are as previously defined. Integration of (3.8) leads to an easily calculated expression for the

tunnelling current:

$$I \propto \lim_{\eta \to 0} \sum_i \left[\tan^{-1}\left(\frac{E_\mathrm{F} - \epsilon_i}{\eta}\right) - \tan^{-1}\left(\frac{E_\mathrm{F} - eV - \epsilon_i}{\eta}\right) \right] |\psi_i(\mathbf{r}_0)|^2 . \tag{3.12}$$

All calculated STM images are obtained directly from this expression with a Lorentzian broadening factor of $\eta = 0.6$eV, and an applied tip-bias of $+0.8$V unless explicitly stated otherwise. Appendix A summarises the conventions used in generating the STM images in this thesis.

Chapter 4

The Transition-Metal Dichalcogenides

4.1 Introduction

4.1.1 Atomic Structure

The transition-metal dichalcogenides (TX_2 where T represents a transition metal from column IVB, VB or VIB in the periodic table, and X represents one of the chalcogens S, Se or Te) have become widely used materials by engineers and physicists alike owing to their useful chemical and physical properties.

The TX_2 family can form in one of many different structures, but they all have the same basic form. Hexagonal layers of metal atoms are sandwiched between two hexagonal layers of chalcogen atoms and these X–T–X sandwiches are stacked on top of each other in a van-der-Waals-bonded layer structure. The difference in structures arises from the relative alignment of the chalcogen layers within the sandwich and the number of the sandwiches in a unit cell (*i.e.*, the stacking sequence). In addition, in some TX_2 materials (*e.g.*, WTe_2) the layers are buckled (Dawson & Bullet 1987). All TX_2 materials of direct interest to this thesis form in the 2H (**2** layers per cell in a **H**exagonal structure) form

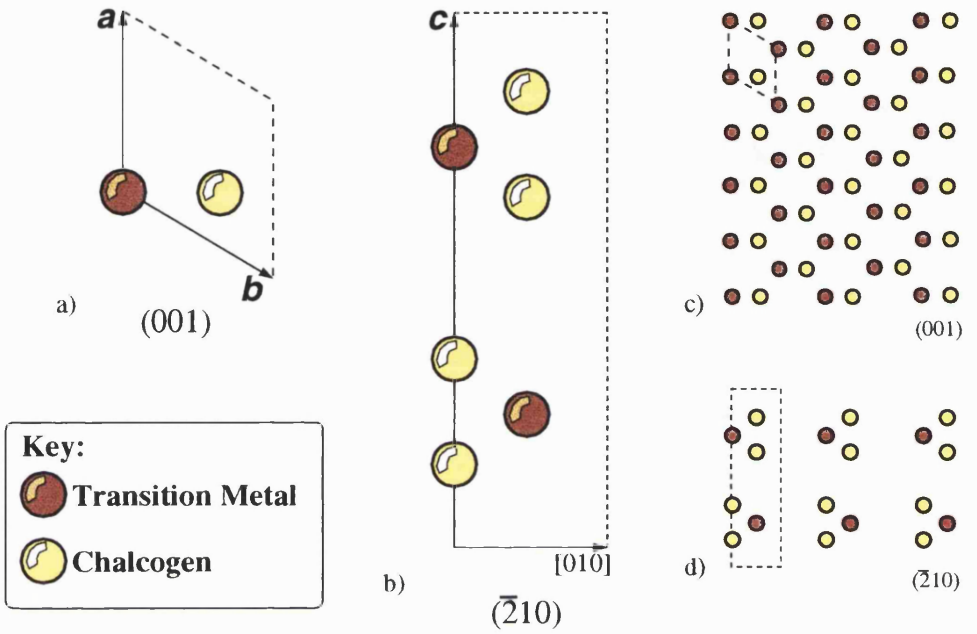

Figure 4.1: Schematic diagrams of the atomic structure of the 2H transition-metal dichalcogenides: a) shows the unit cell in the (001) plane, b) shows the unit cell in the $(\bar{2}10)$ plane, c) and d) show the tessellated structure in the same planes.

shown in Figure 4.1 where the hexagonally arranged chalcogen atoms within a sandwich are aligned along the c-axis, and the unit cell contains two sandwich layers with the chalcogens of one sandwich vertically aligned with the metal atom of the other.

Figure 4.2 shows the Brillouin Zone and symmetry points of the structure. The conductivity of the TX_2 depends on the transition metal type: those with group IVB or VIB metals are generally semi-conducting at room temperature, whereas those with group VB metals are conducting. In addition, the conductivity depends greatly on the crystal orientation—the c-axis conductivity is much lower than that in the plane of the layers. The conduction state and anisotropy can be changed by introducing intercalates between the layers. Many of the TX_2s are also superconducting at low temperatures.

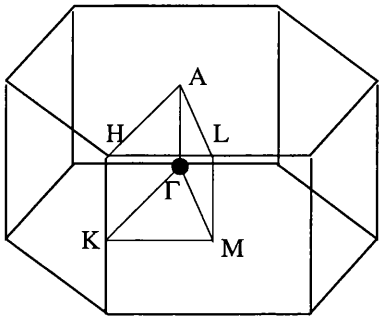

Figure 4.2: Schematic diagram of the Brillouin Zone of the 2H transition-metal dichalcogenides.

4.1.2 Uses and Literature Survey

The transition-metal dichalcogenides are useful materials for industry as well as pure science. The van der Waals bonded nature of the layers means that there is little resistance to layers sliding over each other and that atomically flat surfaces may be produced by cleaving. Consequently the TX_2 make extremely good solid lubricants (Fleischauer 1987), and are ideal surfaces on which to carry out STM studies as virtually perfect surfaces can easily be produced within the STM vacuum chamber. Furthermore, the presence of the transition metal, whose oxidation state can vary, means that the materials can also act as catalysts. It is therefore important that we understand the behaviour of the surface and it is to this end that many experimental and theoretical studies have been carried out.

The chemical, physical and electronic properties (the bulk and surface band structures) of these materials have been extensively studied (Dawson & Bullet 1987, Kobayashi & Yamauchi 1995) and the members of the family share a number of common properties. There are also many groups using STMs to examine the surfaces under various conditions. However, interpretation of STM images on any surface has always been problematic and the transition-metal dichalcogenides are no exception. There was a long-term debate as to

whether the peaks in the filled-state images of the TX_2 surfaces were due to the metal atoms, whose *d* levels provide most of the density of states at the top of the valence band, or the chalcogen atoms, which are physically closer to the tip. Simulation studies (Kobayashi & Yamauchi 1995, Magonov & Whangbo 1994, Altibelli et al. 1996), including Section 4.3 here, have provided insight into the problem and it is now generally agreed that under normal STM operating conditions it is probably the surface chalcogen atoms that are imaged. However, recent STM image calculations on MoS_2 which included the tip explicitly (Altibelli et al. 1996) indicated that the image contrast will change if the tip–sample separation is reduced to less than 4Å, such that the peaks in the image occur between the surface-projected chalcogen and metal sites (*i.e.*, the peaks do not occur directly over an atom of any type). This contrast change can be explained by noting that as the tip approaches the surface, the contribution to the tunnelling current from the metal *d*-states will increase and may at some point become of the order of the contribution from the chalcogen *p*-states.

There is also much attention being paid to the fabrication of nanostructures on the surface. Experimental STM work such as that by Fuchs and Schimmel has studied the effects of voltage pulsing on clean surfaces of WSe_2 (Fuchs, Schimmel, Lux-Steiner, & Bucher 1992, Fuchs, Schimmel, Akari, Eng, Anders, Lux-Steiner, & Dransfield 1993) and MoS_2 (Fuchs 1996). Figure 4.3 shows constant height STM images of several features created on the WSe_2 surface ranging in size from angstroms (atom-sized holes and 'trimer' peaks) to several nanometers (blisters and rings)—the underlying source of these structures and the mechanisms by which they are produced is open to debate and provide an interesting problem for simulation. There are a number of potential explanations for the defects observed. The large blisters and pits could be due to tip-induced surface deformations occurring in areas of local surface hardness variation (Whangbo, Ren, Magonov, Bengel, Parkinson, & Suna 1995),

or may be genuine features of the surface resulting, for example, from a localised, field-induced build up of interstitial atoms between the TX_2 layers. Recent work by Kobayashi (1997) demonstrates that the large ring-like structures could be interference fringes from electrons scattered from point defects far below the surface. The smaller monatomic-hole and trimer-peak vacancies are more likely to be due to monatomic vacancies or substitutions. Whangbo et al. (1995) have carried out semi-empirical Extended Hückel Tight Binding (EHTB) calculations on the MoS_2 surface with point defects including vacancies and likely substitutions and produce STM images which could explain the small hole and trimer structures. Chapter 5 examines the same problem using the PAW method and reaches the same conclusions—the hole and trimer defects are probably caused by surface-chalcogen and sub-surface-metal vacancies respectively.

Hosaka, Hosoki, Hasegawa, Koyanagi, Shintani, & Miyamoto (1995) have also been modifying the surface of MoS_2 with the STM and have been able to pattern stable nanometer sized letters by extracting a series of selected sulphur atoms (Figure 4.4). Suspected monatomic-vacancy defects have also been observed on the WTe_2 surface by Crossley, Myhra, & Sofield (1994); in this case though, the defect patterns are more complicated (WTe_2 has a buckled structure) and show a definite bias dependence. The TX_2s are not the only materials that are amenable to surface modification however: there are many groups working on the modification of gold (Mamin et al. 1990, Lebreton & Wang 1994, Mizutani, Ohi, MotoMatsu, & Tokumoto 1995) and silicon (Uchida et al. 1993, Huang, Grey, & Aono 1995). One feature universal to all experiments of this kind is that the mechanisms behind the modification are not fully understood.

There are a number of possible contributing factors to the process of atom-extraction. Typical tip–sample separations under modification conditions are believed to be less than or around 5Å (Hosaka et al. 1995) and it is not unrea-

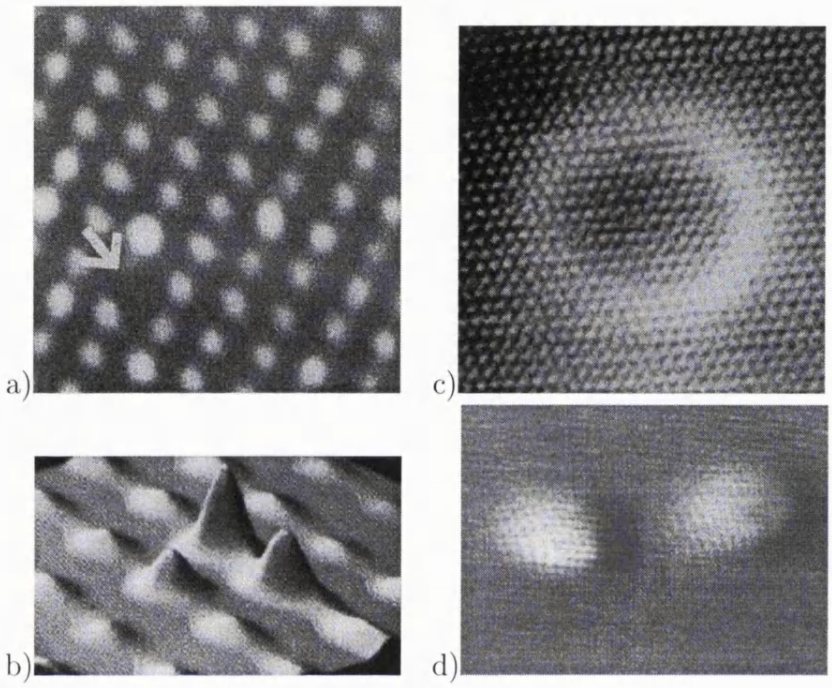

Figure 4.3: Constant height STM images of tip-induced defects on WSe_2 obtained by Fuchs et al. (1992, 1993): (a) monatomic hole defect due to missing surface Se atom; (b) trimer peak defect due to missing sub-surface W atom; (c) and (d) larger defects of unknown constitution.

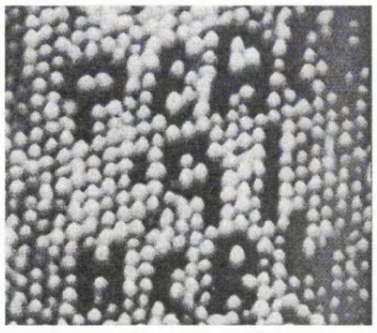

Figure 4.4: Characters etched onto the surface of MoS_2 by Hosoki et al. (1992). The characters were created by applying a 70ns 5V voltage pulse to the STM tip to remove selected S atoms one at a time. (Image taken from Weisendanger (1994).)

sonable to expect the tip–sample interaction to play a large part in reducing the extraction barrier. The electric field between the tip and sample is also likely to be a factor. The Field Ion Microscope (FIM) (Müller & Tsong 1969) has been around much longer than the STM and its operation is based on the emission of ions from a tip under the application of a large bias. However, fields of order 30Vnm^{-1} are required to induce desorption with the FIM compared to fields around 10Vnm^{-1} in the STM, so the bias-induced field alone cannot account for the process. Baskin, Drozdov, & Vladimirov (1996) have proposed that thermal expansion of the tip can cause a tip–sample collision which may be the source of defect formation. Whilst this seems possible for the larger 'bump' and 'pit' features such as those seen in Figure 4.3d and on gold (assuming the observed feature size corresponds to the actual size), it seems unlikely that such a process could explain the reproducible nature of the monatomic defects. Another possibility is that the flow of current from the tip to sample (or vice versa) results in the filling of surface anti-bonding states (or hole in the bonding states) which would weaken the bond, thus lowering the barrier (Salam, Persson, & Palmer 1994, Avouris, Walkup, Rossi, Akpati, Nordlander, Shen, Abeln, & Lyding 1996). The actual mechanism is probably going to be a combination of the above suggestions and will in general depend on the system under discussion—Chapter 6 examines the effect of the electric field on the extraction of Mo and S atoms from MoS_2.

The above text is a summary of a small part of the experimental and theoretical work being carried out on the transition-metal dichalcogenides—there are many other interesting features of these materials which are not directly relevant to this thesis. For example several of the metallic TX_2s (*e.g.*, TaS_2, $NbSe_2$) exhibit Charge Density Waves (CDW) (large-wavelength correlations in the electron density) which can be imaged directly with the STM or Atomic Force Microscope (AFM) (Lieber & Wu 1991b, Lieber & Wu 1991a, Garnaes, Gould, Hansma, & Coleman 1991). It is also possible to etch the surfaces of the

Material	Bulk Bond Length (au (Å)) Calculated	Experiment
MoS_2	4.562 (2.414)	4.57 (2.42)
$MoTe_2$	5.142 (2.721)	5.12 (2.71)

Table 4.1: Comparison of calculated and experimental bond lengths for bulk MoS_2 and $MoTe_2$.

TX_2s layer-by-layer with the tip of an AFM (Delawski & Parkinson 1992), and examine the structure of liquid crystals on the surface (Hara, Iwakabe, Tochigi, Sasabe, Garito, & Yamada 1990). The transition-metal dichalcogenides, then, are versatile materials with many uses in industry and science, both pure and applied.

The rest of this chapter focuses on defect-free bulk and surfaces of MoS_2 and $MoTe_2$. Section 4.2 details PAW calculations on the bulk materials and section 4.3 reports PAW calculations to examine the atomic structure, electronic structure and STM images of the perfect surfaces.

4.2 Bulk MoS_2 and $MoTe_2$

Bulk simulations on MoS_2 and $MoTe_2$ were performed as a test to demonstrate the accuracy of the PAW method and projectors used for the later calculations. The simulations for both MoS_2 and $MoTe_2$ were performed on a single unit cell (6 atoms, 36 valence electrons), with the wavefunctions calculated at 8 k-points (Γ, M, L, and A where $e^{i\mathbf{k}.\mathbf{R}}$ for all lattice vectors $\mathbf{R}$ is real), using a plane-wave cutoff of 15Ry. Table 4.1 shows the optimised bond lengths for MoS_2 and $MoTe_2$—both are within 1% of the experimental values. No attempt was made to optimise the cell parameters; instead the values shown in Table 4.2 were used (Mattheiss 1973, Dawson & Bullet 1987) and are used in all further simulations.

	a_0 (au (Å))	c_0 (au (Å))
MoS_2	5.171 (2.736)	23.232 (12.294)
$MoTe_2$	6.650 (3.519)	26.399 (13.970)

Table 4.2: Bulk MoS_2 and $MoTe_2$ lattice parameters used in all simulations.

Figure 4.5 shows contour plots of the total charge densities of bulk MoS_2 and $MoTe_2$—the lack of (covalent) bonding between the two layers is apparent (note that Te atoms are larger than S atoms, hence the metal-chalcogen contrast changes from MoS_2 to $MoTe_2$, but the peak charges on the metal atoms are the same). The calculated direct band-gaps were 2.06eV and 2.79eV for MoS_2 and $MoTe_2$ respectively. Figure 4.6a shows the calculated band-structure of bulk MoS_2 overlaid on that of Kobayashi & Yamauchi (1995) which was obtained via a Vanderbilt pseudopotential (Vanderbilt 1985) calculation—the agreement between the two is very good. Figure 4.6b shows the calculated band-structure of bulk $MoTe_2$ overlayed on that of Dawson & Bullet (1987) calculated via an *ab-initio* (but not fully self-consistent) tight-binding method; in this case the agreement is, perhaps unsurprisingly, not as good.

4.3 The Perfect Surfaces of MoS_2 and $MoTe_2$

As mentioned in Section 2.5, simulations utilising periodic boundary conditions must make some kind of slab approximation to represent surfaces. The TX_2s are particularly well-suited to such an approximation since the inter-layer interactions (Van der Waals) are small and it is found that the qualitative features of the single-slab band structure match those of both the bulk and a four-slab approximation to the surface (Kobayashi & Yamauchi 1995). The surface simulations here were based on a 3×3 $MoS_2/MoTe_2$ single-layer supercell (27 atoms, 162 valence electrons) with a c dimension roughly equal to

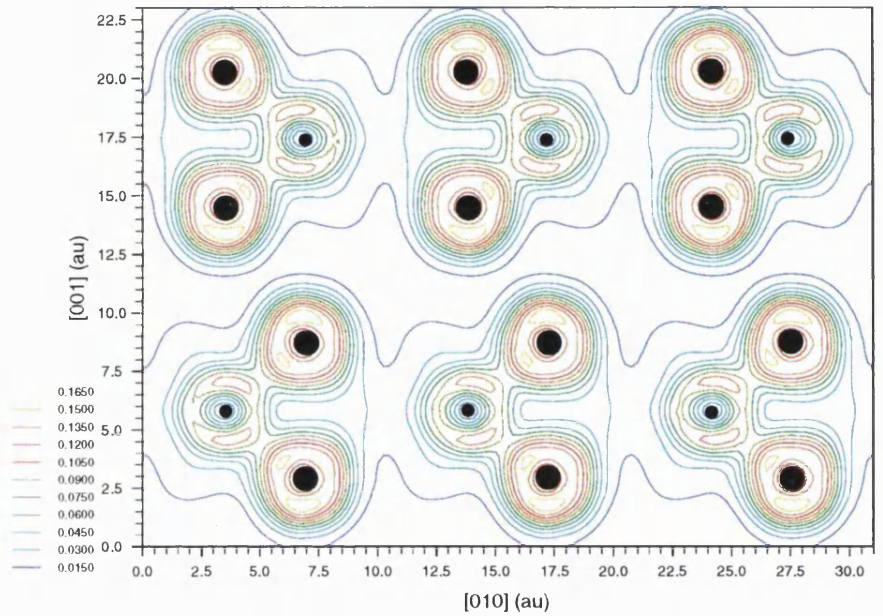

a)

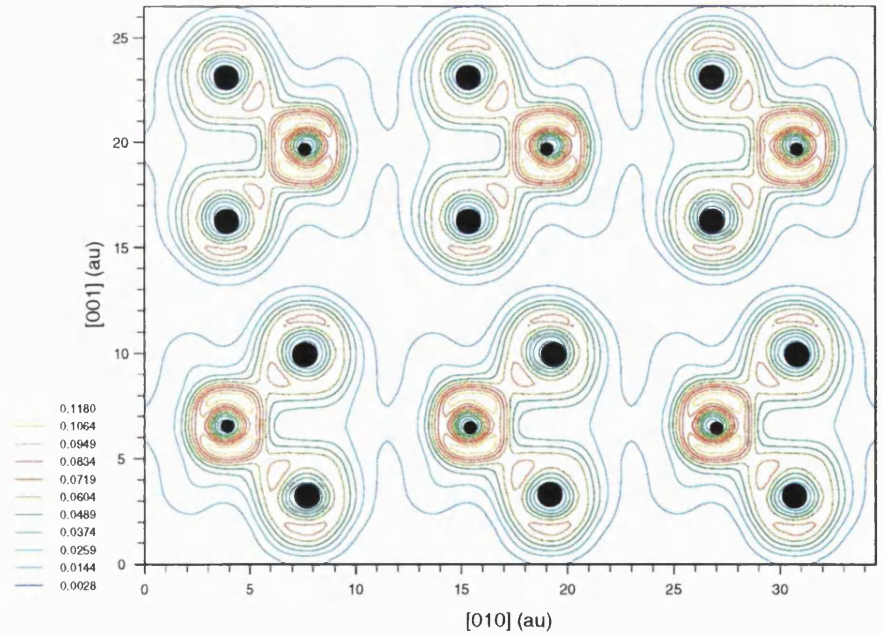

b)

Figure 4.5: Contour plots of the total charge densities of bulk a) MoS_2 and b) $MoTe_2$ calculated via the PAW technique. The slice is in the $(\bar{2}10)$ plane through the atom centres.

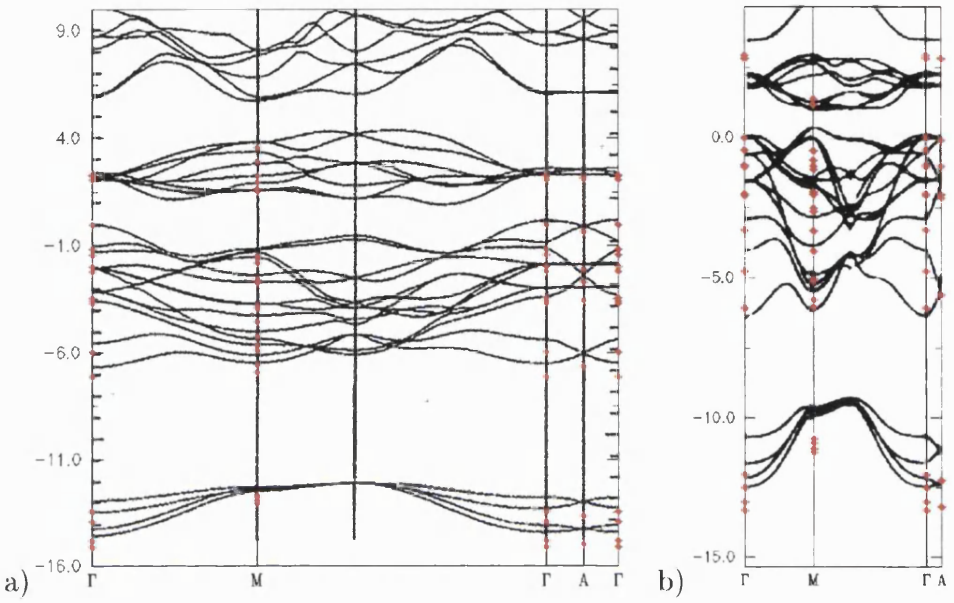

Figure 4.6: Band-structures of bulk a) MoS_2 and b) $MoTe_2$ as calculated by the PAW method. The PAW calculated points are represented by closed circles and are overlayed on those calculated by a) a similar plane-wave calculations (Kobayashi & Yamauchi 1995) and b) a tight-binding calculation (Dawson & Bullet 1987) (See main text).

that of the bulk cell. As with the bulk calculations, planewave cutoffs of 15Ry were used (tested for convergence to 25Ry). Figure 4.7 shows the simulation cell and Figure 4.8 shows the full surface Brillouin Zone, marking the points which are sampled by the reduced Brillouin Zone.

Upon relaxation, the metal–chalcogen bond lengths (initially set to their bulk values) changed to 4.539au for MoS_2 and 5.131au for $MoTe_2$–a change of less than half a percent from the bulk calculated values. The S–Mo and Te–Mo plane separations were 2.922au (1.546Å) and 3.404au (1.801Å) respectively. This is further confirmation that the inter-layer interactions are small in the bulk material and lends credibility to the single-slab approximation.

Figure 4.9 shows the total charge densities of the MoS_2 and $MoTe_2$ surfaces. Figure 4.10 shows the Tersoff-Hamann (Equation (3.6)) constant-height STM

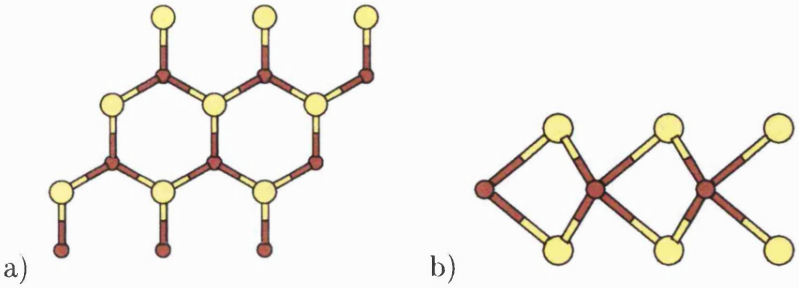

Figure 4.7: The 3×3 single-slab cell used to approximate the perfect MoS_2 and $MoTe_2$ surfaces in the calculations. a) viewed from above the *ab* plane, and b) the side view. The *c* dimension of the cell is roughly equal to that of the bulk lattice.

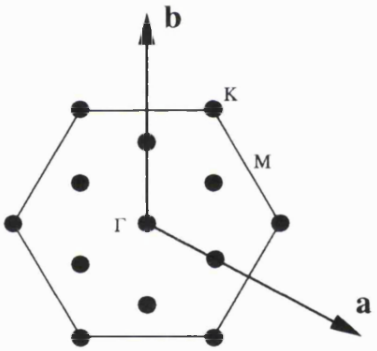

Figure 4.8: Full surface Brillouin Zone. The dots mark the points sampled using a 3×3 unit-cell simulation (Γ points of the reduced Brillouin Zone).

images of the two surfaces. Apart from the different cell dimensions, the two images are almost identical, with the peaks occurring above the surface chalcogen atoms as expected (Kobayashi & Yamauchi 1995, Altibelli et al. 1996). However, it should be noted that calculations on MoS_2 by Altibelli et al. (1996), where the STM tip is included explicitly in the image calculation, show that at tip–sample separations less than ~ 4.2Å the brightest point on the image does not appear at either the Mo or the S site. In this case, the image appears similar to that expected (*i.e.*, a hexagonal array of peaks) but the peaks occur somewhere between the Mo and S surface-projected sites. Figure 4.11 shows

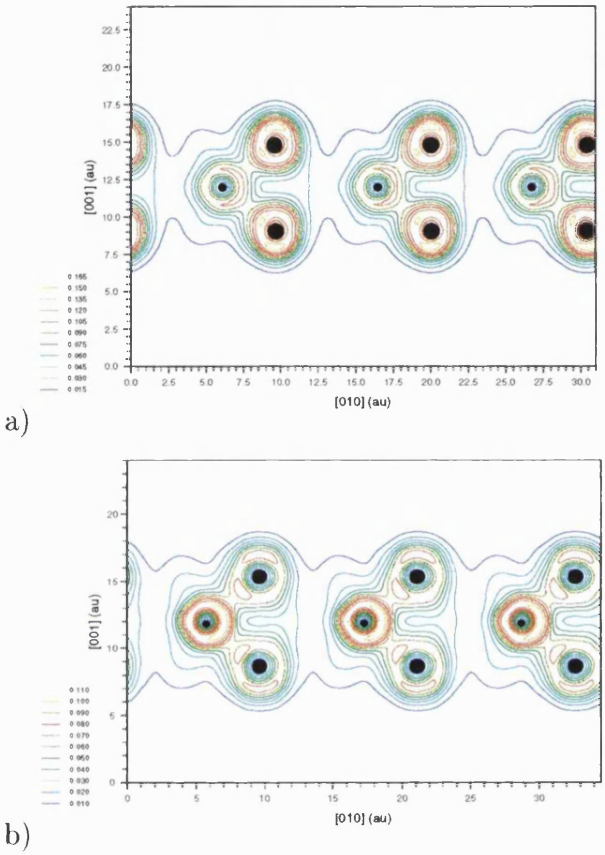

Figure 4.9: Total charge density of the single-slab surfaces of a) MoS_2 and b) $MoTe_2$ taken through the $(\bar{2}10)$ plane.

calculated constant-height scan-lines along the [010] direction for a series of tip heights. No significant separation dependence, other than in the corrugation, can be seen in the STM images—the image obtained, according to Altibelli et al. (1996), is that for the larger (*i.e.*, experimental) tip–sample separations. The electronic-structure calculations presented here have a better description of the wavefunctions than Altibelli et al., but the image calculations use perturbation theory and do not include the tip, hence the change in image is probably an effect due to the tip.

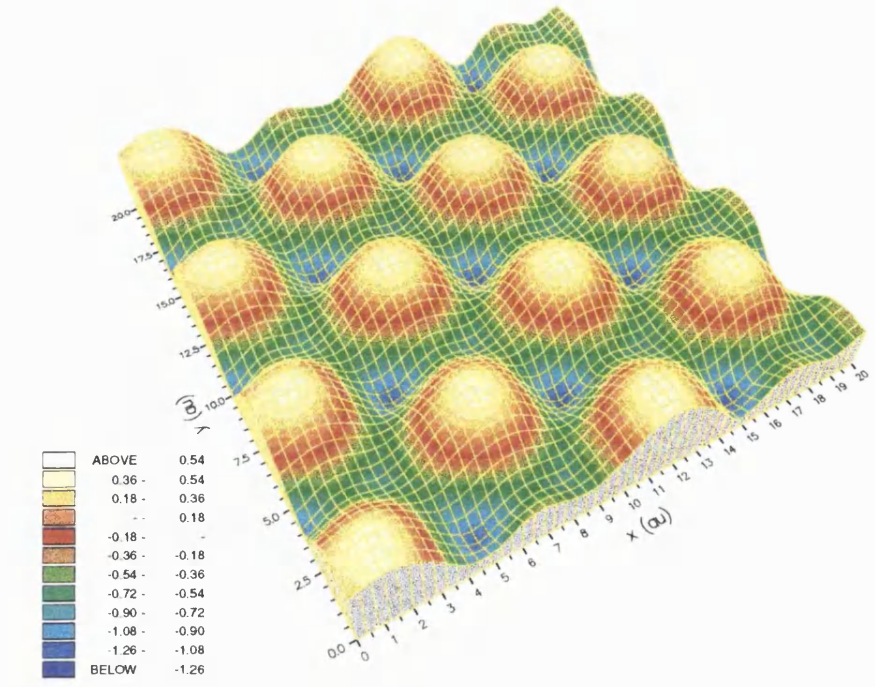

a)

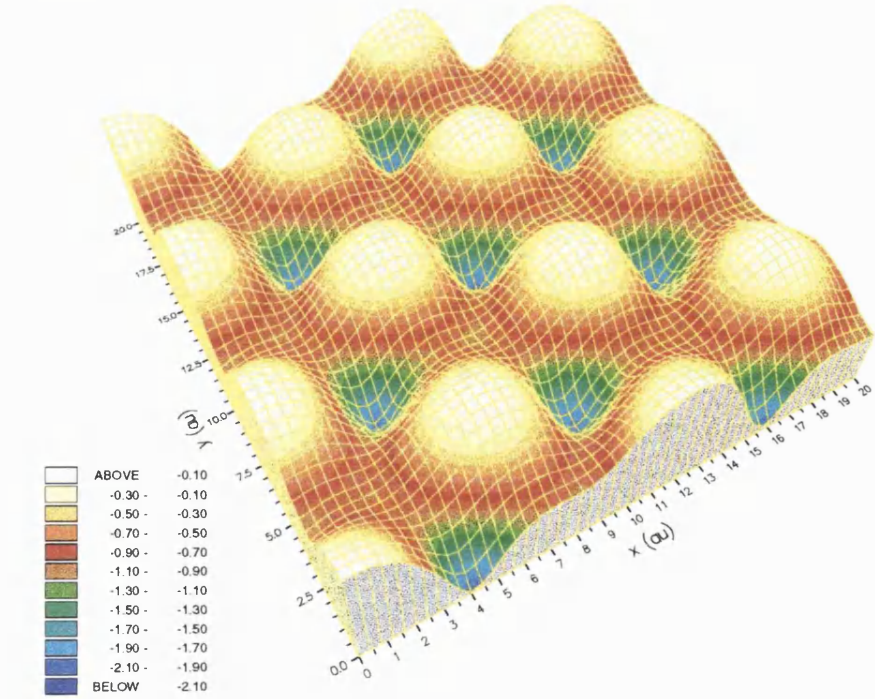

b)

Figure 4.10: Calculated (Tersoff–Hamann) filled-state STM images of the a) MoS_2 and b) $MoTe_2$ surfaces for a simulated applied bias of 0.8V. The peaks in the images occur over the surface chalcogen atoms as expected; the zeros on the height scale correspond to 6.0au and 8.0au above the Mo planes respectively.

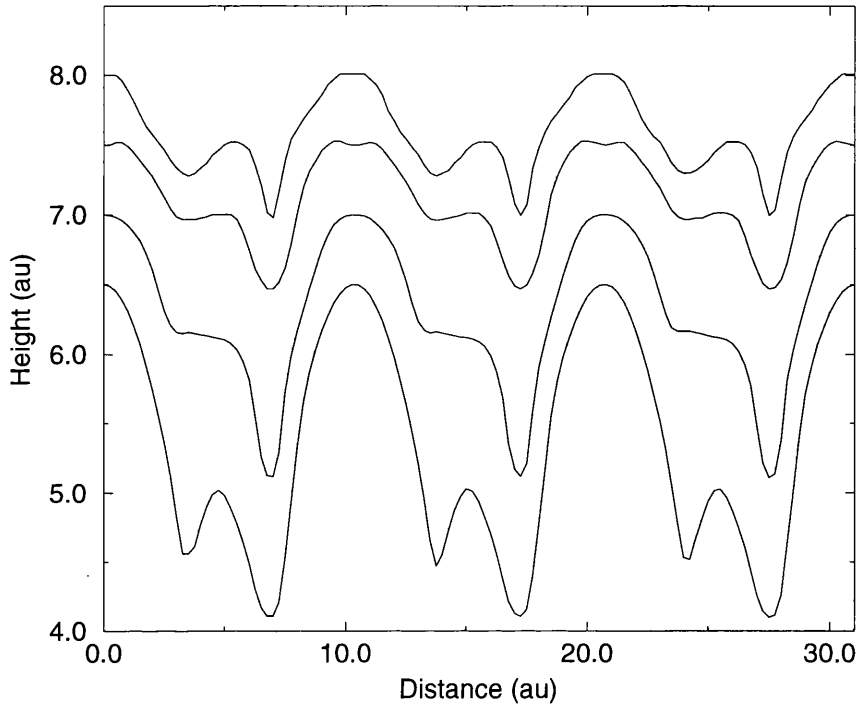

a)

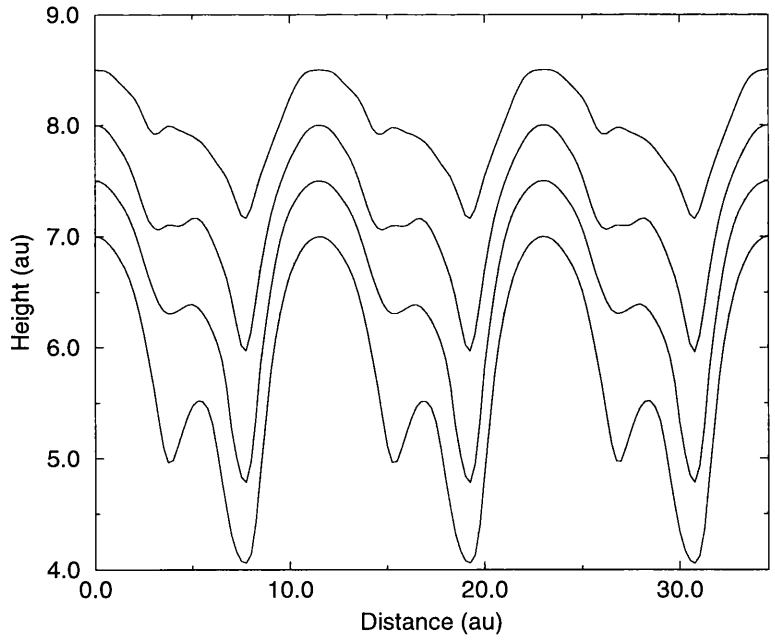

b)

Figure 4.11: Calculated (Tersoff–Hamann) filled-state STM scan-lines of perfect a) MoS_2 and b) $MoTe_2$ surfaces for a simulated applied bias of 0.8V at various tip–sample separations. The peaks in the images occur over the surface chalcogen atoms as expected. The scan-lines are along the [010] direction, and the heights are relative to the metal plane.

4.4 Conclusions

This chapter reported PAW simulations of the bulk and perfect surfaces of MoS_2 and $MoTe_2$. The bulk material simulations included one unit cell and 8 k-points (Γ, M, L, and A) with wavefunctions up to 15Ry. The bulk material bond-lengths (Table 4.1) were found to match experiment to within 1% and there was good agreement between the band-structures calculated here and those of other groups (Figure 4.6).

Perfect surfaces were simulated using 3×3 single-slab supercells in boxes with c dimensions equal to the bulk cells. This effectively doubles the separation between slabs and is sufficient to remove any surface–surface interactions and provide room for the extraction of Tersoff–Hamann STM images. Planewaves up to 15Ry were used to represent the wavefunctions. The bond-lengths were found to change by less than half a percent from the calculated bulk values. The Tersoff–Hamann STM images of the surfaces (Figure 4.10) showed a series of circular peaks situated over the chalcogen atoms as expected, with no appreciable tip–sample separation dependence (Figure 4.11).

Chapter 5

Electronic Structure and STM Images of Vacancy Defects on the MoS_2 and $MoTe_2$ Surfaces

5.1 Introduction

The introduction to Chapter 4 also forms a general introduction to this chapter. This chapter is concerned with the nature of the defects observed on the transition-metal dichalcogenides such as the monatomic-hole and trimer defects observed by Fuchs et al. (1992, 1993) on WSe_2 (see Figure 4.3). Single-atom, neutral chalcogen and metal vacancy defects on MoS_2 and $MoTe_2$ are studied using the PAW method. Section 5.2 covers the chalcogen vacancy calculations, Section 5.3 covers the metal vacancy calculations and Section 5.4 summarises the chapter.

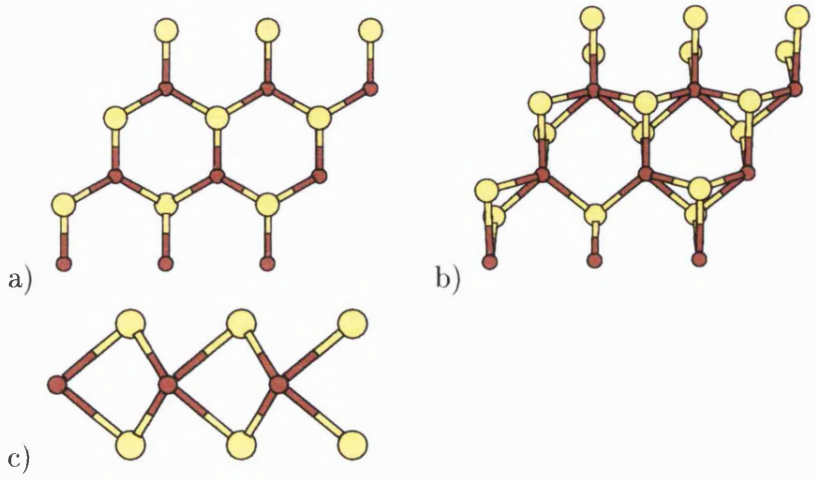

Figure 5.1: Unit cell geometry in the chalcogen vacancy simulations; a single chalcogen (S or Te) was removed from the 3×3 single-slab unit cell of MoS_2 and $MoTe_2$. a) viewed from above the *ab* plane, b) a perspective view, and c) side view.

5.2 Chalcogen Vacancies on MoS_2 and $MoTe_2$

A chalcogen vacancy defect was simulated by removing a chalcogen atom along with its 6 valence electrons from the top layer (*i.e.*, the side on which the STM images are taken) of the 3×3 surface supercell described in Section 4.3. Figure 5.1 shows the unit cell used. Plane waves up to a cutoff of 15 Ry were used to describe the pseudo–wavefunctions.

Table 5.1 shows the magnitude of the relaxations of the atoms nearest the defect for the Γ-point calculation. Starting from the relaxed atomic coordinates, the MoS_2 electronic structure was recalculated with four k-points (Γ and M) and it was found that the forces in the Γ-point calculation were converged to within 0.008au (0.4eVÅ^{-1}). The relaxation about the defect is much larger in $MoTe_2$ than in MoS_2 (which barely changes from the perfect structure), but in both cases the C_{3v} symmetry about the defect is maintained with the majority of the relaxation occurring in the *ab*-plane. Creation of the vacancy defect, and the associated removal of bonding electrons, causes lo-

Material	Nearest neighbour metal atom displacement (Å)	Nearest neighbour chalcogen atom displacement (Å)
MoS_2	0.003	0.003
$MoTe_2$	0.301	0.090

Table 5.1: Magnitude of the atomic displacements in the chalcogen vacancy systems for the nearest neighbour Mo and chalcogen atoms. The distortions are almost entirely within the *ab*-plane.

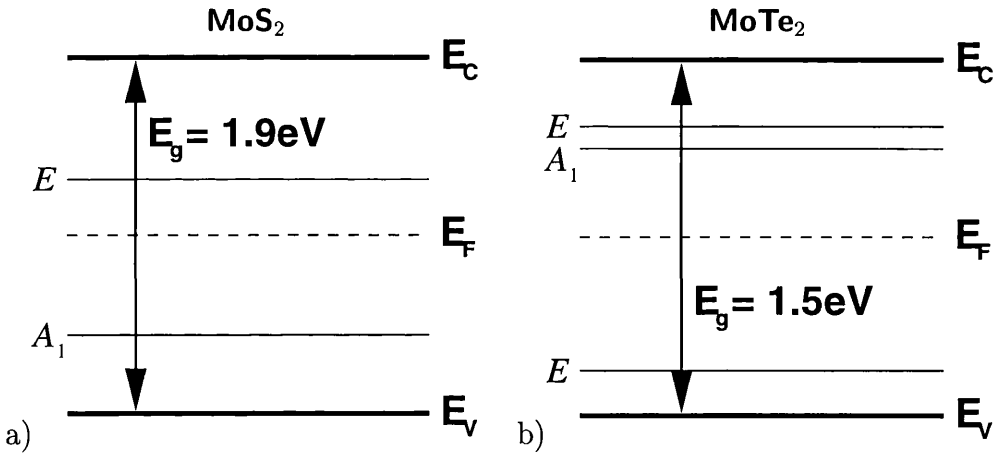

Figure 5.2: Gap-state eigenvalues and state-symmetries for chalcogen vacancies on a) MoS_2 and b) $MoTe_2$ surfaces. E states are doubly degenerate and A states are non-degenerate.

calised electronic states to appear in the perfect-surface forbidden-energy gap. Figure 5.2 shows the gap-state eigenvalues and degeneracies, and Figure 5.3 shows the charge-density isosurfaces for the filled and empty gap-states. The symmetry of the eigenstates was obtained by examining how the overlaps of the eigenfunctions with the PAW projector functions transform under the operations of the C_{3v} point-symmetry group. Figure 5.4 shows slices through the total and gap-state charges in the $(\bar{2}10)$ plane for the two systems. The empty gap-states are similar for both MoS_2 and $MoTe_2$ (Figures 5.3b and 5.3d

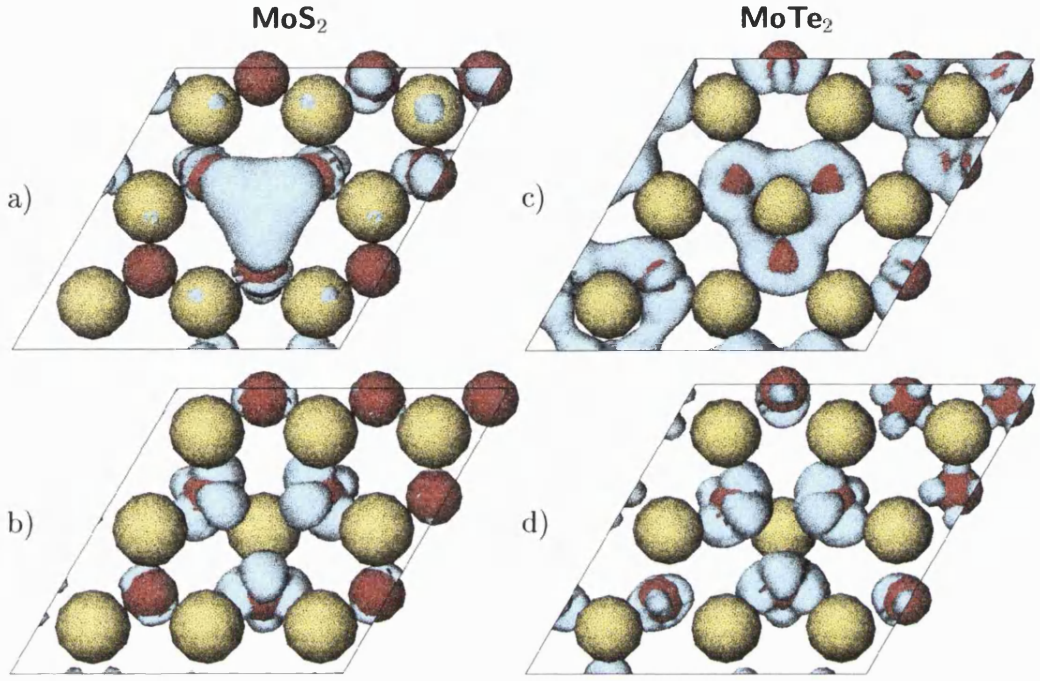

Figure 5.3: Charge-density isosurfaces for the filled and empty gap-states of MoS_2 and $MoTe_2$ with a chalcogen vacancy in the top chalcogen layer at the centre of the cell. a) MoS_2 filled gap-states (0.003au); b) MoS_2 empty gap-states (0.006au); c) $MoTe_2$ filled-gap states (0.003au); d) $MoTe_2$ empty-gap-states (0.006au). The red and yellow spheres represent the metal and chalcogen atoms respectively. The numbers in brackets represent the charge per unit volume at which the contours were evaluated.

respectively), being largely associated with the *d* orbitals of the metal atoms adjacent to the defect. The difference occurs in the filled gap-states where for MoS_2 (Figure 5.3a) the electrons are localised between the planes of the Mo and S atoms, directly below the vacancy. For $MoTe_2$ (Figure 5.3b) on the other hand, the charge is more diffuse, existing in the plane of the Mo atoms, concentrating in a ring encompassing the Mo atoms nearest the vacancy.

Figure 5.5 shows the calculated filled-state STM images and, although they are very similar (consisting unsurprisingly of peaks above the chalcogen atoms and a pit above the vacancy), it is possible to see a small bump in the central pit on the MoS_2 image which does not occur on $MoTe_2$. This feature is

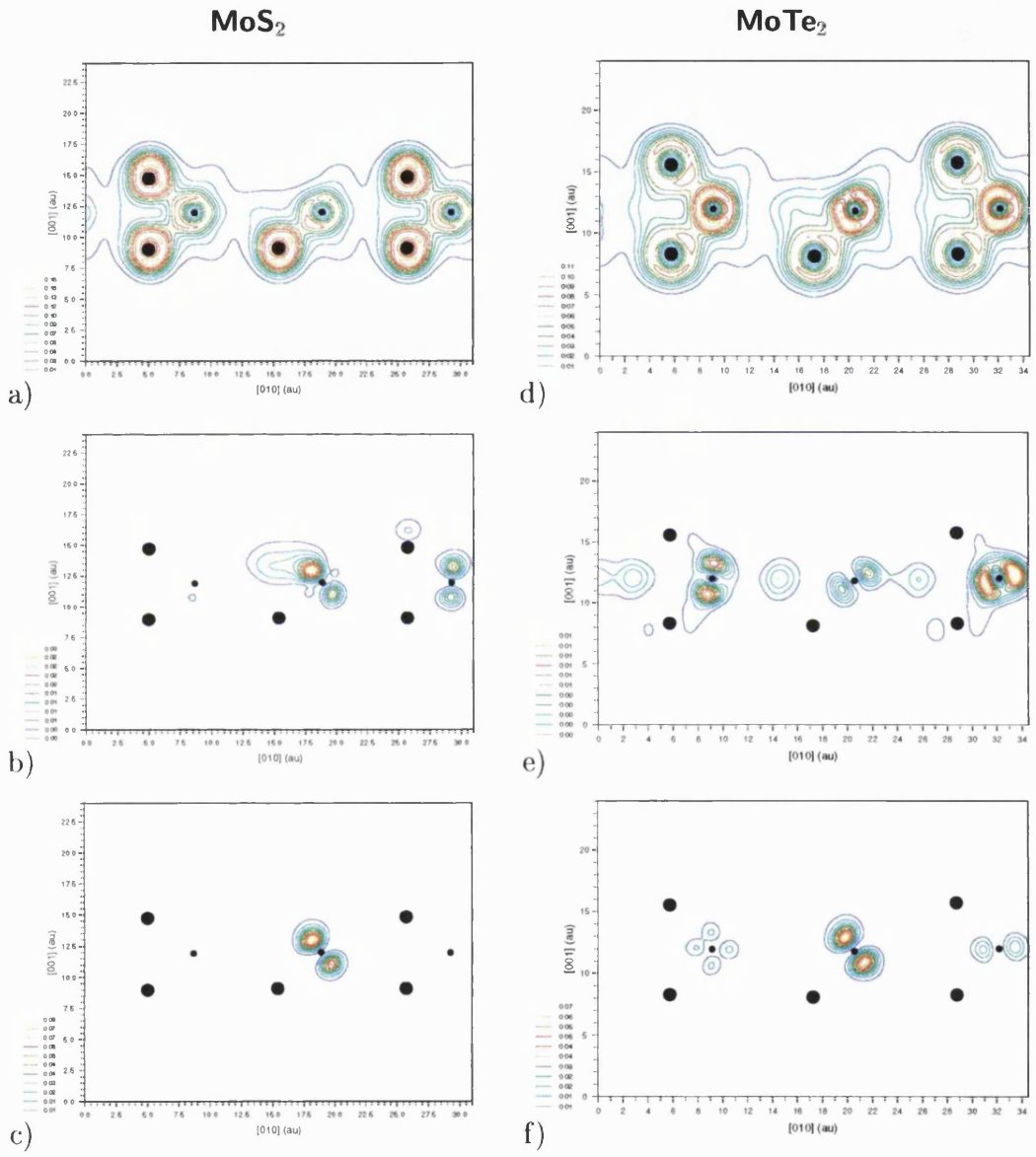

Figure 5.4: Charge density contours of (left) MoS_2 and (right) $MoTe_2$ with chalcogen vacancies. Shown are (top) total charge; (middle) filled gap-state charge; and (bottom) empty gap-state charge. The slice is taken in the $(\bar{2}10)$ plane through the vacancy defects (centre of the image).

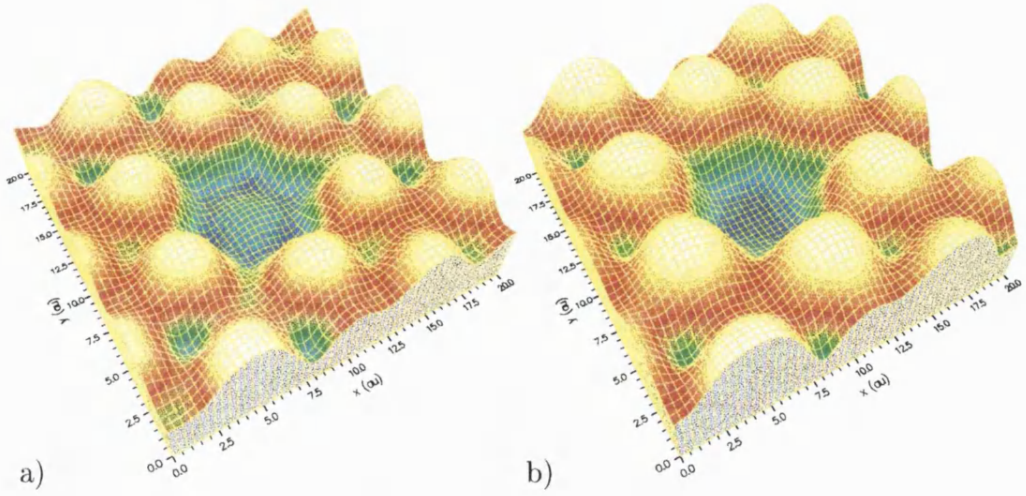

Figure 5.5: Calculated filled-state STM images for a) MoS_2 and b) $MoTe_2$ with chalcogen vacancies located at the centre of the images. There is a slight bump in the central pit of the MoS_2 image which does not appear in the $MoTe_2$ image, due to the structure of the filled gap-state charge density (Figures 5.3a and 5.3c) which is physically closer to the tip in MoS_2. The tip height varies from 4.5au to 6.9au for MoS_2 and 4.3au to 7.4 au for $MoTe_2$ (relative to Mo plane).

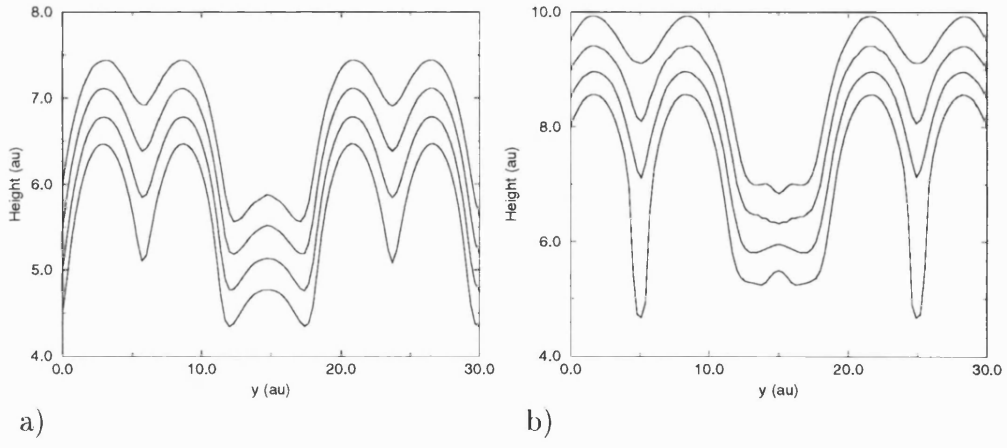

Figure 5.6: Constant-current filled-state scan-lines at various tip–sample separations of MoS_2 and $MoTe_2$ with chalcogen vacancies. The scan-lines are taken in the [010] direction across the vacancy site.

seen more easily in the constant-height scan-lines shown in Figure 5.6 and the difference can be attributed to the difference in the filled gap-states between the two systems. The STM images shown here are similar to those obtained by Whangbo et al. (1995) for MoS_2 with a sulphur vacancy. Furthermore, STM experiments carried out by Fuchs et al. have observed defects on WSe_2 (shown in Figure 4.3a), and more recently on MoS_2 (Fuchs 1996), which also look similar to those in Figure 5.5—it seems likely that these defects are due to missing surface Se/S atoms.

5.3 Metal Vacancies on MoS_2 and $MoTe_2$

Section 5.2 showed that both MoS_2 and $MoTe_2$ behaved in the same manner with the creation of a chalcogen defect. This is perhaps not surprising given that all VIB TX_2s have similar physical and chemical properties. However, the simulations relating to metal vacancies in the same systems which are covered in this section behave in fundamentally different ways: the metal vacancy in $MoTe_2$ is discovered to be a Jahn–Teller system and as such, the lattice distorts in a symmetry-reducing manner. This section is split into two subsections, the first (Section 5.3.1) covering the metal vacancy simulations on MoS_2, and the second (Section 5.3.2) covering the metal vacancies on $MoTe_2$. Appendix B covering the Jahn–Teller effect and the D_{3h} symmetry group is relevant to the latter section.

5.3.1 Metal Vacancies on MoS_2

The metal vacancy on MoS_2 was simulated by the same 3×3 surface super-cell used previously, with a single Mo atom (including valence electrons) removed to generate the vacancy. Figure 5.7 shows the simulation cell in its initial configuration. A 15Ry planewave cutoff was used for the electronic wavefunctions and only the Γ point of the reciprocal cell was considered. Again, the

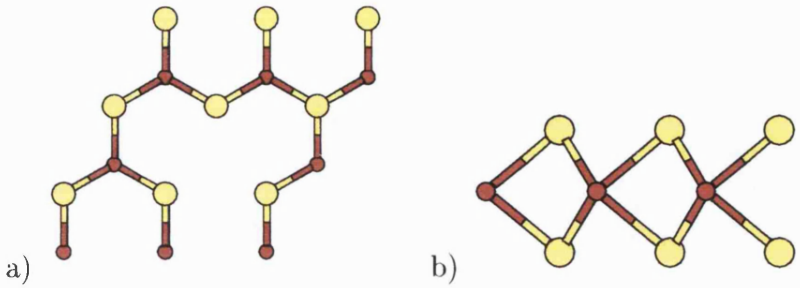

Figure 5.7: Simulation cell used for the MoS_2, Mo-vacancy system shown from a) above the *ab*-plane and b) the side. The surface is represented by a 3×3 single-slab cell, with the vacancy created by removing a single Mo atom and its associated electrons.

atomic relaxation around the vacancy was minimal with the sulphur atoms adjacent to the vacancy moving 0.014Å in the *ab*-plane and a slight relaxation in the *c* direction. The relaxation maintains the D_{3h} point-symmetry about the vacancy.

Five gap-states are apparent in this case: a doubly-degenerate state below the Fermi level, and a singly- and a doubly-degenerate state above the Fermi level. Figure 5.8 shows the eigenvalues, degeneracies, and charge-density iso-surfaces for the filled and empty gap states. Figure 5.9 shows slices through the total and gap-state charges. The filled gap-state charge is largely associated with the dangling *p*-orbitals on the sulphur atoms adjacent to the vacancy, and the empty gap-state charge is localised around the nearest-neighbour metal atoms.

Figure 5.10 shows the calculated STM image and scan-lines for a simulated applied bias of 0.8V. The metal vacancy is located below the centre of the 3D 'topographic' image and the trimer of brighter peaks is associated with the sulphur atoms nearest the Molybdenum vacancy (the second-nearest-neighbour sulphurs also appear slightly brighter). The scan-lines are shown for various tip–sample separations through the vacancy site and an adjacent sulphur pair.

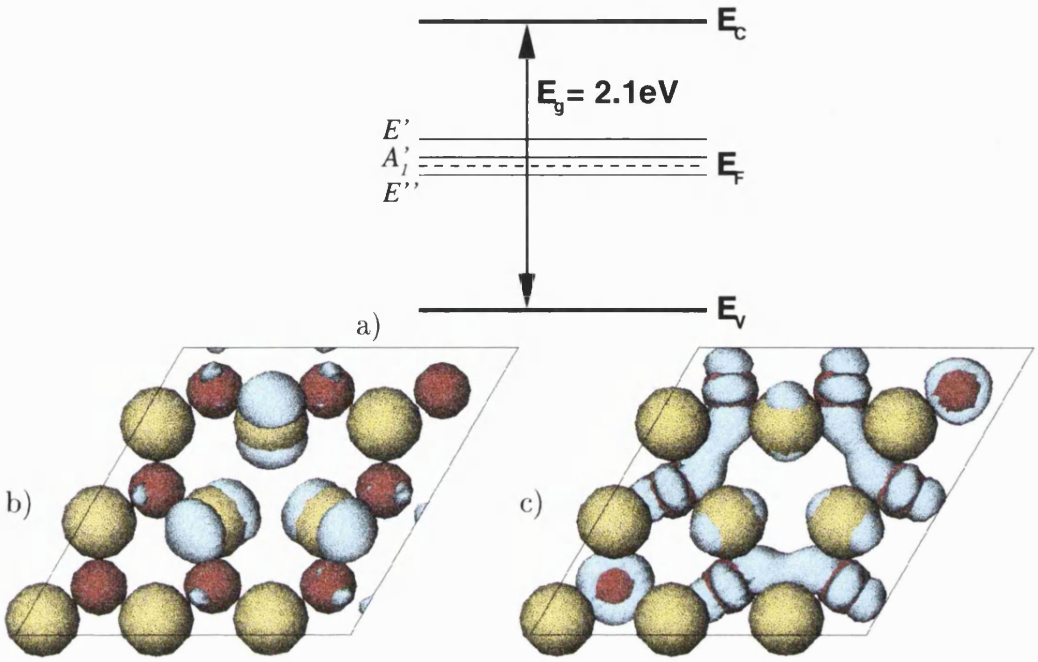

Figure 5.8: a) Gap state eigenvalues and degeneracies, b) filled gap-state charge-density isosurface (0.0036au), and c) empty gap-state charge-density isosurface (0.0054au) for MoS_2 with a Mo vacancy located at the the centre of the cell. The red and yellow spheres represent the Mo and S atoms respectively. Numbers in parentheses give the charge per unit volume at which the surfaces were evaluated.

The increase in apparent height of the nearest-neighbour sulphur atoms is a result of the dangling-bond *p*-states (Figure 5.8b) which locally increase the electronic DoS near the Fermi level. The STM image of Figure 5.10a is qualitatively the same as that obtained by Magonov & Whangbo (1994) on the same system (but see Section 5.4) and also shares the same trimer-like feature seen in the experimental image of Fuchs et al. (1992) for a defect created on WSe_2 (see Figure 4.3b). The trimer defects observed by Fuchs are asymmetric where the predicted images for MoS_2 are not. There are a couple of possible explanations for the asymmetry in the experimental WSe_2 STM images. For example, there may be some kind of symmetry lowering distortion of the surface as a result of the existence of the vacancy (as we find

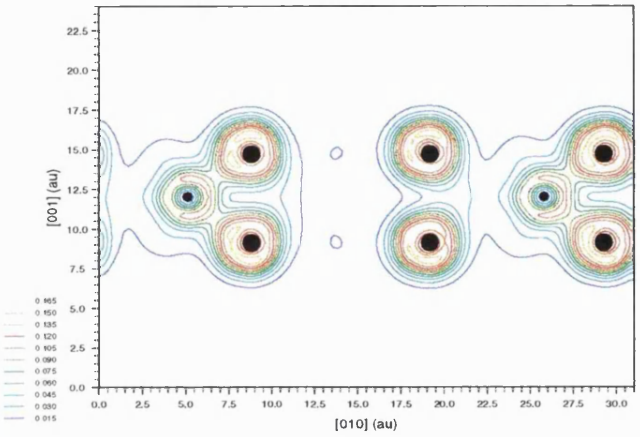

a)

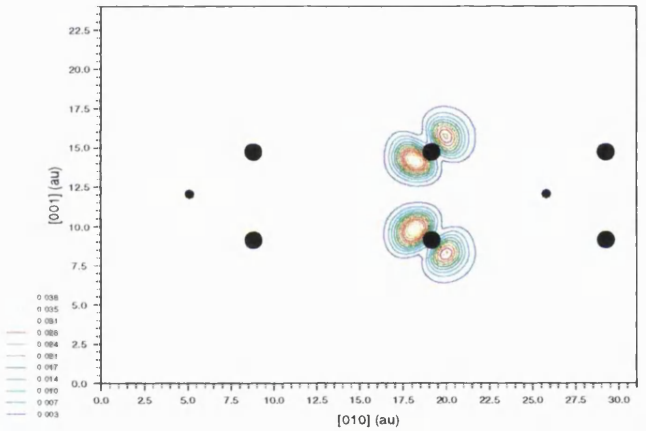

b)

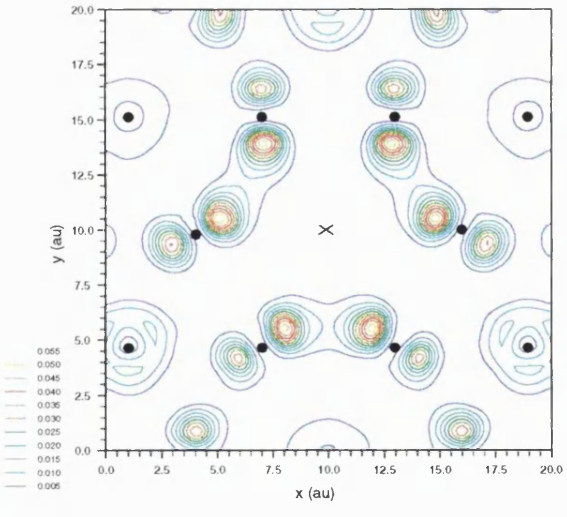

c)

Figure 5.9: Charge density contours of MoS_2 with a metal vacancy. Shown are a) total charge, b) filled gap-state charge, and c) empty gap-state charge. For a) and b) the slice is taken through the $(\bar{2}10)$ plane through the vacancy defects (centre of the image); c) is taken in the Mo plane (the cross marks the vacancy).

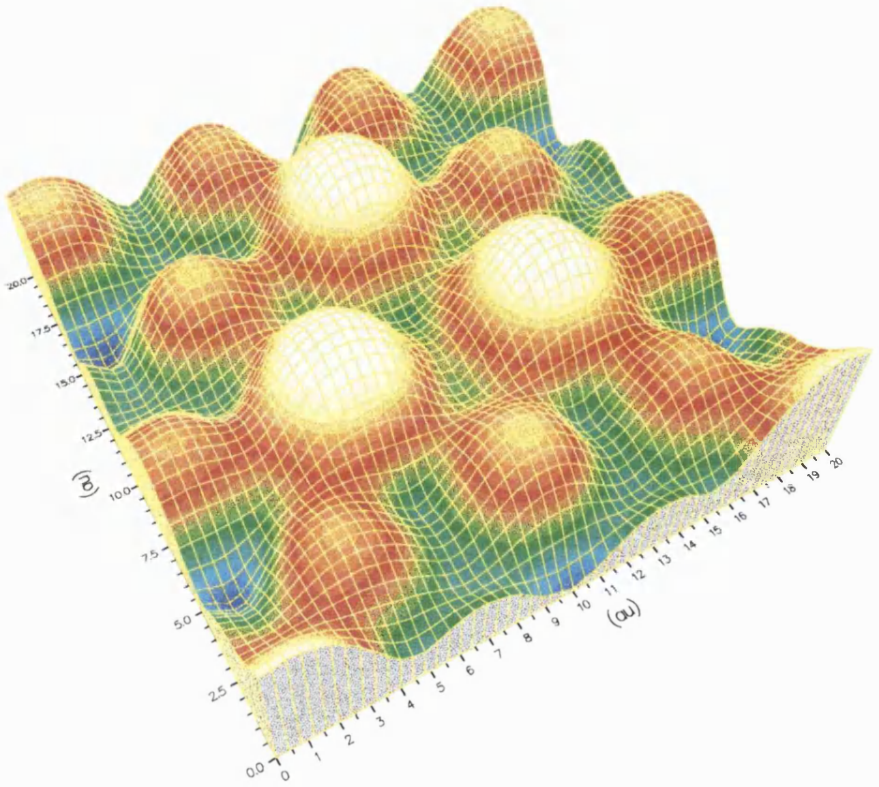

a)

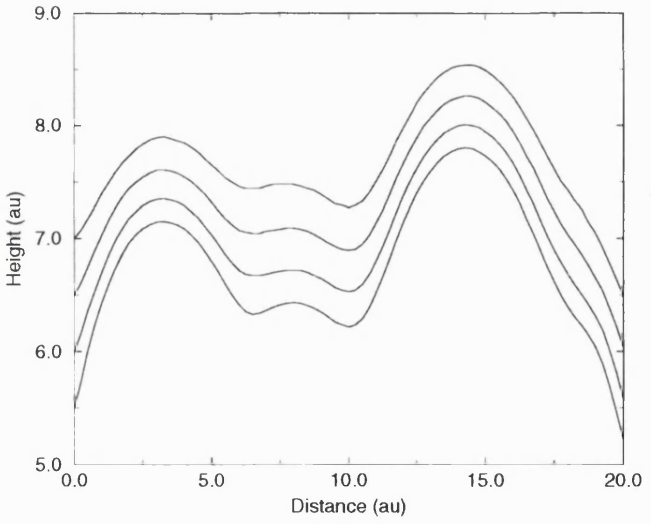

b)

Figure 5.10: a) Calculated STM image and b) STM scan-lines for MoS_2 with a sub-surface metal vacancy for a simulated tip-positive bias of 0.8V. The vacancy is located below the centre of the trimer-peak structure shown in the 3D image. The trimer structure can be attributed to the dangling p-orbitals located on the sulphur atoms nearest the vacancy. The scan-lines are taken across the vacancy site at $x = 10$au along the y direction. The uppermost scan-line corresponds to the 2D topograph in (a).

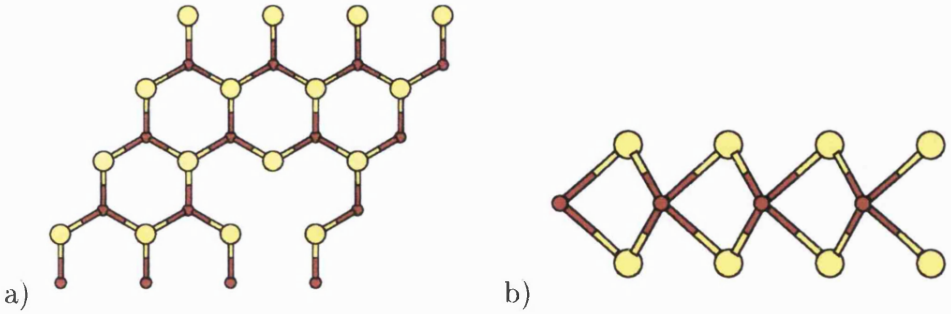

Figure 5.11: Simulation cell used for the $MoTe_2$, Mo-vacancy calculations viewed along a) the c-axis, and b) the a-axis. Here, the surface is represented by a 4×4 single-slab cell with the vacancy created by removing a single Mo atom and its associated electrons.

for $MoTe_2$—see Section 5.3.2), although this is unlikely as all three defects shown appear to be oriented in the same direction. A more likely explanation is that the asymmetry is an artifact of the tip. It seems likely that the trimer-like WSe_2 defects are due to sub-surface tungsten vacancies.

5.3.2 Metal Vacancies on $MoTe_2$

Initially, for the $MoTe_2$ system with a metal vacancy, a 3×3 single-slab cell was used as for all other calculations so far. However, the lattice distortions observed with this system turned out to be much larger than expected (for reasons discussed below) and as a result the cell was extended to the 4×4 single-slab cell shown in Figure 5.11.

Figure 5.12 shows the relaxed atomic structure overlaid on a shadow of the undistorted cell (*i.e.*, before the atoms were allowed to move); the D_{3h} symmetry of the non-relaxed structure was reduced to C_2 upon relaxation. The largest displacements from the perfect surface positions occur for the atoms nearest the vacancy: the nearest-neighbour Mo atoms are displaced by 0.31Å, and the nearest-neighbour Te atoms move 0.22 to 0.25Å depending on their position relative to the C_2 axis. However, unlike the other simulations

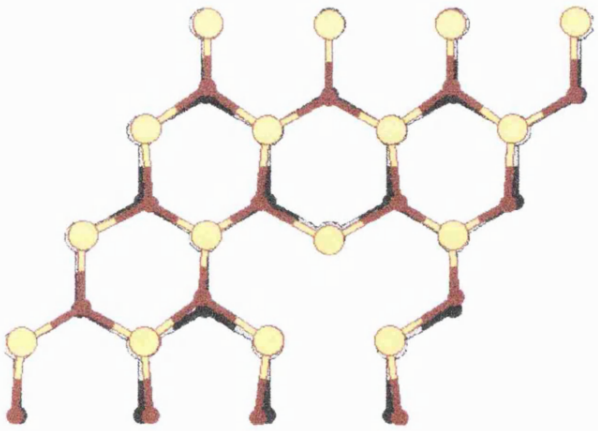

Figure 5.12: Atomic structure of $MoTe_2$ with a metal vacancy before and after atomic relaxation. The foreground (colour) image shows the relaxed, distorted structure, and is overlaid on a 'shadow' of the undistorted (*i.e.*, perfect surface) structure. The D_{3h} symmetry of the undistorted system is reduced to C_2 upon relaxation.

described in this paper, the relaxation extends beyond the vacancy's nearest neighbours, with the second-nearest-neighbour Mo and Te atoms moving by 0.20Å and 0.18Å respectively.

The reason for this symmetry-breaking distortion becomes apparent upon examination of the electronic structure of the non-relaxed system. It is found that the lowest-energy electronic configuration in the case where the ions are fixed in their perfect surface positions is one in which the two highest occupied eigenstates are equally (*i.e.*, singly) occupied. Figure 5.13 shows a schematic diagram (to scale) of the eigenvalues and degeneracies before and after atomic relaxation; before relaxation the A_1' state is below the E'' state (*cf.* Figure 5.8a, where this situation is reversed) leaving a pair of singly occupied degenerate states at the Fermi level, making this a Jahn–Teller system.

Examination of a table showing how the irreducible representations of the D_{3h} group behave on reduction of symmetry (displayed in Appendix B) shows that the E'' state remains doubly degenerate until the symmetry is reduced to at least C_{2v}. Table 5.2 shows the magnitudes per atomic site of the symmetry

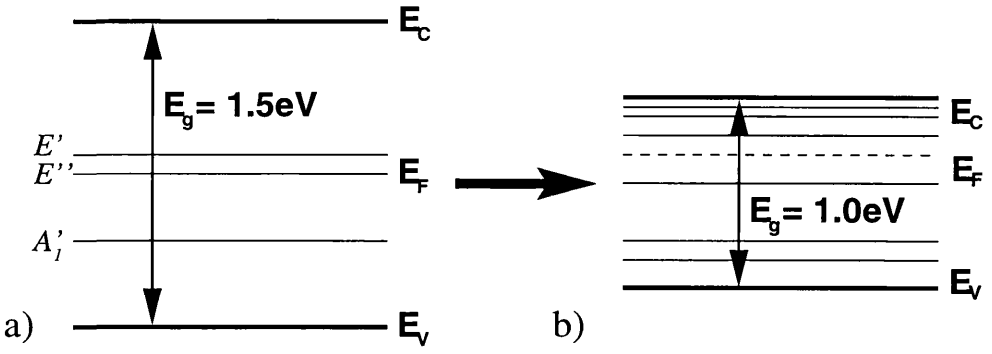

Figure 5.13: Gap-state eigenvalues for $MoTe_2$ with Mo vacancy: a) with atoms in their perfect surface positions, and b) after atomic relaxation. There is an orbital degeneracy at the Fermi level in the non-relaxed system which leads to a Jahn–Teller distortion upon relaxation. The reduction of the band gap on relaxation is attributed to finite-size effects.

Atoms	A_1'	A_2'	E'	A_1''	A_2''	E''
NN Mo	0.184	0.001	0.195	0.002	0.000	0.010
NN Te	0.231	0.000	0.049	0.000	0.000	0.009
2NN Te	0.108	0.000	0.114	0.002	0.000	0.010

Table 5.2: The average magnitude per atomic site of the projected distortions (Equation 5.1) in angströms for each of the D_{3h} representations. The A_1' and E' representations account for most of the total lattice relaxation (see also Figure 5.14). NN and 2NN denote the first- and second-nearest neighbours respectively.

projected distortions for each of the six irreducible representations ν of the group D_{3h}. This is defined by

$$d^{(\nu)} = \frac{1}{n_a} \sum_{i}^{n_a} |\mathbf{R}_i^{(\nu)}| \tag{5.1}$$

where n_a is the number of sites in the shell under study (nearest neighbour etc.), and $\mathbf{R}_i^{(\nu)}$ is the symmetry projected distortion for representation ν at

site i:

$$\mathbf{R}_i^{(\nu)} = \mathbf{P}^{(\nu)}\mathbf{R}_i = \left[\frac{n_\nu}{g}\sum_{A \text{ in } \mathcal{G}} \chi^{(\nu)}(\mathbf{A})\mathbf{A}\right]\mathbf{R}_i \tag{5.2}$$

where n_ν is the dimension of representation ν in group $\mathcal{G}$, g is the order of $\mathcal{G}$, $\chi^{(\nu)}(\mathbf{A})$ is the character of the operator $\mathbf{A}$ in representation ν, and $\mathbf{R}_i$ is a column vector of all the displacements of the atoms in the shell in question.

This shows that the distortion of the lattice is largely due to two modes: one which transforms like the identity representation A_1', and therefore does not affect the point-group symmetry (Figure 5.14a) and one which transforms according to the E' representation (Figure 5.14b). There is also a small contribution from the E'' representation (Figure 5.14c), without which the symmetry would have been C_{2v} as opposed to C_2, but this is more than an order of magnitude smaller than the A_1' and E' contributions .

Figure 5.15 shows the filled and empty gap-state charge densities for the system before and after atomic relaxation (the labelling of states as 'gap-states' here is not precise, owing to the small separation between the band-edge and the gap-states, and is based purely on their physical localisation). Figure 5.16 shows the total and gap-state charge densities in a slice through the vacancy site along the C_2 rotation axis. Comparing the gap-states of $MoTe_2$ (Figures 5.15 and 5.16) with those of MoS_2 (Figures 5.8 and 5.9) we see that they have a similar makeup in terms of atomic orbitals, but that the Jahn–Teller distortion of the $MoTe_2$ system results in a lowering of the electronic symmetry to C_2 and an exchange of the filled and empty gap states, *i.e.*, the p states associated with the chalcogens are now above the Fermi level, whereas the states localised around the metal are below E_F.

Figure 5.17 shows the calculated STM image and selected scan-lines for a simulated tip-positive bias of 0.8V. In this case, because of the different ordering of the gap-states, the sulphur-localised p-orbitals do not contribute to the image for sample-negative biases (*i.e.*, imaging of filled states). In fact, the

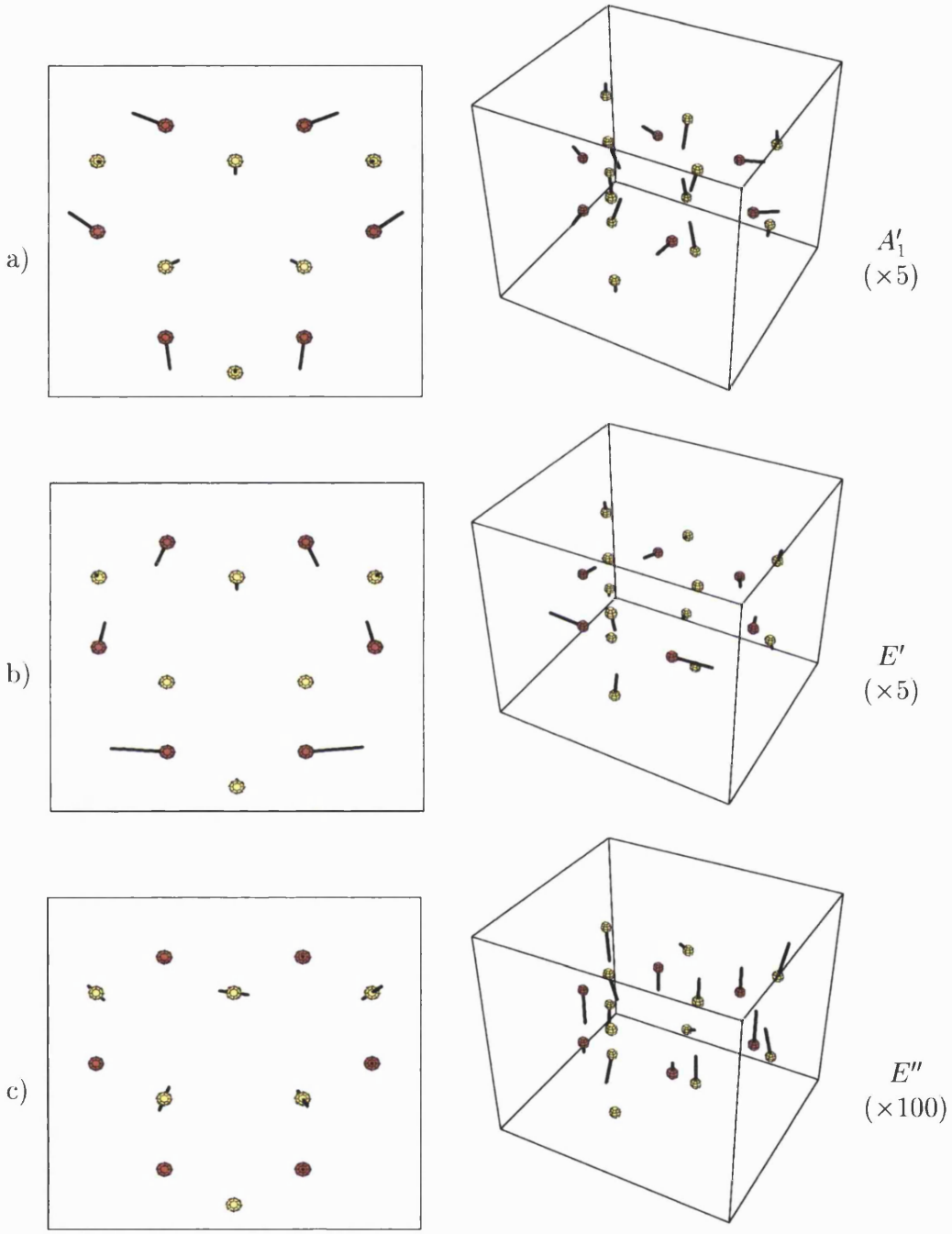

Figure 5.14: The symmetry projected distortions (Equation (5.2)) for $MoTe_2$ with a Mo vacancy (centre of the box). The lines represent the direction and magnitude of the motion for a) the A_1', b) the E' (both scaled ×5), and c) the E'' (scaled ×100) components for the nearest neighbour Mo atoms (red) and the first- and second-nearest-neighbour Te atoms (yellow). No other components show up on this scale (see Table 5.2). The 2D images are viewed from above the *ab*-plane; the 3D versions show the vertical component of the distortions.

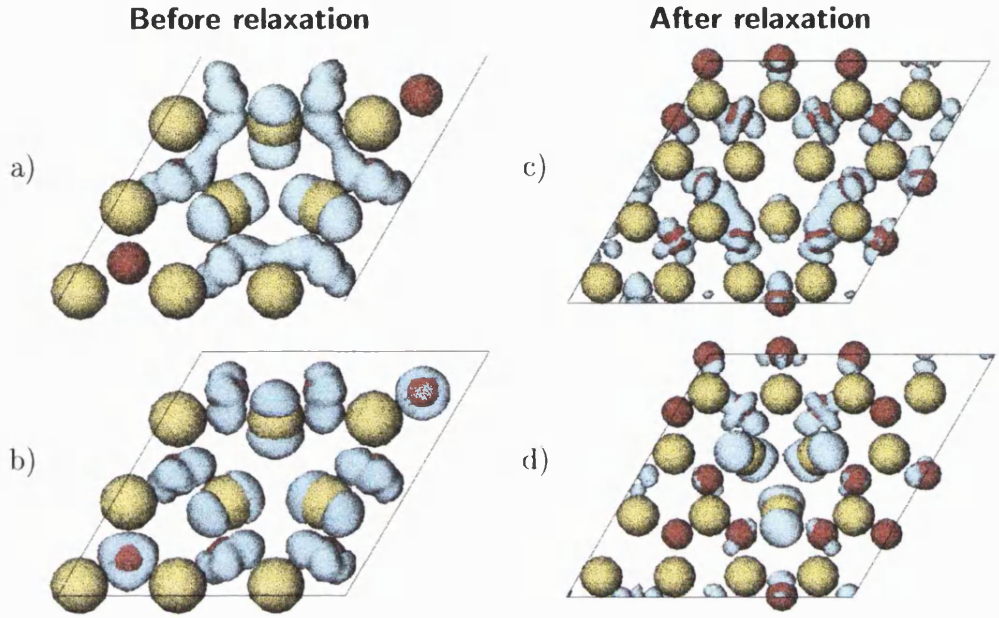

Figure 5.15: The filled (top) and empty (bottom) gap-states for $MoTe_2$ with a Mo vacancy located at the centre of the cell; a) and b) are for the undistorted geometry; c) and d) are for the relaxed geometry where there is an apparent reversal of states with respect to the equivalent MoS_2 system (Figure 5.8). The isosurfaces were taken at a charge per unit volume of 0.001au per state. The red and yellow spheres represent the Mo and Te atoms respectively.

reconstruction of the surface results in a surface buckling which lowers the sulphur atoms nearest the vacancy, and the image shows a trimer of *darker* peaks around the vacancy. It does not seem unreasonable to expect that, within the Tersoff–Hamann model, imaging under tip-negative bias would again show a trimer of brighter peaks above the vacancy. Figure 5.18 shows the calculated empty-state STM image for the metal-vacancy $MoTe_2$ system; the trimer structure is visible in the centre of the image. In this case however, the trimer is surrounded by four other peaks of increased apparent height near the vacancy. These arise from the buckled nature of the underlying surface, where the atoms beneath the 'extra' bumps are raised $\sim$ 0.4au relative to the rest of the surface, and $\sim$ 0.8au relative to the trimer-associated atoms (this effect

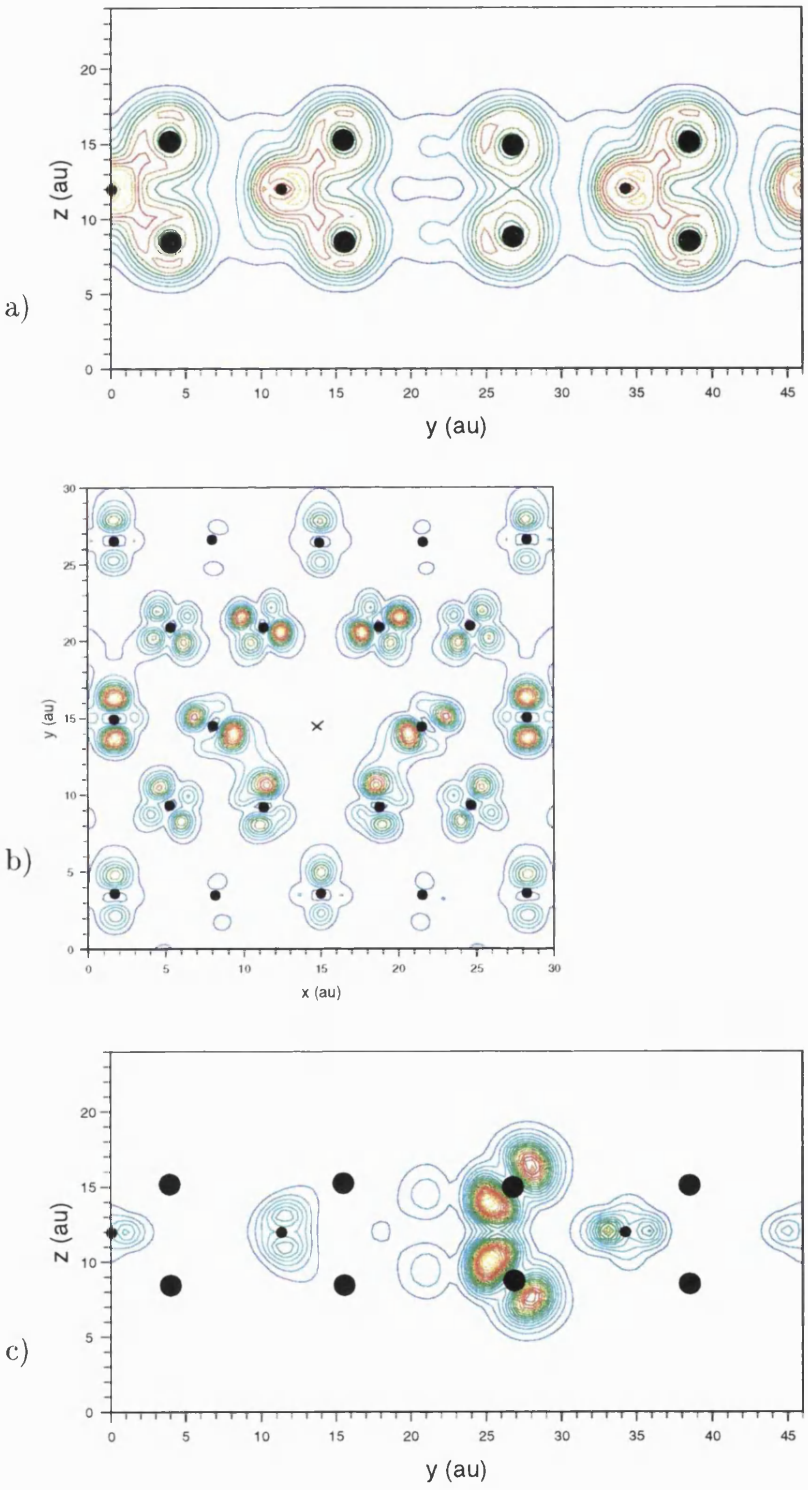

Figure 5.16: a) Total, b) filled gap-state, and c) empty gap-state charge density for $MoTe_2$ with a Mo vacancy (centre of slice). For (a) and (c), the slice is taken along the C_2 symmetry axis (the cartesian y-axis) through the vacancy site, (b) is taken in the Mo plane.

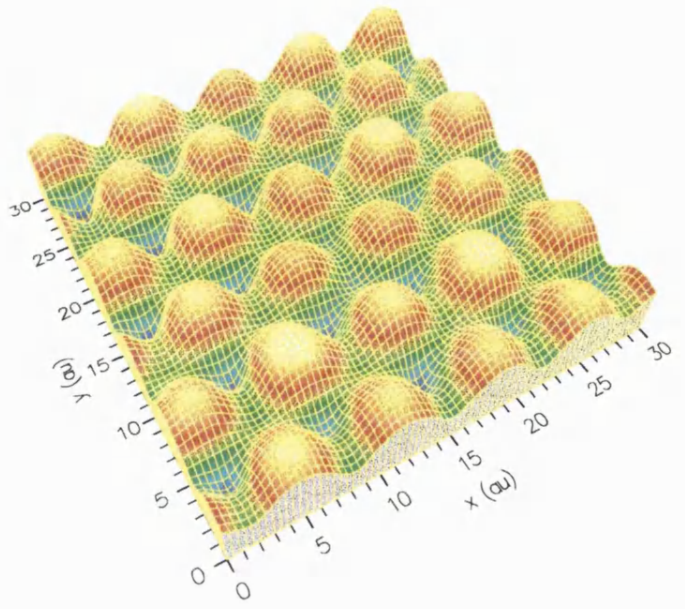

a)

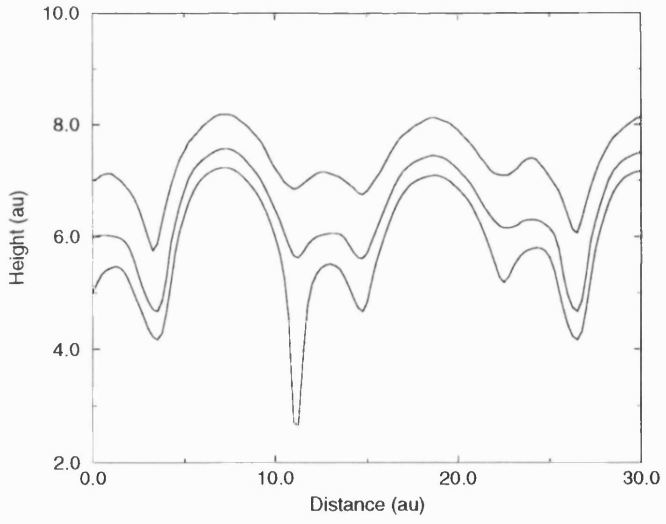

b)

Figure 5.17: a) Calculated STM image and b) STM scan-lines for $MoTe_2$ with a sub-surface metal vacancy for a simulated tip-positive applied bias of 0.8V. The vacancy is located below the centre of the slightly darker trimer structure shown in the 3D image. The peaks occur above the sulphur atoms and the lack of the trimer-peak structure (*cf.* Figure 5.10) is a result of a re-ordering of the gap-states. The relative heights of the peaks reflect the underlying atomic structure which is no longer exactly planar. The scan-lines are taken in the y direction at $x = 15$au (heights are relative to the Mo plane); the uppermost curve corresponds to the topographic image in (a).

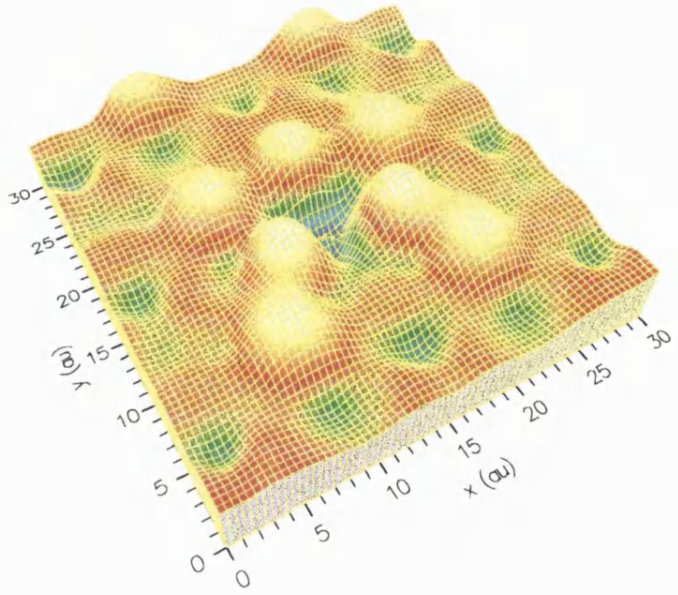

Figure 5.18: Empty-state (surface-positive) Tersoff–Hamann STM image of the $MoTe_2$ surface with a single Mo vacancy (centre of the image) at a tip bias of -0.8V. The image shows the trimer-peak structure observed on MoS_2 for a sample-negative bias (Figure 5.10).

can also be seen in the filled-state image). Since the four-atom feature appears $\sim$ 8au higher than the main surface there must also be some further localised electronic contribution originating from states in the conduction band, but no individual state which might be responsible for the feature could be found.

It is important to appreciate that the Tersoff–Hamann approximation ignores a couple of potentially important factors. The tip, for example, is effectively ignored and could be particularly important with regard to the reversal of contrast in the trimer–peaks predicted here. With the tip in such close proximity to the sample, even under zero bias conditions, there will be some charge transfer between the tip and sample (the contact potential) which may change the occupancies of the gap-states and possibly result in the trimer peaks being observed on $MoTe_2$ for sample negative biases. The bias and electric field could

also alter the state occupations with the possibility that previously unoccupied states close to the Fermi level may become occupied, thereby changing the STM image. The important point is that producing a metal vacancy on the TX_2 surface will, at some material-dependent energy, result in localised p-orbital gap-states on the nearest neighbour chalcogen atoms. As a result the STM image will, at some bias, show a trimer of peaks around the vacancy, and likewise, for the opposite bias the trimer will disappear. A further point of note is that the Jahn–Teller distortion observed here could be a possible explanation for the asymmetry observed in the experimental images of Fuchs et al. on the WSe_2 surface. Whether this is the case will depend on the ordering of the levels around the vacancy in that material.

5.4 Conclusions

This chapter reported on PAW simulations of single-atom (metal or chalcogen) vacancies on the surfaces of MoS_2 and $MoTe_2$. In each case, 3×3 (4×4 for $MoTe_2$ with Mo vacancy) single-slab cells were used with a vacancy created by removing one atom and its associated valence electrons from the cell. This setup implicitly assumes that the vacancies are neutral, which may not be the case as MoS_2 and $MoTe_2$ are semiconductors and may therefore maintain charged defects.

Creation of the vacancy defects caused localised states in the surface band-gap, which (within the Tersoff–Hamann approximation) can contribute to the STM image. Whether localised gap-states contribute to the tunnelling current in a real STM is a topic of discussion (Lawunmi & Payne 1995) and will depend on many things such as how deep the levels are in the gap, the tip-induced band-bending at the surface, and the doping of the sample. These effects were not considered in these simulations, and the Tersoff–Hamann approximation is assumed to provide a good first approximation to an STM image.

The simulations showed that the chalcogen vacancy systems behave in similar ways for both MoS_2 and $MoTe_2$, with the gap-states being localised around the metal atoms and not contributing greatly to the STM image. In both cases, the STM image of the chalcogen vacancy showed a monatomic hole at the site of the vacancy.

It was discovered however, that the two metal-vacancy systems behaved in fundamentally different ways. The MoS_2 system again showed little relaxation, and dangling-bond p-states associated with the sulphur atoms nearest the molybdenum vacancy resulted in a trimer of brighter peaks above the nearest-neighbour sulphur atoms. This is qualitatively the same result as that obtained by Whangbo et al. (1995) except that in their case, the trimer of peaks appeared for the empty-state image and not the filled-state image as found here. The work of Whangbo et al. (1995), though, was based on the EHTB technique which is not as accurate at the PAW technique. The $MoTe_2$ system is found to be a Jahn–Teller system which leads to a symmetry-reducing distortion of the lattice and an inversion of the filled and empty gap-states compared with MoS_2. This reversal of the gap-state order means that the filled-state STM image of $MoTe_2$ with a metal vacancy does not show the trimer of peaks observed on MoS_2. In fact, owing to the distortion of the lattice, which lowers the nearest-neighbour tellurium atoms towards the molybdenum plane, the trimer of nearest-neighbour Te atoms appear darker than the surrounding atoms. Reversing the tip bias to image the empty states of the surface reveals the bright trimer peaks once more along with some additional brighter peaks associated with the actual topography of the surface. Whether this effect is seen in experimental conditions will depend on factors not taken into account in the Tersoff–Hamann approximation, such as the transfer of charge from the tip to sample (contact potential) and the tip–sample bias/ electric field which could alter the occupations of the gap-states and therefore the contrast of the trimer structure. The important point though, is that for any planar,

semiconducting TX_2 at some energy there will be p-states localised around the chalcogen atoms nearest the metal vacancy. Correspondingly, at some material-dependent applied bias the STM will observe the atoms nearest the vacancy as brighter (higher) than the surrounding atoms.

Based on these calculations it seems likely that the monatomic holes and trimer peaks observed by Fuchs et al. (see Figure 4.3) and others on MoS_2 and WSe_2 are due to single chalcogen and metal vacancies respectively. Another possible source of the observed defects is atomic substitution, *e.g.*, Whangbo et al. (1995) carried out EHTB calculations on Mn substitution on MoS_2 (electron donor) which also resulted in a trimer of peaks on the nearest-neighbour sulphurs. However, since the modification experiments were carried out under UHV conditions and could be produced with a variety of tip materials (W, Ir and Pt—ruling out tip-atom substitution), the vacancies are the most likely candidates for the observed features. The Jahn–Teller nature of the metal vacancy on $MoTe_2$ leads to a possible explanation for the asymmetry observed in the trimer structures on WSe_2 (Figure 4.3b). However, it seems unlikely that, if WSe_2 with a tungsten vacancy were a Jahn–Teller system, the distortion would always occur in the same direction as is observed (*i.e.*, the C_2 axis is always pointing in the same direction despite the fact that there are three equivalent choices on reduction of symmetry from D_{3h} to C_2). It is possible that the co-operative Jahn–Teller effect could produce such alignment, but the defects are well separated and produced at room temperature (probably too high for weak strain-coupling effects to occur), so this is unlikely. Perhaps the most likely explanation is that the asymmetry is due to the structure of the tip.

Chapter 6

STM-Induced Vacancy Formation on the MoS_2 Surface

6.1 Introduction

Section 4.1 also forms a general introduction to this chapter. In Chapter 5 the PAW method was used to study the electronic structure and STM images of vacancy defects on the MoS_2 and $MoTe_2$ surfaces in order to explain some of the STM images obtained after modification of the TX_2 surfaces with the STM tip. The conclusion reached there and by other groups (Whangbo et al. 1995) was that STM pulsing on the transition-metal dichalcogenide surfaces can produce monatomic vacancies in both the surface chalcogen and the sub-surface metal layers. The ability to modify surfaces on the atomic scale is becoming increasingly important as the need for smaller electronic and mechanical devices becomes greater. It is therefore important that the processes behind surface modification with the STM are understood and it is toward this end that several theory and simulation groups are working.

Tsong (1991) extended conventional field-evaporation theory (Gomer 1959, Gomer & Swanson 1963, Müller & Tsong 1969) to the specific geometry of the

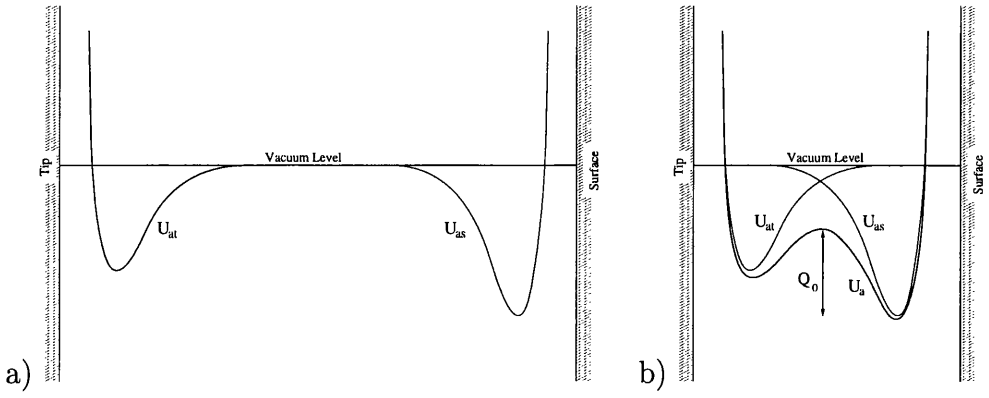

Figure 6.1: Atomic potentials for an adsorbate-tip-sample system for a) large and b) small tip–sample separations. At small separations, the overlap of the tip– and sample–adsorbate barriers produces a double potential well with an effective barrier of height Q_0.

Scanning Tunnelling Microscope. For large tip–sample separations, the wells in the adsorbate–tip potential U_{at} and the adsorbate–sample potential U_{as} do not overlap and the probability atom of transfer in either direction is minimal (Figure 6.1). However, when the tip and sample approach each other the U_{at} and U_{as} potential wells overlap so that the total potential is (to first approximation) $U_a = U_{at} + U_{as}$ with an atom-transfer barrier Q_0 (Figure 6.1b). Using a similar argument, an ion-transfer potential curve may be approximated by $U_i = U_{it} + U_{is}$ where U_{it} and U_{is} are the ion–tip and ion–sample potentials respectively (Figure 6.2). Upon application of an electric field the ionic potential will be modified to become $U_i = U_{it} + U_{is} - q\mathcal{E}z$ where q is the charge on the ion and $\mathcal{E}$ is the magnitude of the electric field. From this simple theory an expression for the field required to evaporate ions from the surface with the STM can be obtained (Equations (3) and (4) in Tsong (1991)) which predict evaporation fields around 3–4VÅ^{-1} for gold and tungsten. This approach however does not shed much light on the actual mechanisms behind the surface-modification process—the tip-surface interactions are completely ignored and no predictions are made as to the atomic and electronic configuration as the atom is actually

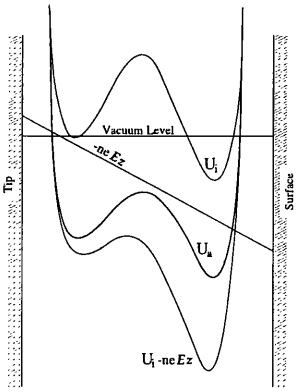

Figure 6.2: Potentials for transfer of an atom (U_a) and an ion of charge q (U_i) between the tip and sample under an applied electric field $\mathcal{E}$ in the z direction.

in the process of being removed.

Lang (1992, 1994) has studied the effect of the electric field on the transfer of aluminium atoms between two jellium electrodes held at different potentials. He concluded that greatest barrier-lowering effect is that of the tip–sample interaction (arising from their close proximity), but that the presence of the field provides an additional lowering of the barrier. The results also indicated that the field required for atom transfer depends strongly on the tip–sample separation, and that total charge appearing on the transferred atom never exceeds 0.1 electron charges, which is unsurprising given that the atom is never far from either the positive surface or the negative tip.

Hirose & Tsukada (1994) have studied Al atom transfer between an Al surface and tip, which are in turn connected to jellium electrodes with different Fermi levels (Figure 6.3). The wavefunctions are expanded as

$$\psi(\mathbf{r}) = e^{i\mathbf{k}_{||}\cdot\mathbf{r}_{||}} \sum_{G_{||}} e^{i\mathbf{G}_{||}\cdot\mathbf{r}_{||}} \phi\left(G_{||}, z\right), \tag{6.1}$$

where $G_{||}$ are a set of 2D reciprocal-lattice vectors, *i.e.*, the system is periodic in two dimensions. $\phi\left(G_{||}, z\right)$ is obtained by a matrix-recursion method, where

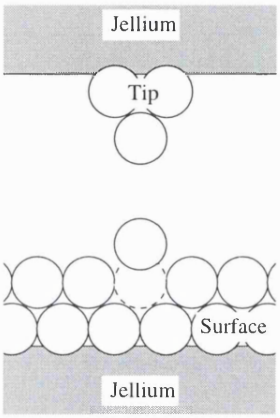

Figure 6.3: Geometry of the simulations carried out by Tsukada et al. The surface is represented by a slab and the tip by a pyramid of Al atoms; both are mounted on $r_s = 2$ slabs of jellium held at different potentials.

the Schrödinger equation is integrated from a point where the wavefunctions are known (deep in the surface) through the vacuum gap and into the tip. The LDA and local pseudopotentials are used and the effective potential, electron density, and the current density are all obtained from the calculations. They show that as the tip approaches the surface under bias a 'hole' opens up in the electron barrier through which a ballistic-electron current can flow, eventually forming a bridge of charge between the tip and sample. The potential barrier for atom transfer between the tip and sample is shown to have two distinct minima at zero bias corresponding to the atom in the surface, or adsorbed on the tip. As the (surface-positive) bias is increased, the barrier against atom transfer reduces, eventually disappearing at a bias of 8.0V for a tip–sample separation of 14au (7.4Å).

However, so far there have been no simulations relating to the STM-induced extraction of atoms from partially ionic materials, such as the transition-metal dichalcogenides, which also include effects due to the tip bias (but see Shluger & Kantorovich (1997) and Livshits & Shluger (1997) which examine atom transfer and tip contamination in Atomic Force Microscopy (AFM) of ionic

surfaces). This chapter reports on PAW simulations of a MoS_2 sample surface in the presence of a Mo tip, with and without an applied external electric field. Section 6.2 covers the method of implementation of the electric field within the PAW method (Appendix D details some preliminary calculations on the MoS_2 surface (without a tip) which are relevant to this section). Sections 6.4 and 6.5 cover the zero-field and finite-field calculations on MoS_2 respectively and Section 6.6 concludes the chapter.

6.2 Electric field in PAW

The Projector Augmented Wave method (Section 2.7) relies on the use of plane-waves to describe the electron wavefunctions. For a discrete system using a finite number of planewaves this implies the existence of periodic boundary conditions, which requires that any potential term included in the total PAW potential must have the periodicity of the simulation cell. In addition, the potential must be well-representable in both real and reciprocal space or Friedel-like oscillations will appear in the potential upon transformation from real to reciprocal space and back again.

There are a number of ways in which to define a potential with the above characteristics to represent a constant electric field. The method used here is that of Ness & Fisher (1997a) where a potential V_{APP} is added to the self-consistent potential having the form

$$V_{\mathrm{APP}} = \mathcal{E}_{\mathrm{APP}} \left[z - z_0 - \frac{c_0}{1 + e^{\beta(z_c - z)}} \right] \qquad (0 \leqslant z \leqslant c_0), \tag{6.2}$$

where $\mathcal{E}_{\mathrm{APP}}$ is the magnitude of the applied field; z_0 is the position of the zero of the potential; z_c is the mid-point of the Fermi cutoff function; c_0 is the cell dimension in the z direction; and β is a smoothing parameter. This potential has a 'rounded sawtooth' shape and is equivalent to introducing a

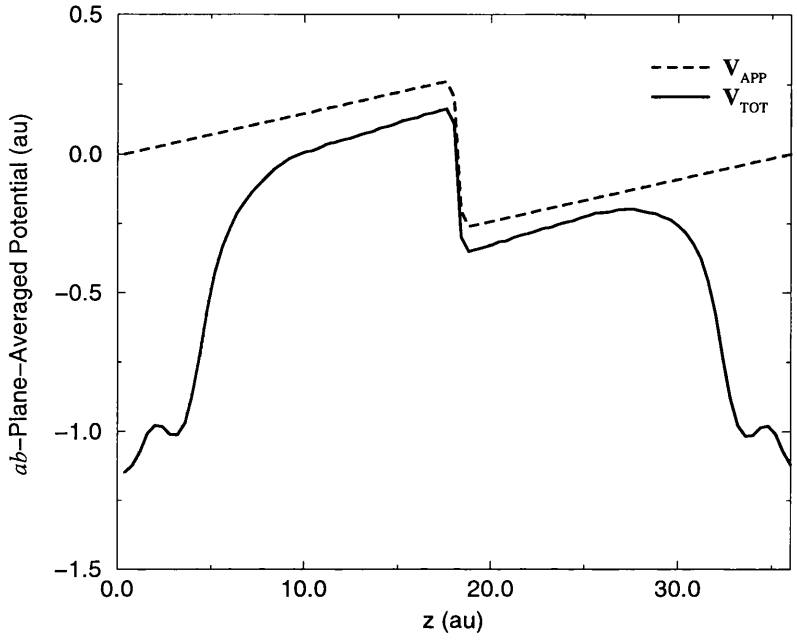

Figure 6.4: Rounded-sawtooth external potential (V_{APP}) and the ab-plane-averaged total potential for the MoS_2 surface. These potentials were calculated for $\beta = 2.0$au and an applied field of 0.015au ($0.772\mathrm{V\AA}^{-1}$) (see Equation (6.2)). The effective field in the vacuum gap is actually 0.21au ($1.08\mathrm{V\AA}^{-1}$) owing to the periodic boundary conditions and the polarisation of the slab.

planar capacitor of width $\sim \beta^{-1}$ at position z_c. Figure 6.4 shows V_{APP} and the total self-consistent potential (averaged in the ab-plane) of a single layer of MoS_2 (Section 4.3) for an applied field of $\mathcal{E}_{\mathrm{APP}} = 0.015$au ($0.772\mathrm{V\AA}^{-1}$) and $\beta = 2.0$au. An important feature of Figure 6.4 is that the combination of periodic boundary conditions and a polarisable slab results in an effective electric field in the vacuum gap larger than the applied field ; the effective field in these MoS_2 simulations (the gradient of the potential in the vacuum region) is 0.021au ($1.08\mathrm{V\AA}^{-1}$). For further discussion, see Appendix D.1 or Ness & Fisher (1997a).

It is worth noting that extra care must be taken when choosing the di-

mension of the simulation cell in the direction of the field. The cell must be chosen large enough such that the region in which the charge is depleted/ accumulated by the field does not overlap the cutoff region (the 'capacitor' region $\sim \beta^{-1}$ around z_c). However, if the slab-to-boundary distance is too large, bound (trapped) states may form in the potential well at the cutoff boundary which could be lower in energy than those in the slab resulting in a spurious 'spilling out' of charge form the slab of material to the potential well (the static equivalent of field emission). This problem is easily identified and can be avoided by a suitable choice of applied fields and cell dimensions. Assuming no trapped states exist, and the regions of interest are well separated from the 'capacitor' then variations in z_c and β will not alter the results (unless β is made too large for the sawtooth potential to be well-described by planewaves up to the chosen energy cutoff, in which case the Friedel-like oscillations will appear in the potential).

6.3 Simulation Details

The MoS_2 surface was approximated by the same 3×3 single-slab used in the previous chapters. For all calculations, the surface atoms are fixed in their equilibrium surface positions as calculated in Section 4.3. The tip, whose apex was positioned over either an Mo or S atom site, consisted of a 5-atom molybdenum cluster held in its relaxed geometry subject to the constraint that the four base atoms remain in a plane (see Figure 6.5 and Appendix C.1.1). A planewave cutoff of 15Ry was used throughout for the wavefunctions and only the Γ point is considered.

Figure 6.6 shows the full tip–sample cell with the tip positioned over a Mo site 11au (5.82Å) away from the surface Mo plane (the Mo atom below the tip apex has been moved towards the tip—see below). The c dimension used in these simulations was 36au (19.05Å)—Figure 6.7 shows schematically the

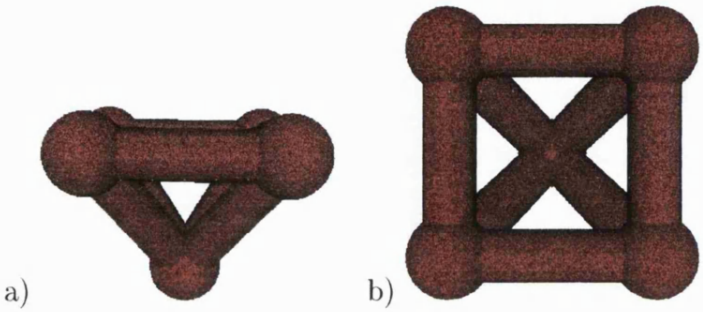

Figure 6.5: The atomic structure of the five-atom Mo-cluster tip used in the atom-extraction simulations in a) side-view and b) plan-view. This structure is the ground-state atomic structure for a five-atom Mo cluster subject to the constraint that four of the atoms remain in a plane.

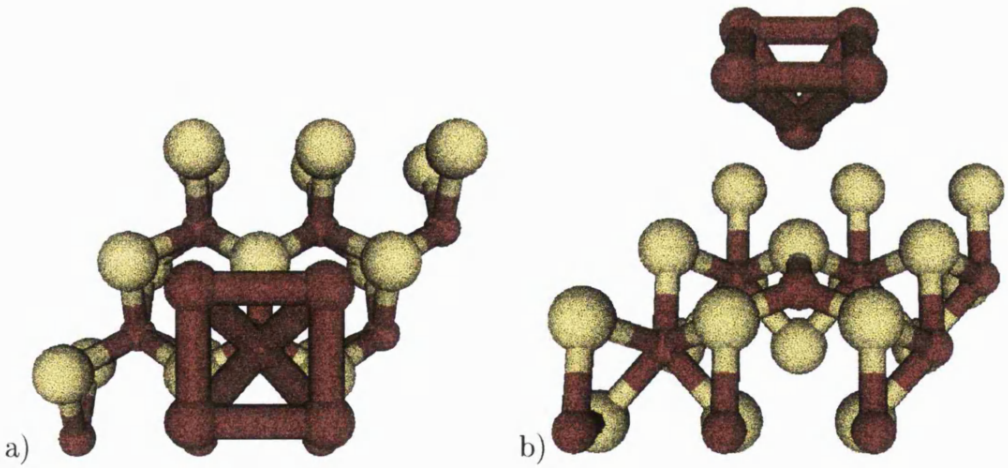

Figure 6.6: The simulation cell used for the atom-extraction calculations from various viewpoints. The tip here is positioned 11au (5.82Å) away from the surface Mo plane above a Mo atom which has been moved 2.8au towards the tip. The position of the tip and atom below the tip will vary depending on the simulation.

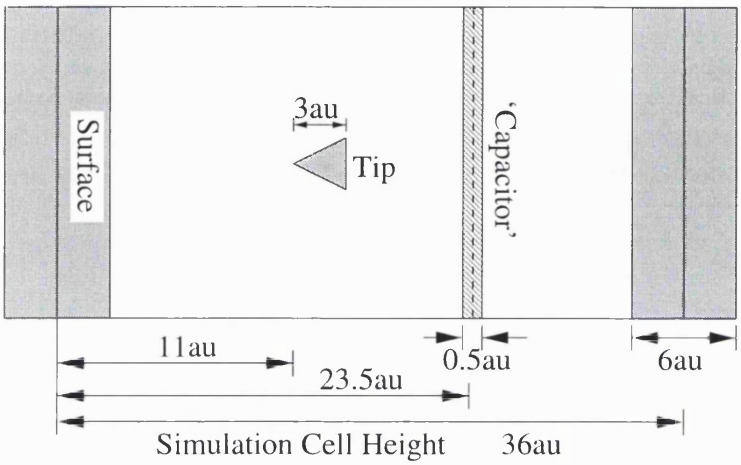

Figure 6.7: Schematic diagram of the simulation cell showing the sizes of the slab, tip and vacuum gap regions. The dotted line shows the plane of the electric-field cutoff (see Section 6.2)—the cutoff is placed midway between the tip base and the lower side of the surface. This leaves a distance separating the cutoff from the tip base and the surface of 9.5au (5.03Å).

relative sizes of the slab, tip, and the vacuum gaps between them. With the tip apex positioned 11au from the Mo plane, the distance between the base of the tip and the image-surface sulphur atoms (from periodic boundary conditions) is $\sim$ 19au (10Å).

For all calculations including an electric field, the field cutoff was positioned halfway between the tip base and lower surface (*i.e.*, 9.5au from each) which, as shown later (Section 6.5), is enough space to remove any interactions between the field cutoff and any of the atoms in the cell. The applied electric field had a magnitude of 0.015au (0.772VÅ^{-1}) and was directed towards the tip (*i.e.*, a tip-negative bias to extract preferentially positive ions). For the tip–sample separations considered this gives a nominal tip-negative applied bias of around 3.5–4.5V depending on the points of reference; the bias used in the surface-modification experiments on MoS_2 was 5V (tip negative) (Hosaka et al. 1995).

Atom extraction barriers were calculated for extraction of both Mo and S atoms from the surface, with and without an external field of 0.015au

($0.77\text{V}\text{Å}^{-1}$). In each case, the tip is positioned 11au above the atom to be extracted (also 10au for sulphur), which is then moved in steps (of 0.4 or 0.8au) towards the tip apex in a straight line. No further atomic relaxation is allowed in the main calculations, however several support calculations were carried out (*e.g.*, to determine the equilibrium tip–adsorbate separation) which are detailed in Appendices C and D and referenced where relevant in the following sections.

6.4 Zero-Field Atom Extraction

6.4.1 Atom-Extraction Barriers

Figure 6.8 shows the calculated barriers against extraction of single sulphur and molybdenum atoms from the MoS_2 surface. The barriers are obtained from the difference in total energies between the systems in their ground-state and the systems with one surface atom displaced towards the tip. 'Ground-state' here refers to the electronic ground-state with the tip and surface held in their preferred atomic configuration when separated—no further atomic relaxation was allowed in the barrier calculations. Shown are two extraction barriers for sulphur, one with the tip at 10.0au and the other with the tip at 11.0au from the Mo plane, and one barrier for molybdenum extraction with the tip at 11.0au.

The sulphur-extraction barriers will be considered first (blue and green curves in Figure 6.8). The first thing which becomes apparent is the separation dependence of the barrier. With the tip apex at 11.0au (*i.e.*, $\approx$ 8.0au from the surface sulphur plane) there is a second minimum in the barrier occuring at (approximately) the equilibrium tip–sulphur separation of 4.17au (2.21Å) (corresponding to a sulphur position of z=6.83au on the graph) calculated in the absence of the surface (assuming the sulphur atom remains on a line

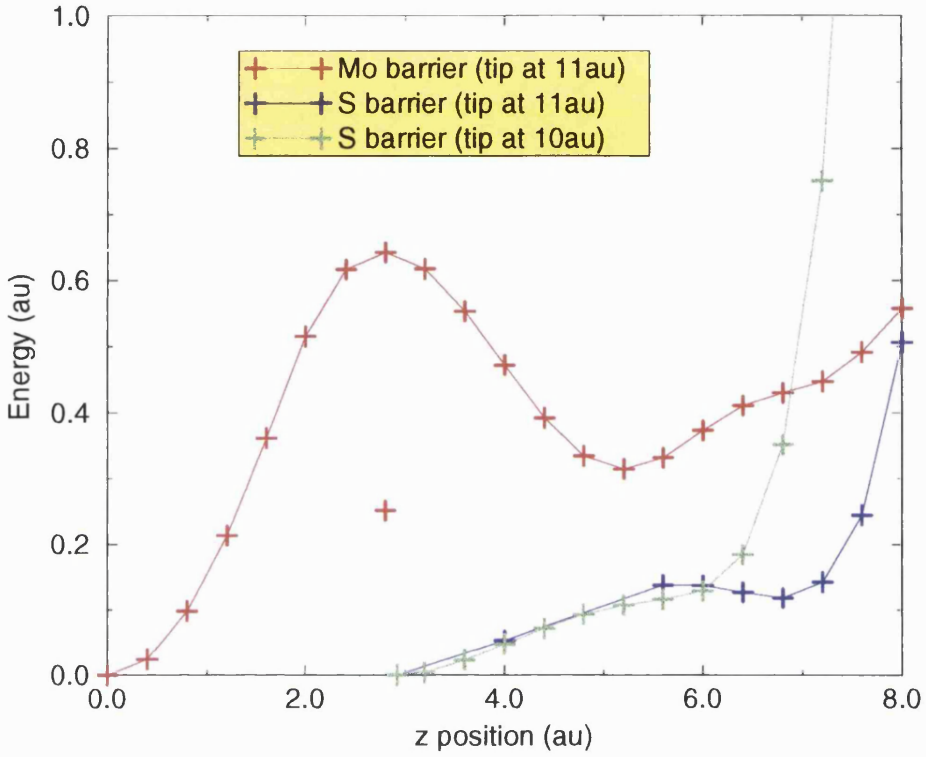

Figure 6.8: Barriers against extraction of single molybdenum and sulphur atoms from the MoS_2 surface. The large peak in the Mo extraction barrier is a result of the lack of atomic relaxation in the simulation. The single point shows the effect of full surface relaxation with the extracted atom at the barrier peak (*i.e.*, in the plane of the surface sulphur atoms)— in this adiabatic limit, the peak disappears. See text for further discussion.

perpendicular to the tip through the apex; see Appendix C.2.1). This implies that the sulphur atom is no longer bound to the surface, but is adsorbed on the tip—a fact confirmed by examining the charge density (see Section 6.4.2). The barrier prior to the tip-adsorption minimum, which must be overcome for transfer of the atom from the surface to the tip, has a maximum at an energy of 0.14au (3.81eV). However, with the tip positioned one atomic unit closer to the surface (*i.e.*, $\approx$ 7.0au from the surface sulphur plane), the barrier has been removed and there is no longer a minimum associated with the atom adsorbed

on the tip.

The vanishing of the barrier maximum for the smaller tip–sample separation is a result of the fact that the sulphur is still bound to the surface at the equilibrium tip–sulphur separation and seems to imply that atom extraction could not occur at this tip–sample separation. However, this conclusion is potentially misleading as it is important to appreciate that Figure 6.8 is really a one-dimensional cut through a three-dimensional potential barrier. A calculation of the full 3D barrier would be extremely costly (both in terms of time and storage) using the PAW technique and, it turns out, largely unnecessary. Appendix C.2.2 describes support calculations carried out on the tip with a sulphur atom adsorbed on it (*i.e.*, no surface) designed to illuminate the 3D structure of the barrier. These calculations showed that the tip–adsorbate potential is very flat in the plane perpendicular to the tip at the equilibrium tip–sulphur separation. Also, allowing the sulphur atom to relax fully around the fixed tip lowered the system energy by 0.086au (2.34eV) relative to the energy at the equilibrium separation on the tip apex. On the other hand, there is almost no surface relaxation about a sulphur vacancy in the absence of a tip. This implies that there is a minimum associated with the extracted atom adsorbed on the tip, but it lies off the chosen line, and that the barrier would not be significantly reduced by allowing surface relaxation. The most likely trajectory of an extracted sulphur atom is along the straight line towards the tip apex up to or near the point of equilibrium separation, whereupon the atom will 'slide' around the side of the tip. Hence it is still possible that sulphur atoms could be extracted even for the lower tip–sample separation with an effective barrier against extraction given approximately by the value of the barrier at the equilibrium tip–sulphur separation, *i.e.*, 0.11au (3.00eV).

The molybdenum extraction barrier shown (red curve) is that with the tip placed at 11.0au from the Mo plane and has a different form to those for sulphur extraction. The barrier is much higher than that against sulphur

extraction, and there is a large peak (height 0.64au) located at $z = 2.8$au from the Mo plane, *i.e.*, almost in the plane of the surface sulphur atoms (at 2.92au). This large peak is a result of the fact that atomic relaxation was not allowed in the calculations and corresponds to the Mo atom 'squeezing' through the surface S layer. A separate calculation (Appendix D.3) involving only the surface with the Mo atom placed 2.8au away from its equilibrium position, which also allowed atomic relaxation, resulted in a lowering of system energy by 0.339au (9.24eV). The single red point in Figure 6.8 shows the effect the surface relaxation would have on the barrier—if the Mo atom were extracted adiabatically from the surface (*i.e.*, if the calculation allowed full atomic relaxation), the large barrier would be totally removed.

As the extracted Mo atom approaches the tip, the potential curve starts to resemble that for extraction of sulphur with the tip placed at 10au, *i.e.*, there is no minimum associated with the atom being adsorbed on the tip. The equilibrium tip–molybdenum separation (Appendix C.2.1) was found to be 4.02au (2.13Å), which corresponds to a z position of 6.98au on Figure 6.8. However, as noted above, the lack of a minimum does not necessarily imply that atom extraction is not possible at this separation. Calculations on the tip with a molybdenum adsorbate (Appendix C.2.2) show that the tip–Mo potential is flat in the plane perpendicular to the tip, through the equilibrium tip–Mo separation. Also, full relaxation of the molybdenum adsorbate around the tip lowered the energy by 0.15au (4.1eV) relative to its equilibrium position above the tip. The conclusion, then, is the same as before: it should be possible to extract Mo atoms at this tip–sample separation, and the effective barrier is approximately that at the equilibrium tip–Mo separation, *i.e.*, 0.44au (12.0eV).

The energies required to evaporate single neutral atoms from the surface were calculated (Appendix D.2) at 0.83au (22.6eV) for molybdenum and 0.31au (8.45eV) for sulphur. Table 6.1 summarises the barriers against extraction of molybdenum and sulphur atoms with the tip at 11au from the Mo

	Barrier height (au (eV))	Evaporation energy (au (eV))
S	0.14 (3.81)	0.31 (8.45)
Mo	0.44 (12.0)	0.83 (22.6)

Table 6.1: Barrier height against extraction of single Mo and S atoms from the MoS_2 surface in the presence of a tip (at 11au from the Mo plane) compared to the energy required to evaporate a neutral atom from the surface. The tip effectively halves the barrier.

plane and compares them to the evaporation energies. The presence of the tip has reduced the energy required to extract atoms from the surface by a factor of two.

Assuming that the atom-extraction process is thermally activated, the equation

$$\kappa = \nu \exp\left(\frac{-\Delta E}{k_B T}\right) \tag{6.3}$$

can be used to estimate either the extraction probabilities for a given temperature or the temperatures required for a given extraction rate. Here κ is the extraction rate, ν is assumed an effective 'attempt frequency' (but in reality may include other terms such as entropy), ΔE is the barrier height, k_B the Boltzmann constant, and T the temperature. The frequency of attempts to overcome the barrier is obtained by making the further assumption that the atom to be extracted is oscillating in an harmonic potential given by fitting to the first two points of the barrier in Figure 6.8. At 300K the calculated rate of atom extraction is far too low ($\kappa \lesssim e^{-100}\mathrm{s}^{-1}$) for the process to occur in any experiment. Table 6.2 shows the calculated oscillation frequencies and the local temperatures required to extract atoms at rates of $10^3\mathrm{s}^{-1}$ and $1\mathrm{s}^{-1}$. These temperatures are much higher than those likely to occur on the surface

Atom Type	Oscillation Frequency ($\times 10^{12}$Hz)	Extraction Rate (s^{-1})	Required Surface Temperature (K)
Sulphur (tip at 10au)	9.1	10^3 1	1500 1200
Sulphur (tip at 11au)	9.1	10^3 1	1900 1500
Molybdenum (tip at 11au)	8.7	10^3 1	6000 4600

Table 6.2: Local surface temperatures required to extract sulphur and molybdenum atoms from the MoS_2 surface based on the zero-field barrier heights in Table 6.1 and the assumption that the atoms oscillate in an harmonic potential with the frequencies given (calculated from the barriers in Figure 6.8).

(Baskin et al. 1996) leading to the conclusion that the presence of the tip alone cannot account for the reproducibility of the atom-extraction experiments.

6.4.2 Bond-Breaking and Gap-State Formation

Under static equilibrium the Fermi levels of the tip and sample systems must equalise. This will occur by the transfer of charge from the material with the higher Fermi level to the material with the lower Fermi level resulting in the contact potential (Ashcroft & Mermin 1976b). Integrating the charge density around the tip and sample regions separately it is found that once equilibrium has been reached, the tip has transferred 0.1 electrons to the MoS_2 surface.

Figures 6.9, 6.10 and 6.11 show the total charge density of the two sulphur-extraction systems (with the tip at 10au and 11au) and the molybdenum-extraction system for various positions of the extracted atom. The slice is taken in a vertical plane through the tip apex and extracted atom—this plane does not go through any of the base atoms of the tip. These figures show in a qualitative way how the atom becomes detached from the surface and bonds

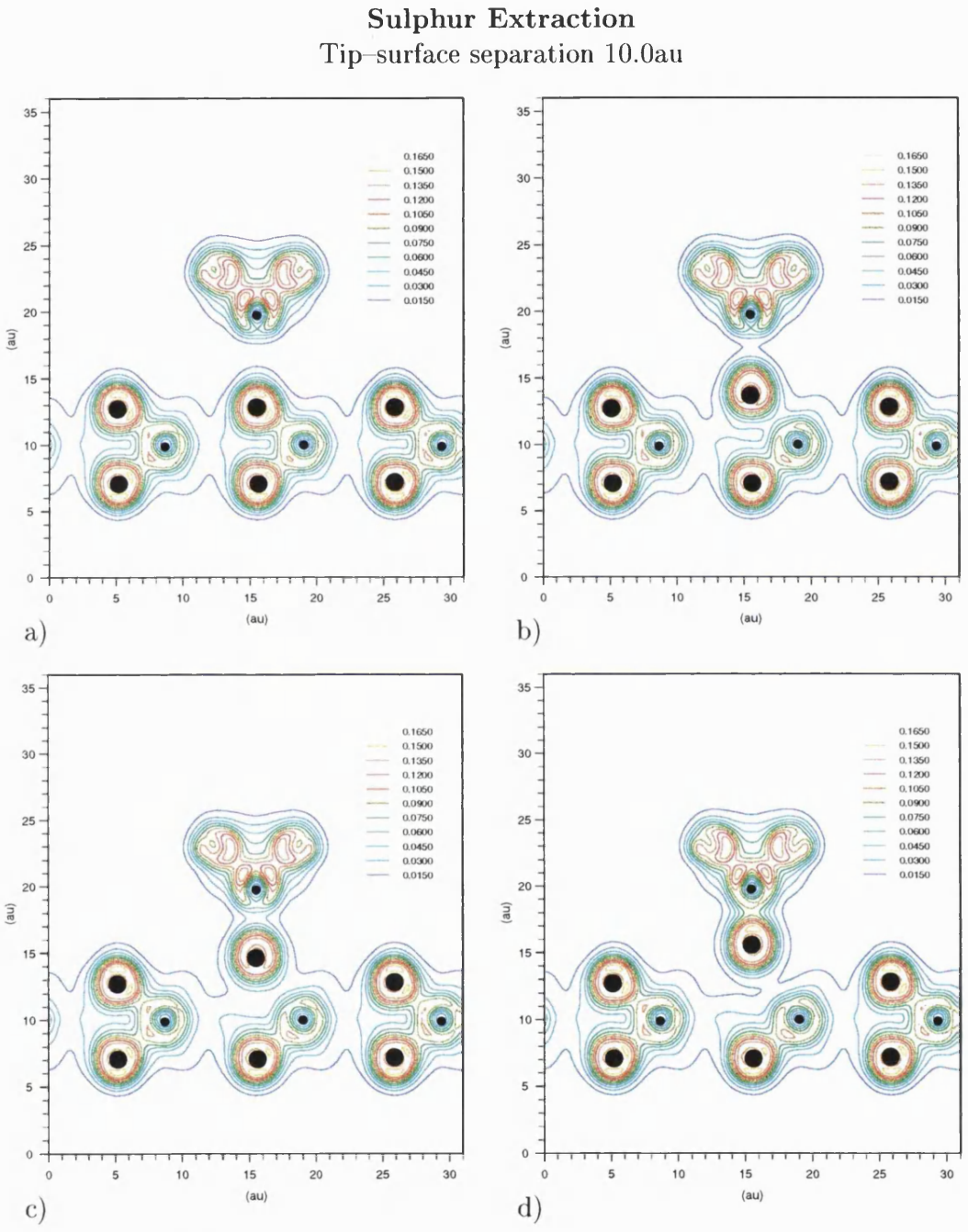

Figure 6.9: Sulphur extraction from the MoS_2 surface in the presence of an STM tip positioned 10.0au from the surface Mo plane with no applied field. Shown are contour plots of total charge density taken in a vertical plane through the tip apex atom and the atom being removed from the surface, showing how the surface–atom and tip–atom bonds break and form respectively as the atom moves from the sample (a) to the tip (d). At this tip–sample separation, the sulphur atom is still attached to the surface when it reaches the equilibrium tip–adsorbate separation.

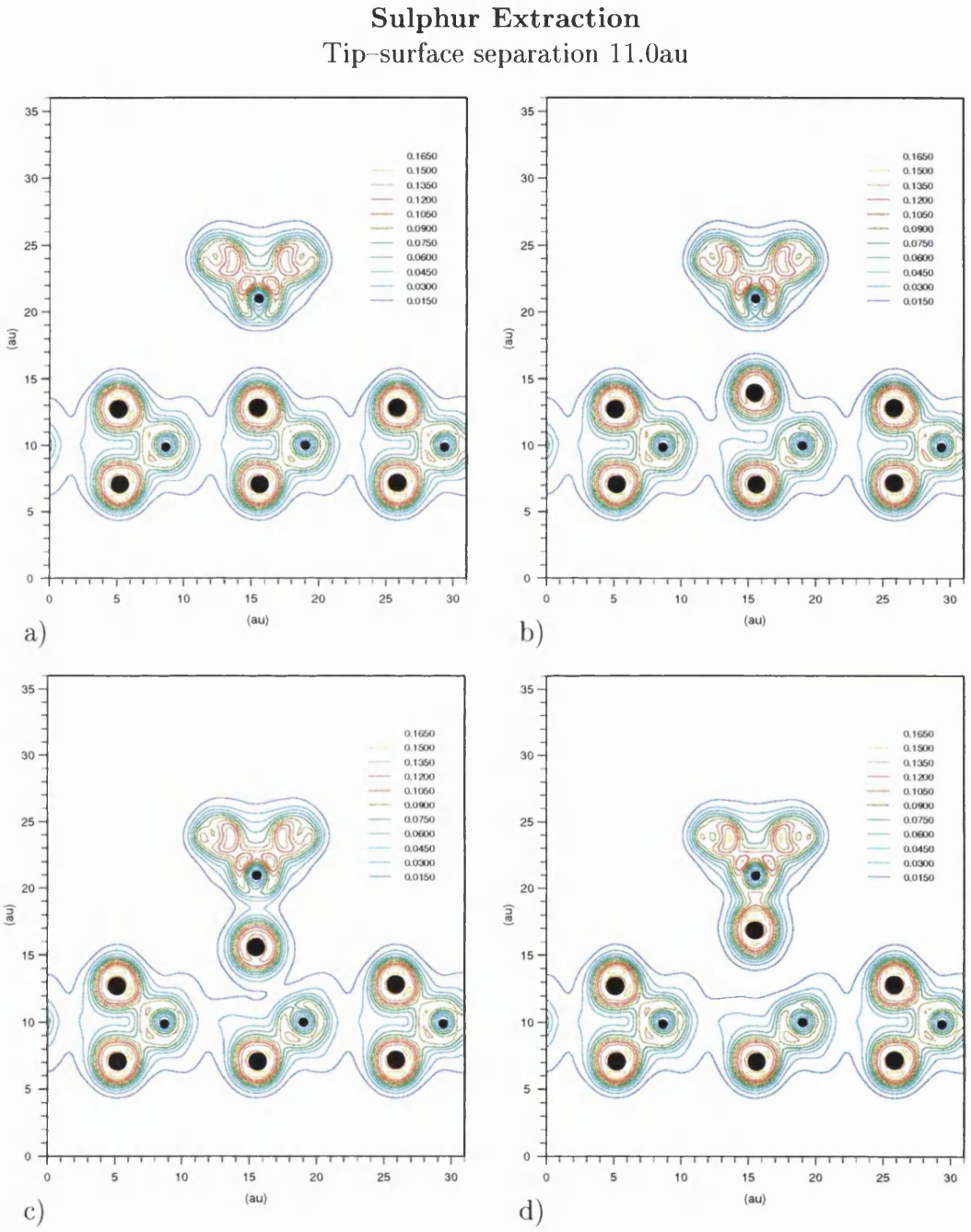

Figure 6.10: Sulphur extraction from the MoS_2 surface in the presence of an STM tip positioned 11.0au from the surface Mo plane with no applied field. Shown are contour plots of total charge density taken in a vertical plane through the tip apex atom and the atom being removed from the surface, showing how the surface–atom and tip–atom bonds break and form respectively as the atom moves from the sample (a) to the tip (d).

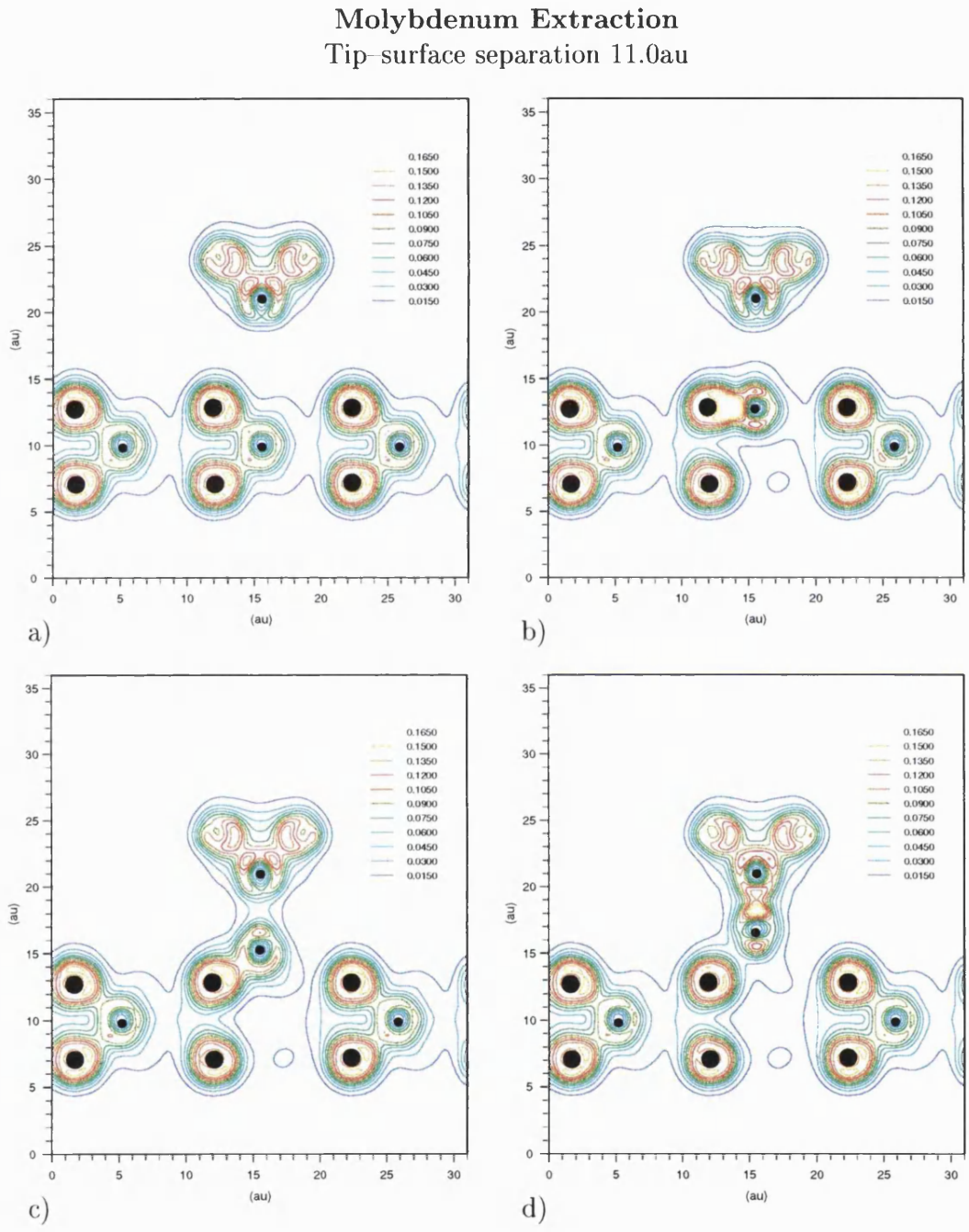

Figure 6.11: Molybdenum extraction from the MoS_2 surface in the presence of an STM tip positioned 11.0au from the surface Mo plane with no applied field. Show are contour plots of total charge density taken in a vertical plane through the tip apex atom and the atom being removed from the surface, showing how the surface–atom and tip–atom bonds break and form respectively as the atom moves from the sample (a) to the tip (d). The Mo atom is still bound to the surface at the equilibrium tip–Mo separation (part d).

to the tip. They also indicate why there are no tip-adsorption minima in the barriers for Mo extraction and S extraction (with the tip at 10au)—at the equilibrium tip–adsorbate separation the removed atom is still bonded to the surface (Figures 6.9d and 6.11d). In hindsight, the lack of a tip-adsorption minimum on the molybdenum extraction curve (where the minimum was apparent on the sulphur-extraction curve at the same tip position) seems reasonable. For the case of sulphur extraction, since the sulphurs are bonded only to the molybdenum atoms (and not any of the surface sulphur atoms), it is the separation between the sulphur and the molybdenum plane which determines the degree of bonding of the atom to the surface. So, the sulphur does not need to move far from its equilibrium surface position before it becomes effectively free from the surface. For the molybdenum however, which in its perfect surface position is bonded to three sulphur atoms from each of the two sulphur planes, moving the atom outside the surface does not break the bonds between it and the top-most sulphur atoms. Hence the Mo atom will still be 'half bound' to the surface at distances up to at least 3au. When the extracted Mo atom is at the equilibrium tip–Mo position, the distance between the extracted atom and the surface sulphur plane is only 4au (2.1Å), and the Mo atom is still partially bound to the surface.

Chapter 5 reported PAW simulations on vacancy defects on MoS_2 (and $MoTe_2$) and showed that the introduction of a vacancy into the MoS_2 surface resulted in electronic states appearing in the surface band-gap which could be associated with the dangling bonds. For these simulations which include a tip, these states will not necessarily appear in the band-gap of the simulation (*i.e.*, they may not be the highest-occupied and lowest-unoccupied molecular orbitals (HOMO and LUMO respectively)) since the states associated with metallic tip tend to have higher eigenvalues than those of the surface. However, it is possible to find states which closely resemble the gap-states observed in the surface-only calculations. Figures 6.12 and 6.13 show selected states from the

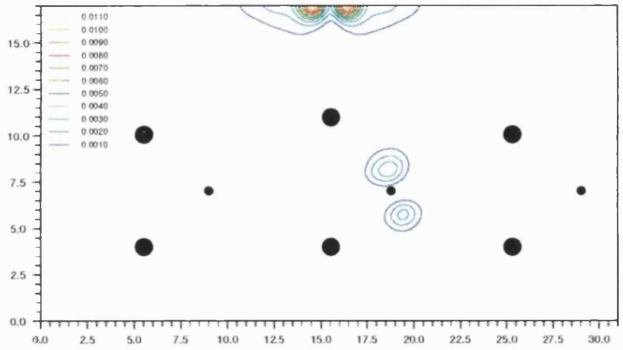

a) $z_S = 4$au; States 93–95 ($E = -7.06$eV to -6.80eV); $E_F = -6.72$eV

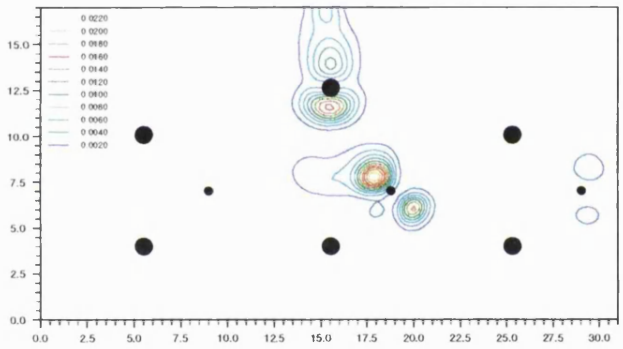

b) $z_S = 5.6$au; States 93–95 ($E = -7.49$eV to -7.34eV); $E_F = -7.32$eV

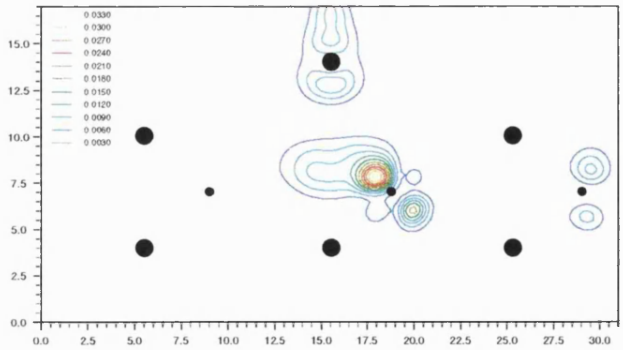

c) $z_S = 6.8$au; States 93–95 ($E = -7.81$eV to -7.62eV); $E_F = -6.72$eV

Figure 6.12: Charge-density contours for selected electronic states as a sulphur atom is extracted form the surface of MoS_2. z_S is the z position of the sulphur atom being extracted from the surface (perfect surface position: $z_S = 2.92$au). As the extracted atom is moved further from the surface, the states start to closely resemble the 'gap-states' in Figure 5.4. The slice is in the vertical plane through the vacancy site and the Mo–S bonds.

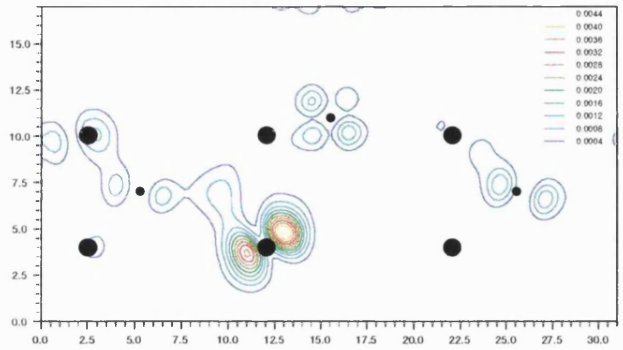

a) $z_{Mo} = 4.0$au; States 89–90 ($E = -7.65$eV to -7.63eV); $E_F = -7.45$eV

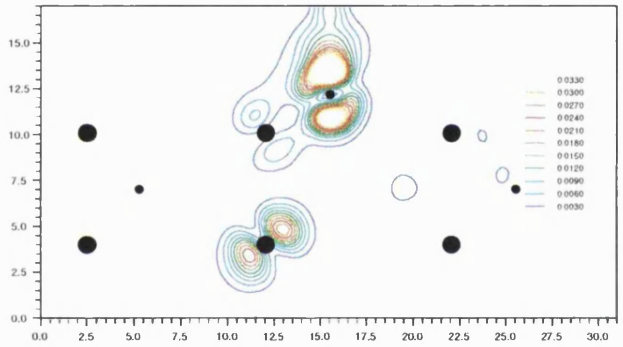

b) $z_{Mo} = 5.2$au; States 89–90 ($E = -7.98$eV to -7.62eV); $E_F = -7.35$eV

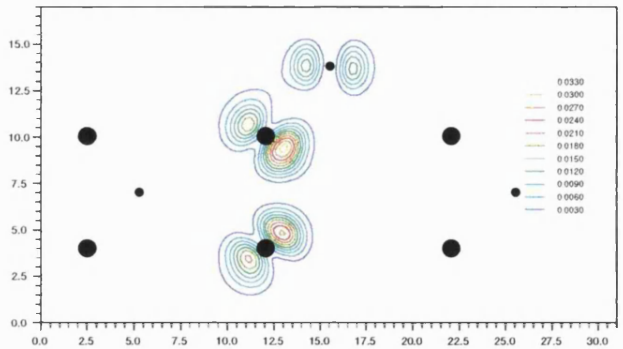

c) $z_{Mo} = 6.8$au; States 91–92 ($E = -8.06$eV to -7.72eV); $E_F = -7.30$eV

Figure 6.13: Charge-density contours for selected electronic states as a molybdenum atom is extracted form the surface of MoS_2. z_{Mo} represents the z coordinate of the Mo atom being extracted from the surface (perfect surface position: $z_{Mo} = 0.0$au). As the extracted atom is moved further from the surface, these states start to closely resemble the gap-states in Figure 5.9b. The slice is in the vertical plane through the vacancy site and the Mo–S bonds.

sulphur- and molybdenum-extraction simulations respectively for various atom positions. As the atoms are moved away from their perfect-surface positions, the states start to resemble those of Figures 5.4b and 5.9b. By the time the extracted sulphur and molybdenum atoms reach their ideal tip–adsorbate separation, the gap-states are fully formed.

6.4.3 Electronic Potential *vs.* Tip–Sample Separation

In Section 6.4.1 it was determined that the close proximity of the tip to the sample has a large effect on the barrier against removal of atoms from the surface. The electron barrier should also be affected in the same way. Hirose & Tsukada (1994) have shown that the effective barrier for tunnelling electrons vanishes at small tip–sample separations. Figure 6.14 shows the self-consistent electronic potential in a line along the z axis through the tip and a Mo atom for different tip–sample separations. This potential is not, strictly speaking, that seen by tunnelling electrons as it does not include the image potential (unless the electrons tunnel infinitely quickly) and the DFT potential does not necessarily match the actual electronic potential (although it usually does a good job in bulk materials). However, the reduction in the height of the barrier with decreasing tip–sample separation will be similar to the reduction of the tunnelling barrier height under the same circumstances. In Figure 6.14 the barrier height has been reduced by 0.06au (1.6eV) by a tip movement of 1.25au (0.661Å).

Figure 6.15 shows the 'tail' of the total electronic charge density as a function of tip position relative to the surface Mo plane. As the tip approaches the surface, and the electronic barrier reduces, the electronic wavefunctions of the tip and surface start to overlap—the onset of bonding.

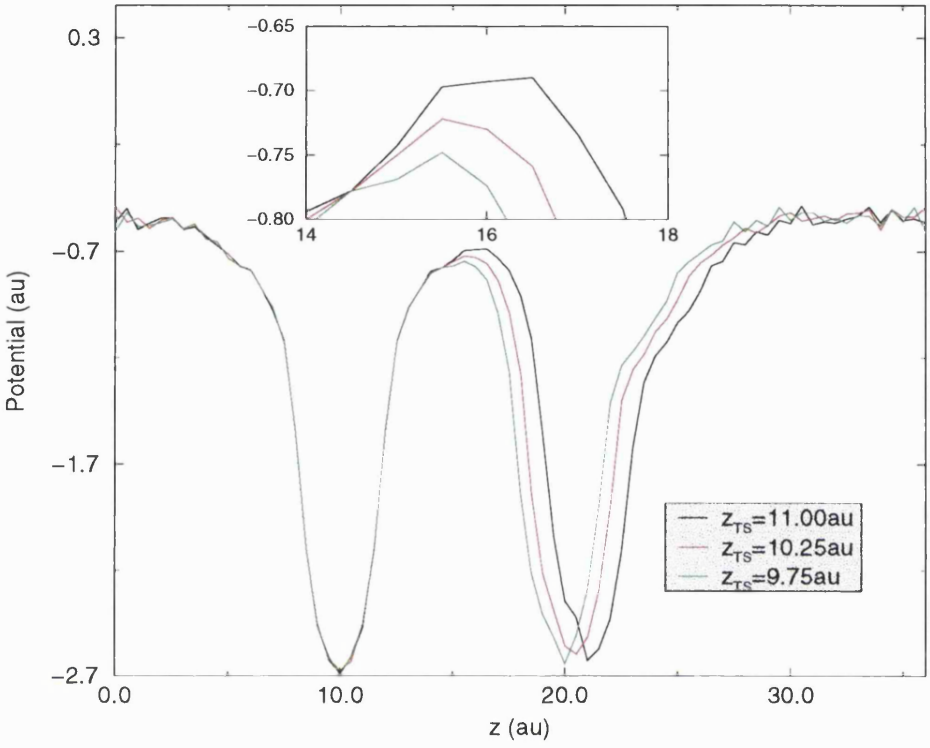

Figure 6.14: Self-consistent electronic potential in a vertical line through the tip apex and a Mo atom with the tip and surface in their separate equilibrium structures. The inset shows a magnified view of the barrier peak—the barrier height reduces by 0.06au (1.6eV) when the tip is moved 1.25au (0.661Å).

6.5 Field Effects in Atom Extraction

6.5.1 Effect on the Extraction Barrier

Section 6.4 reported PAW calculations on the extraction of molybdenum and sulphur atoms from the surface of MoS_2 and concluded that the atom extraction process cannot be explained purely in terms of the tip lowering the atom-extraction barrier. Those calculations included a tip, but did not take into account the fact that the tip is held a a different electrostatic potential to the surface. Extraction of sulphur from the MoS_2 surface, for example,

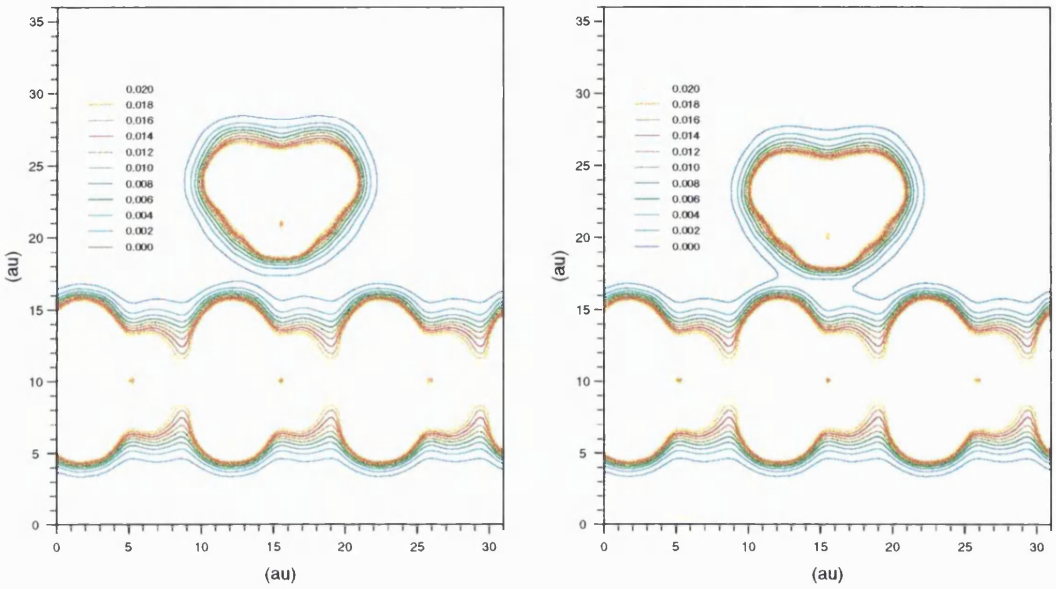

a) $z_{\text{tip}} = 11.0\text{au}$ b) $z_{\text{tip}} = 10.25\text{au}$

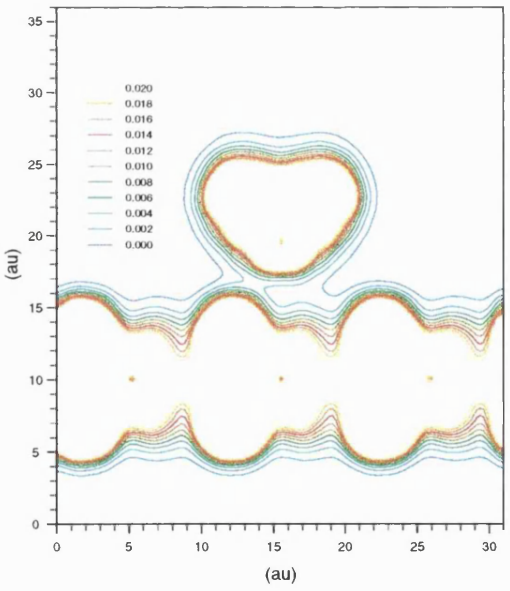

c) $z_{\text{tip}} = 9.75\text{au}$

Figure 6.15: Total charge density with the tip positioned over a Mo site showing the tail (lower values) of the density as a function of tip–sample separation (z_{tip} relative to Mo plane at 10au). As the tip is brought closer to the surface, the overlap of the tip and surface wavefunctions increases.

is typically carried out by pulsing the tip at -5V relative to the surface at a tip–sample separation less than or around 5Å.

The PAW method relies on periodic boundary conditions and is a purely static calculation as far as the electrons are concerned (*i.e.*, there can only be one Fermi level at equilibrium). It is therefore not possible to hold the chemical potential of the tip at a value different to that of the sample. However, it is possible to simulate the effect by applying a constant electric field to the system (Section 6.2). The system simulated here uses an applied field of 0.015au (0.77VÅ^{-1}) with the tip apex 11.0au (5.82Å) away from the surface molybdenum plane. Taking 8.0au (4.23Å, the tip–sulphur separation) as the tip–sample separation, the implied electrostatic potential difference between the tip and sample is -3.3V (tip negative with respect to surface).

Figure 6.16 shows the barriers against extraction of Mo and S atoms from the MoS_2 surface with an external applied field of 0.015au (0.77VÅ^{-1}) in a direction which would attract positive ions to the tip (tip apex at 11.0au). Also shown for comparison are the zero-field barriers previously shown in Figure 6.8. As before, the single point shows the effect that surface relaxation would have on the zero-field barrier maximum in the Mo-extraction barrier (*i.e.*, for adiabatic atom extraction, the barrier is removed). The figure shows that the application of an external electric field lowers the effective barrier against the extraction of both types of atoms from the surface. For the case of sulphur extraction, the barrier is lowered from 0.14au (3.81eV) without the field to 0.12au (3.26eV) with the field—a reduction of 14%. The effect on the molybdenum extraction barrier (ignoring the initial peak at $z = 2.8$au) is to lower it by 16% from 0.44au (12.0eV) without the field to 0.37au (10.1eV) with the field. (See Section 6.4.1 for assumptions about the 3D potential barrier and the effective barrier height).

Following Section 6.4.1, the temperatures required to extract S and Mo atoms from the surface can be estimated (Equation (6.3)). Table 6.3 shows

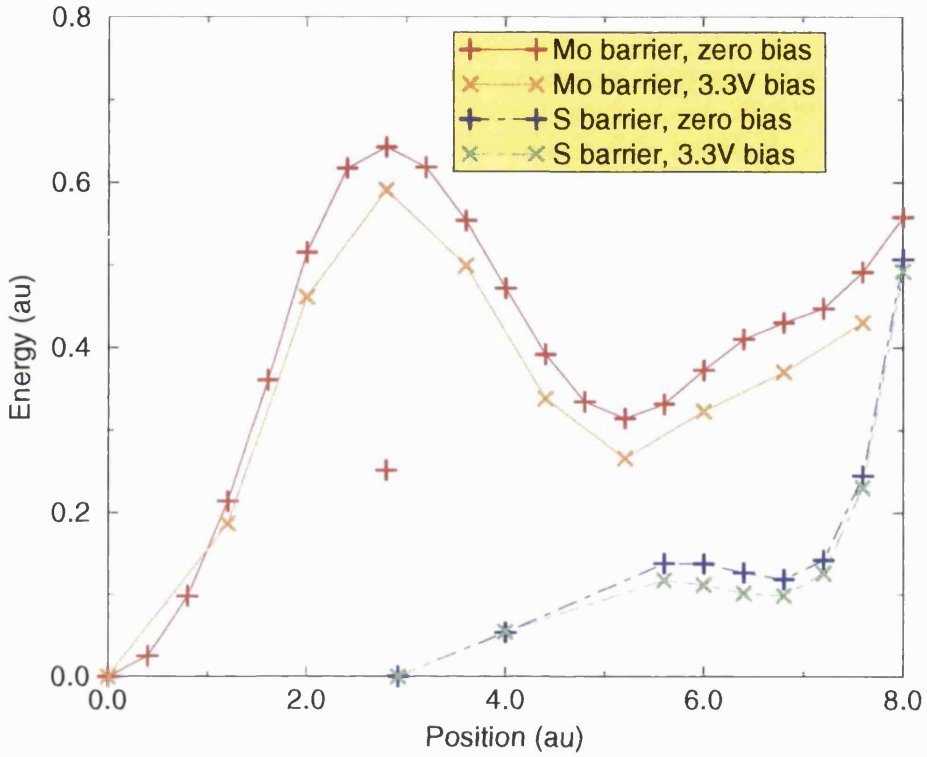

Figure 6.16: Barriers against extraction of single molybdenum and sulphur atom in the presence of a 0.015au ($0.77\text{V}\text{Å}^{-1}$) electric field (orange and green curves respectively) compared to the barriers without the field (red and blue curves). The single point shows the effect of surface relaxation on the zero-field molybdenum-extraction barrier peak at 2.8au. The tip apex is located at 11.0au.

Atom Type	Extraction Rate (s^{-1})	Required Surface Temperature (K)
S	10^3	1600
	1	1200
Mo	10^3	5100
	1	3900

Table 6.3: Local surface temperatures required to extract sulphur and molybdenum atoms from the MoS_2 surface for extraction rates of $10^3 s^{-1}$ and $1 s^{-1}$ in the presence of an electric field.

the calculated local surface temperatures required to extract S and Mo atoms at rates of $10^3 s^{-1}$ and $1 s^{-1}$ in the presence of a $0.77 V Å^{-1}$ electric field with the oscillation frequencies taken as those in the zero-field calculations (see Table 6.2). Although the electric field has reduced the local temperature required to remove atoms from the surface, the temperatures are still too high to be produced in a typical STM modification experiment. This implies that the atom-extraction mechanism relies on more than just the presence of the tip and the bias-induced electric field effects. Further discussion is deferred to Section 6.6.

6.5.2 Polarisation Charge and Electric Field

The reason behind the application of an electric field to the tip–sample system was to investigate the effects of the relative tip–sample bias on the barrier against atom extraction from the MoS_2 surface. The question is, does the system behave in the same way as a real STM tip and sample arrangement under an applied bias? The problem, as already mentioned, is that the PAW method does not allow for the existence of two distinct Fermi levels as in a real system where a net current flows. In the static calculation with a field, the tip and sample, which initially are at different electrostatic potentials owing to the electric field, will exchange charge in such a way that the Fermi levels equalise, removing the electrostatic (ES) potential difference.

This feature can be seen in the barriers shown in Figure 6.16: the energy separations between the curves with and without the field for both Mo and S extraction remain constant whilst the atom is within the 'vacuum' region. There are two possible explanations for this phenomenon: either the atom being extracted has no net charge (*cf.* Lang (1994) where the net charge on an Al adsorbate atom moved between two closely-spaced jellium electrodes attained a maximum net charge of 0.1e); or there is no electric field within

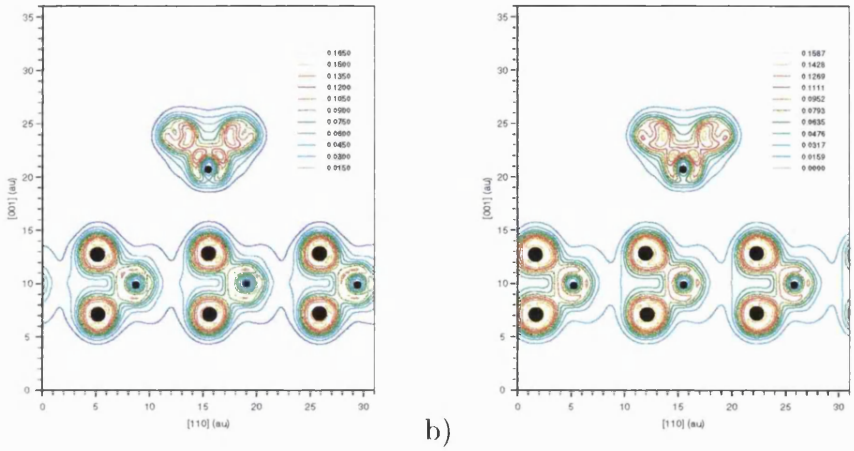

a) b)

Figure 6.17: Total charge density contours for a MoS_2 surface and a Mo cluster tip under the influence of a 0.015au ($0.77 V Å^{-1}$) electric field. a) Tip over sulphur site, and b) tip over a molybdenum site.

the gap region (or both may be true). Integrating the charge around the tip and sample (before atom extraction begins) shows that the tip has donated a further 0.8 electrons to the surface as a result of the applied field (to give a net charge transfer of 0.9e). Figure 6.17 shows the total charge density of the S and Mo extraction systems in the presence of the field with the tip and surface in their initial structures. Unsurprisingly, the charge transfer is not visible in the total charge density (there are 162 electrons in the surface and 30 in the tip before charge transfer).

Figures 6.18 and 6.19 show the polarisation charge densities (total charge of the system with the field minus the total charge of the system without the field) for the sulphur and molybdenum extraction systems respectively. As described above, the charge transfer has indeed cancelled the polarisation charge which would be present at the surface and tip apex. The effect of this depolarisation on the electric field is shown in Figure 6.20. This shows the difference in ES potentials for the tip–sample systems with and without a field for the tip placed above a sulphur and a molybdenum site. The external

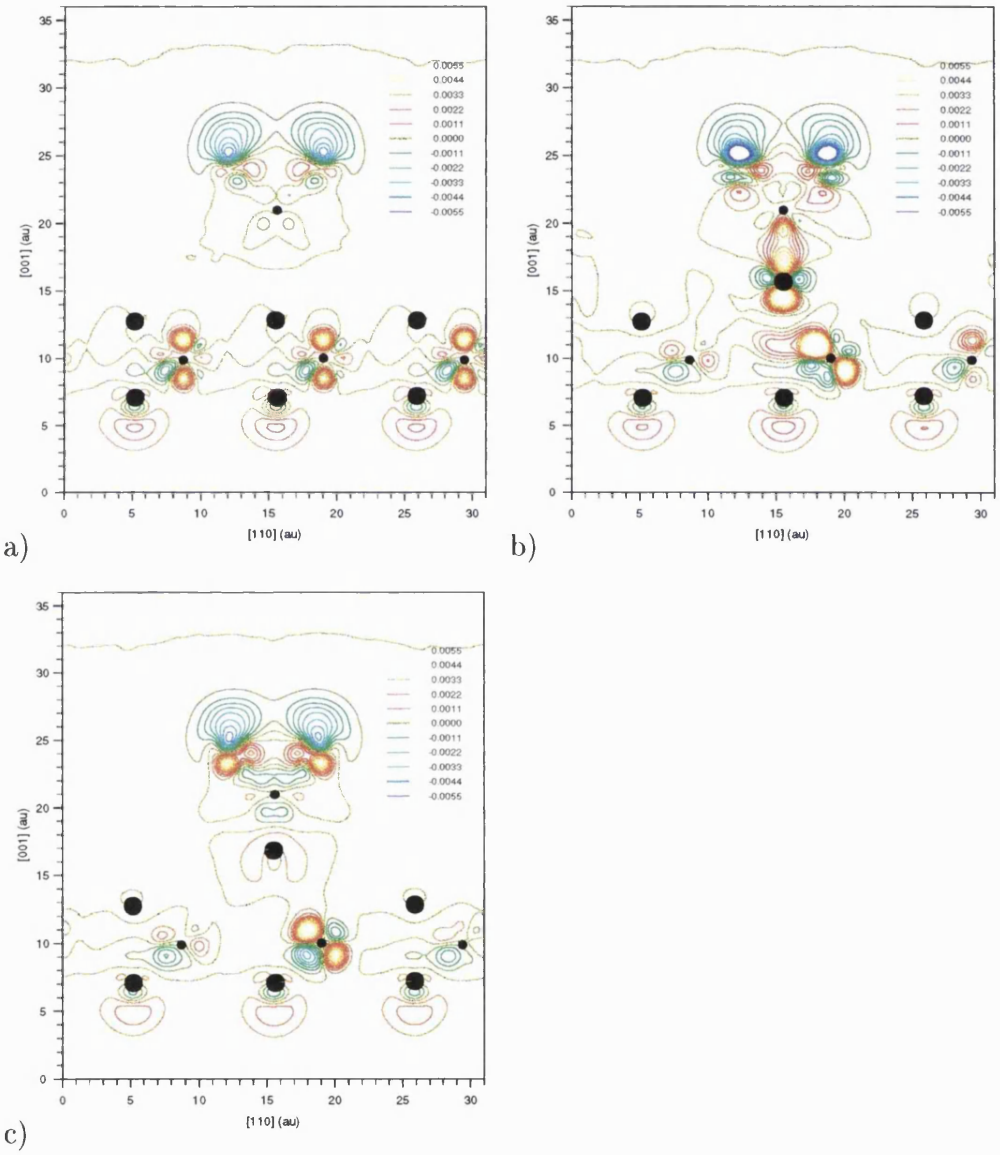

Figure 6.18: Polarisation charge density for MoS_2 in the presence of a Mo tip and an applied field of 0.015au ($0.77 V Å^{-1}$) at various stages as a sulphur atom is removed from the surface.

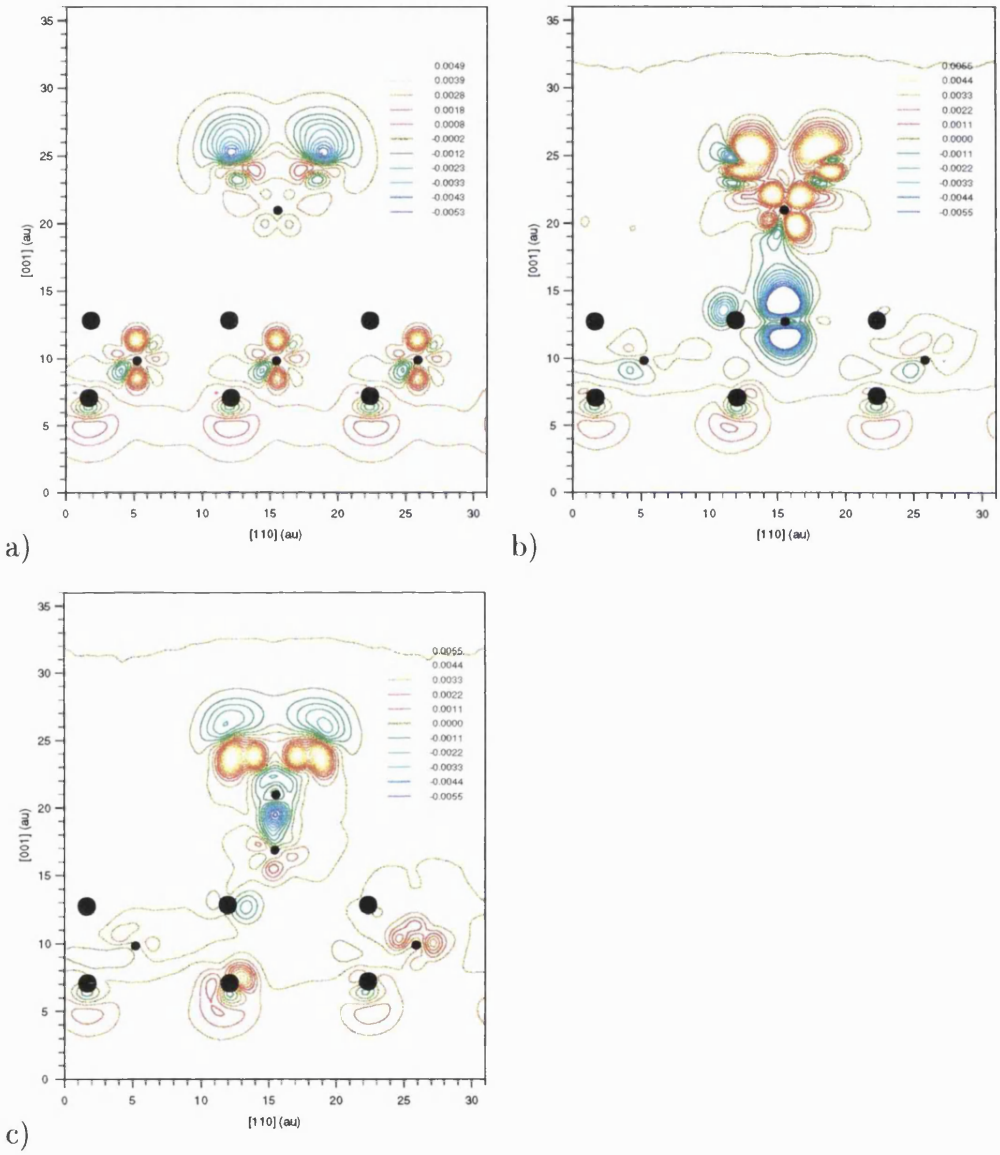

Figure 6.19: Polarisation charge density for MoS_2 in the presence of a Mo tip and an applied field of 0.015au ($0.77 V Å^{-1}$) at various stages as a molybdenum atom is removed from the surface.

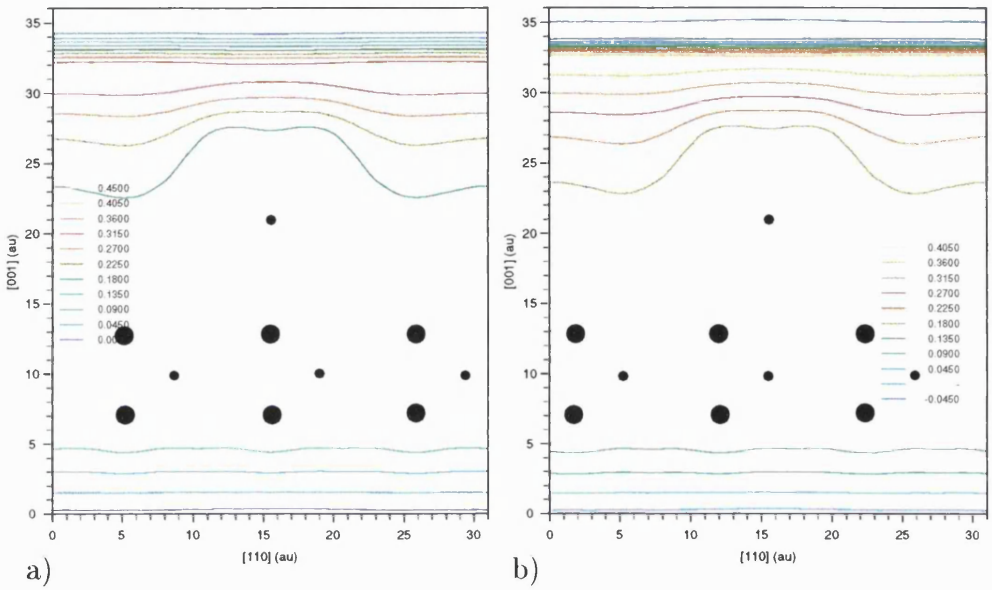

Figure 6.20: Electrostatic potential difference (see text for definition) for the MoS_2 surface in the presence of an electric field of 0.015au ($0.77 V Å^{-1}$) and an Mo tip located over a) a sulphur site and b) a molybdenum site. Field-induced charge transfer from the tip to the sample effectively screens the electric field in the vacuum gap region. The rapid change in potential at $z \approx 34$au is from the periodic cutoff (see Section 6.2).

electric field is totally screened within the tip and sample and in the vacuum gap between them—the system has responded to the field as a single, coupled system, not as two separate systems.

These charge-transfer and field-screening effects are the static-limit approximation to the existence of a tunnelling current (after all, a current is the result of an attempt to equalise the Fermi levels of two electrodes, made impossible by the fact that Fermi levels at the ends of the electrodes are pinned at different values). A naïve description of the processes occurring in a system maintaining a tunnelling current could go as shown in Figure 6.21. First, charge builds up on the tip apex and the surface polarises due to the different electrostatic potentials of the two electrodes. Next, the electron on the tip apex will tunnel

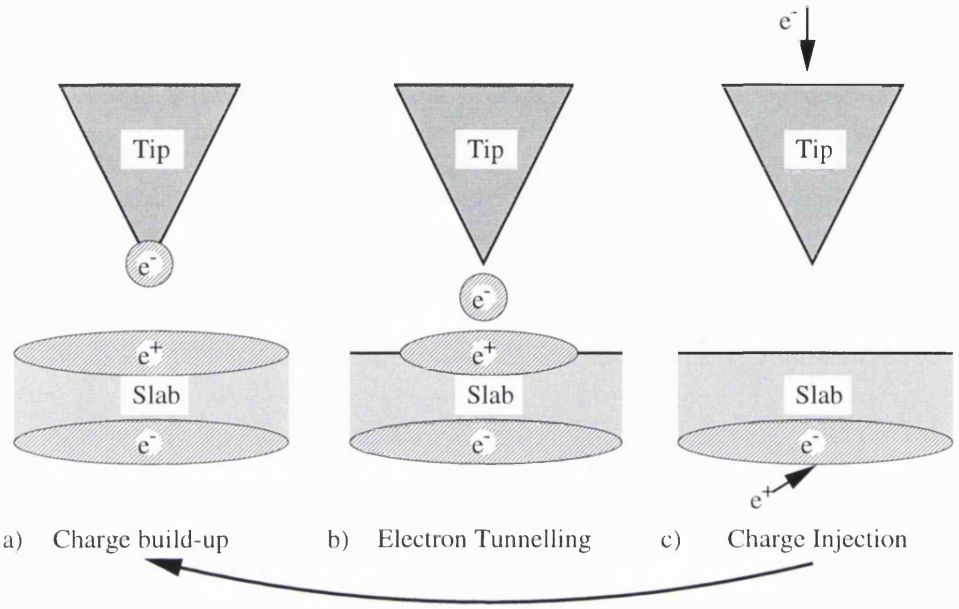

Figure 6.21: Naïve representation of the processes occurring in a dynamic tunnelling current situation. a) Charge builds up on the tip and the surface polarises; b) the electron on the tip tunnels through the barrier into the sample; c) the tunnelling electron reaches the surface and the polarisation in the gap (between the tip and upper sample surface) is reduced or removed. The process then repeats.

through the barrier, eventually reaching the surface, reducing the polarisation charge at the surface and tip apex. Then, another electron will be injected into the tip, and an electron extracted from the sample and the process will repeat. Since the tunnelling time ($\sim 10^{-16}$s) (Weisendanger 1994) and the time taken for the tip electrons to re-adjust (typically an inverse plasmon frequency, $\tau_{\text{plasmon}} \sim 10^{-16}$s) are much smaller than the time between tunnelling processes ($e/I \sim 10^{-10}$s) the system is likely to spend most of its time in the first state (*i.e.*, state (a) in Figure 6.21). So in a dynamic system there will, on average, be an electric field between the tip and sample. Since the shortest time-period in which an atom can transfer from one electrode to the other is of order the inverse phonon frequency, $\tau_{\text{phonon}} \sim 10^{-13}$s for phonons in most materials, the

effective barrier against atom transfer will be closer to the barrier in situation (a) then that of situation (c). So, a static calculation with one Fermi level will be sampling the wrong end of the tunnelling process. However, Appendix D.4 describes a set of calculations on the molybdenum-extraction barrier which show that the presence of an electric field affects the barrier in much the same way as surface charging without an external field. Furthermore, combining the effects of electric field and surface charging does not reduce the barrier much further. Hence the tip and sample calculations including the electric field presented in this chapter probably provide a reasonably accurate atom-extraction barrier in the presence of a tip and a bias.

6.6 Conclusions

In this chapter the barriers against the extraction of single sulphur and molybdenum atoms from the MoS_2 were calculated in the presence of a molybdenum tip. The effects that the application of an applied bias has on the barrier were simulated by adding a linear electric field to the total self-consistent PAW potential and re-relaxing the electrons from their zero-field distribution.

The barrier against extraction of sulphur from the MoS_2 surface was calculated with the tip apex at 10.0au (5.3Å) and 11.0au (5.8Å) from the surface molybdenum plane (7.0au and 8.0au respectively away from the top sulphur plane). With the tip at 11au there was a clear minimum in the barrier, associated with the sulphur atom being adsorbed on the tip, occurring at the previously-calculated equilibrium tip–sulphur separation. No such minimum was apparent with the tip at 10au, but separate calculations revealing the 3D shape of the barrier showed that there are minima off the chosen extraction line (*i.e.*, around the sides of the tip). The extraction barriers were found to be 0.11au (3.00eV) and 0.14au (3.81eV) with the tip at 10au and 11au respectively.

The molybdenum-extraction barrier showed a large peak as the Mo atom was squeezed through the surface sulphur layer. This peak is a result of the fact that atomic relaxation was not allowed in the calculations, and would be totally removed if the atom were extracted adiabatically. As for sulphur extraction with a tip at 10au, there was no minimum on the chosen extraction line. Again, though, the full 3D barrier was discovered to have minima around the side of the tip implying atom extraction is possible at this separation. The extraction barrier was found to be 0.44au (12.0eV). This barrier is significantly higher than that to extract an S atom from the surface. This is in line with the observations of Fuchs (1997) that, whilst it is fairly easy to extract chalcogen atoms from TX_2 surfaces, the metal atoms prove much more troublesome with the vacancies being formed with much lower probability and not always in the expected place (below the tip apex).

It was also found that the filled gap-states reported in Chapter 5 occurring as a result of the vacancy formation could be observed forming as the atoms were moved further away from their perfect surface positions. In this case, though, the 'gap-states' were not located at the top of the valence band since the eigenvalues of some of the states associated with the tip were higher in energy than the surface gap-states.

The electric field (magnitude $0.77\text{V}\text{Å}^{-1}$ directed from the surface towards the tip) was found to lower the barrier by 14% for extraction of sulphur and 16% for molybdenum extraction. These field-induced changes are relatively small when compared to the effect that the mere presence of the tip has on the extraction barrier. The evaporation energies of sulphur and molybdenum from the MoS_2 surface were calculated at 0.31au (8.45eV) and 0.83au (22.6eV) respectively—the barriers in the presence of the tip were around half of these values.

The way that a static calculation containing two different material slabs reacts to the addition of an external field is to transfer charge from one material

surface to the other. This is an effect similar to the contact potential which occurs when any two materials with differing work-functions are brought within close proximity of each other—it is the static limit of a tunnelling current. The effect on these calculations was to transfer 0.8 electrons (on top of the 0.1 electrons due to the contact potential) from the tip to the surface. The result of this is that the electric field within the two materials is completely screened. By considering the time-scales involved in the tunnelling current processes we have argued that a dynamic system will probably spend most of its time with the tip and surface polarised and an electric field between them. Things get conceptually much more difficult when considering the situation when the atom being extracted is halfway between the tip and sample—presumably current could flow more easily in this situation and the meaning of both 'electric field' and 'vacuum gap' become rather vague. Separate tip-free calculations on the MoS_2 surface charged with one electron (per 3×3 cell) and/or in the presence of the field show that the atom extraction barrier is affected in the same way (energetically speaking) whether the surface is charged or under a field. The conclusion is that the charge transfer resulting from the applied field in the static calculations has a similar effect on the extraction barrier as would the existence of a genuine electric field.

From the calculated barriers, and using a harmonic approximation to calculate the atomic vibration frequencies, the temperature required to extract atoms at a given rate can be estimated. The temperatures required for the extraction of sulphur and molybdenum atoms at the rates apparent in experiments ($\sim 10^3 s^{-1}$) were calculated to be over 1500K and 5000K respectively. The local surface heating resulting from the tunnelling current is not thought to be enough to produce these kinds of temperatures, and there is no evidence of local surface melting (which would surely occur at these temperatures).

The calculated atom-extraction barriers then, are much higher than those apparent in the experiments, leading to the conclusion that either an important

factor is missing from the calculations, or the tip–sample separation is too large. The tip–sample separation was estimated by Hosaka et al. (1995) to be less than or around 5Å, but it is possible that the actual separation may be less than this as a result of, for example, current-induced thermal expansion of the tip (Baskin et al. 1996). Reducing the tip–surface separation will certainly reduce the atom-transfer barrier, but at some point the potential well around the side of the tip may disappear. Perhaps the most important feature missing from the calculation is the lack of a dynamic tunnelling current. Inclusion of current (via a multi-Fermi-level simulation) would also inherently include the correct electric field and charge transfer between the tip and sample, and could in principle include effects such as the force on the atoms from the electron current. The current could also contribute to the reduction of the barrier by electron injection or excitation into anti-bonding states of the surface.

There are several groups using theory and experiment to study the role of the current in the atom-transfer process. Salam et al. (1994), for example, have studied the effect of coherent multiple excitations on the desorption of adsorbates on systems where there is a negative-ion resonance near the Fermi level, as is the case with Xe on Ni(110) (*cf. incoherent* excitations responsible for vibrational heating). They find that coherent effects are relatively important in the regime where the frequency of tunnelling events is smaller than that of the atomic vibrations (*i.e.*, the low current regime). Avouris et al. (1996) have also looked at the relative importance of coherent and incoherent excitations with regard to the selective removal of hydrogen from the H-passivated Si(100) surface. They demonstrated that pulsing at 6V or more (tip negative) with a tip–sample separation $\sim$ 16Å (implying an electric field $\sim$ 0.4VÅ^{-1}) resulted in a high probability of H desorption. The process involved in the desorption process is argued to be the excitation of Si–H σ bond electrons into the anti-bonding σ^* states, in which state the H–Si potential curve is repulsive. At lower electron energies (lower bias), H desorption was still possible,

albeit at reduced probability. Multiple incoherent excitations (*i.e.*, heating) are suspected to contribute in this case. The apparent switch in the regimes of importance is due to the position of the resonance with respect to the Fermi level.

Chapter 7

Conclusions

The *ab-initio* Projector Augmented Wave method has been used to study the STM imaging and method of formation of monatomic vacancies on the surfaces of the group VIB transition-metal dichalcogenides MoS_2 and $MoTe_2$. The PAW method is an all-electron electronic-structure technique based on density functional theory within the local density approximation and can cope with traditionally difficult elements such as the transition metals.

The bulk properties (bond lengths, band structure and charge density) of MoS_2 and $MoTe_2$ were calculated—the bond lengths were found to agree with experiment to within 1% and the band structure was found to be in good agreement with other simulations. The perfect surfaces of the two materials were simulated with a 3×3 single-slab cell and it was found that very little surface relaxation occurred relative to the bulk structure. The STM images of the surfaces showed peaks above the surface chalcogen sites as is now accepted to be the case under normal imaging conditions (although there is some evidence that the contrast may change at very small gap resistances).

Ultra High Vacuum STM experiments (Fuchs et al. 1992, Fuchs et al. 1993, Hosaka et al. 1995) have demonstrated that small features such as monatomic holes and trimer peaks may be formed on the surfaces of the transition-metal dichalcogenides by voltage-pulsing with the STM tip close to the surface. The

ease with which these vacancies can be produced varies. The monatomic holes are easily produced such that well-defined characters can be written to a surface, whereas the trimer defects are produced more erratically and with much lower probability. Monatomic vacancies on the MoS_2 and $MoTe_2$ surface were simulated for both metal and chalcogen vacancies in order to determine the nature of the defects observed in the STM experiments.

Introducing defects to a surface, such as substitutions or vacancies, will modify the local electronic structure, and hence may affect the STM image around the defect site. For both MoS_2 and $MoTe_2$, creation of the chalcogen vacancy was found to produce electronic states within the surface band-gap which were localised around the molybdenum atoms nearest the vacancy. The calculated STM images were qualitatively the same for both MoS_2 and $MoTe_2$, consisting of a monatomic hole at the site of the vacancy similar to those obtained in experiment after voltage pulsing on the surface. The MoS_2 image however, had a smaller bump in the central pit arising from the gap-states which was not seen in the $MoTe_2$ image.

Creation of metal vacancies on the surfaces was found to result in a trimer peak in the STM images of the surfaces similar to some of the defects observed in the experiments of Fuchs et al. (1992). In this case though, the energy at which the trimer could be observed differed for the two materials. For MoS_2 the localised states which produced the trimer were located below the Fermi level and therefore can be observed in a filled-state image, whereas for $MoTe_2$ the trimer is found in the empty-state image. In addition to this difference, the atomic structure of $MoTe_2$ around a metal vacancy is found to distort in a symmetry-lowering manner where there was almost no relaxation at all for the same vacancy on MoS_2. The source of this difference is found upon examination of the gap-states of the vacancy materials. The different ordering of these states in $MoTe_2$ relative to MoS_2 leaves the trimer-producing pair of doubly-degenerate states at the Fermi level, making $MoTe_2$ with a metal va-

cancy a Jahn–Teller system. Removal of the degeneracy upon relaxation (as will always occur in such situations) results in a lowering of the symmetry from D_{3h} to C_2 and the gap-states which produce the trimer feature end up above the Fermi level. So, while the trimer feature appears to be an inherent product of the vacancy defects on the VIB transition-metal dichalcogenides, the energy at which the feature can be observed is material dependent. In fact, whilst the MoS_2 results here agree qualitatively with tight-binding simulations carried out on the MoS_2 surface with a metal vacancy (Whangbo et al. 1995), there is disagreement over where in energy the feature will occur. However, since neither simulations included a very exact calculation of the STM image (both utilise the Tersoff-Hamann approximation and therefore completely ignore tip–sample interactions) the disagreement is perhaps a minor point, but demonstrates one of the difficulties of dealing with such systems.

Despite the fact that experimental groups are now regularly modifying surfaces by selectively extracting single atoms, the actual mechanisms behind the process are not well understood. The process is likely to occur via a combination of chemical, electric field, current, and heating effects, and the PAW method (with modifications by Ness & Fisher (1997a)) is well-suited to examine the effects of the tip–surface interaction and the electric field.

Single Mo- and S-atom extraction from the MoS_2 surface in the presence of a 5-atom cluster Mo tip, and the effect of an electric field of $0.77\text{V}\text{Å}^{-1}$, were studied. It was found that the presence of the tip reduced the barrier against extracting both Mo and S atoms by a factor of two relative to the zero-field, no-tip barrier (*i.e.*, the evaporation energies). The addition of the electric field perpendicular to the surface, set up to attract positive ions to the tip, was found to reduce the barrier by a further $\sim 15\%$. However, the barrier heights are still rather high, implying local surface temperatures of order 1500K and 5000K for the extraction of single S and Mo atoms respectively at a rate of 10^3s^{-1}. It is often argued that the local surface heating effects in the STM

are unlikely to raise the temperature by more than around a hundred degrees implying that there is more to the extraction process (at least for MoS_2) than the effects of the tip and the field.

Another interesting aspect of the atom-extraction simulations is the reaction of the system to the electric field. The PAW technique, being a plane-wave based, periodic-cell technique, does not allow for travelling-wave solutions to the Schrödinger equation, and hence ignores the tunnelling current and cannot maintain a system with two Fermi levels (as exists in the real situation). The result is that upon application of a bias, charge transfers from the tip to the surface, removing the polarisation and the electric field in the gap region—the tip and surface react to the field as a single coupled system. This behaviour is the static limit of a tunnelling current, which is a result of an attempt by two systems to equalise Fermi levels. Energetically speaking, it is found that the charge transfer affects the atom-extraction barrier in a similar way to the existence of an electric field, so the PAW simulations are deemed to be a good representation of the field and tip effects. The next generation of simulations regarding atom-extraction with the STM, however, will need to include the current and bias effects explicitly in order to make accurate predictions as to the barriers against surface modification.

There are several possibilities for expanding on the work presented in this thesis. Firstly, with regard to the imaging of the vacancies on the transition-metal dichalcogenides, the contrast of the observed features may be changed if the occupation of the gap-states are changed. A full image calculation including the tip and current effects should reveal the correct image contrast for a given bias. Inclusion of a finite current in the atom-extraction calculations is also an important step. Calculations of this type have been done by, *e.g.*, Hirose & Tsukada (1994), but the formalism would need to be expanded to deal with non-local pseudopotentials in order to treat materials such as the transition-metal dichalcogenides. Inelastic effects have also been shown by

others to be important in certain circumstances, where either surface heating, or long-lived resonance states can increase the likelihood of atom extraction—a qualitative description of the energy-transfer between the ions and electrons would be a useful addition to the calculations. Atomic-relaxation is another feature missing from the atom-extraction calculations. It would be interesting to confirm the partially-justified assumptions that this would not significantly affect the atom-extraction barrier height, and to produce the correct atom-extraction path. It would also be interesting to see how the $MoTe_2$ surface behaves as a metal atom is removed—at what point does the Jahn–Teller distortion of the surface occur, or does the presence of the tip and the associated contact potential and bias mean that the degeneracy at the Fermi level never arises when the tip is near the surface? One further possible addition to the calculations is the force on the ions resulting from the flow of electrons itself—the 'electromigration' force. The effect, if any, this process has on the atom-extraction process is unknown and it would be interesting to see whether (and under what conditions) it is important.

In conclusion, the studies presented in this thesis, while lacking many features of real STM experiments, have helped clarify the nature of defects obseved and created on the TX_2 surfaces and have provided insight into some of the mechanisms which contribute to the production of such defects.

Appendix A

Figure Conventions

A.1 STM Images

All calculated STM images shown in this thesis are obtained via the Tersoff–Hamann method (see Section 3.2) using Equation (3.12) assuming that the PAW (Section 2.7) eigenvalues represent the one-electron eigenvalues of the real system.

In almost all cases, the simulated applied bias was 0.8V (tip positive) such that it is the filled surface states which are imaged; the exception is Figure 5.10 where the bias is reversed. A Lorentzian broadening factor of $\eta = 0.6$eV was used throughout.

In STM images of surfaces with vacancies, the vacancy is always located at the centre of the image. STM scan-lines are always taken in a direction along the metal-chalcogen bond, across the vacancy site (where relevant).

A.2 Charge Density Slices

Unless stated otherwise, the 2D charge-density contours shown are taken in a vertical plane diagonally across the simulation cell. With the unit cell taken to be as in Figure 4.1, this corresponds to the $(\bar{2}10)$ plane (Figures 4.1b and

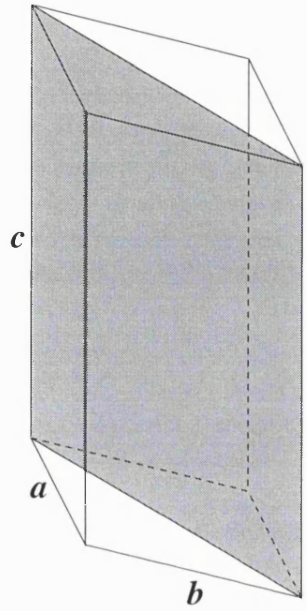

Figure A.1: Schematic representation of the slice used throughout this thesis (unless otherwise stated) to show charge densities. The slice is taken with one axis diagonally across the full simulation cell and the other in the c direction (along the z axis). The plane is also chosen to bisect any important features of the simulation, such as vacancy sites, displaced atoms, and where relevant, the tip apex.

d), with the x- and y-axes of the plane taken in the [010] and [001] directions respectively (there are, however, two other equivalent choices provided the cell symmetry is maintained). Figure A.1 shows a schematic representation of an equivalent slice in the simulation cell. The slice passes through the metal-chalcogen bonds, any vacancy sites or displaced atoms, and, where applicable, the apex of the tip. The slice stretches across the entire cell so that the left and right edges are equivalent. Metal and chalcogen atoms in the plane of the slice are represented by small and large closed circles respectively. Where present, the figure legends show charge per unit volume in atomic units (*i.e.*, e/a_o^3)—they are intended only to indicate the relative magnitudes of the densities between different images in the same chapter.

Although the PAW method is an All-Electron (AE) method, the charges

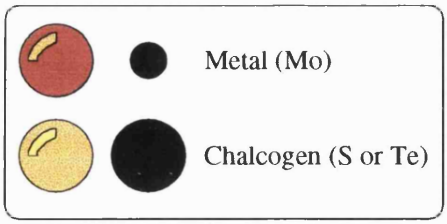

Figure A.2: The symbols used to represent atoms in the figures in this thesis.

displayed are obtained from the pseudo-charge only. Including the AE charge would just produce a spike of density at the atomic centres and, aside from the advantages of such a wavefunction representation, is of little interest to this work.

A.3 Atomic Representation

Throughout this thesis, metal atoms are represented by red spheres, or small black closed circles, and chalcogen atoms are represented by yellow spheres, or large black circles regardless of the specific type of metal or chalcogen (see Figure A.2).

Appendix B

The Jahn–Teller Effect and the D_{3h} Point-Symmetry Group

In Chapter 5 the molybdenum vacancy on the $MoTe_2$ surface was found to be a Jahn–Teller system. The Jahn–Teller effect occurs in almost any situation where there is an orbital degeneracy at the Fermi level (the sole exceptions being linear molecules, and the Kramers degeneracy), and is a result of the fact that for any degenerate set of orbitals there will be an associated lattice distortion which can remove the degeneracy. Since in all Jahn–Teller systems the leading term in the electron-phonon coupling is linear, whereas the ground-state energy is quadratic in the atomic coordinates, it is possible to lower the energy of a system with an orbital degeneracy at the Fermi level by lowering the symmetry of the lattice.

The Hamiltonian of a doubly degenerate electronic state interacting with a single mode of lattice distortion can be expressed as

$$H = -\frac{1}{2}\frac{\partial^2}{\partial Q^2} + \frac{1}{2}Q^2 + K \begin{pmatrix} -Q & 0 \\ 0 & Q \end{pmatrix}, \tag{B.1}$$

where Q is the normal-mode coordinate of the lattice distortion, and K rep-

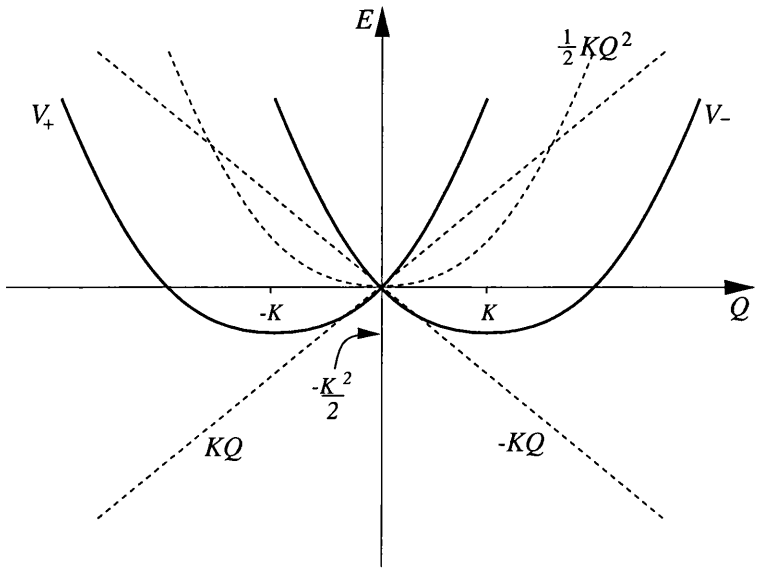

Figure B.1: The potential of a doubly degenerate pair of electronic orbitals interacting with a single lattice-distortion mode: $V_\pm = \frac{1}{2}Q^2 \pm KQ$ where Q is the normal-mode coordinate and K the Jahn–Teller coupling. The dotted lines represent the components of the potential $V_\pm$, and the solid lines show the actual potentials V_+ and V_-.

resents the the coupling between the electronic states and the normal mode. When operating on a wavefunction described by only one of the degenerate pair Equation (B.1) can be written as

$$H = -\frac{1}{2}\frac{\partial^2}{\partial Q^2} + \frac{1}{2}Q^2 \pm KQ, \tag{B.2}$$

Equation (B.2) is the Hamiltonian of a pair of harmonic oscillators with minima of $E = -\frac{1}{2}K^2$ at $Q = \pm K$. Figure B.1 shows a schematic of the potential. For more complicated situations such as those in a crystal lattice, the basic result is the same: the potential surface will have minima away from the origin in normal-mode-coordinate space (but not necessarily along the axis of a single mode) and the system will lower its total energy by distorting the lattice.

The symmetry group of interest to this thesis is that about a metal vacancy

D_{3h}	E	$2C_3$	$3C_2$	σ_h	$2S_3$	$3\sigma_v$
A_1'	1	1	1	1	1	1
A_2'	1	1	-1	1	1	-1
E'	2	-1	0	2	-1	0
A_1''	1	1	1	-1	-1	-1
A_2''	1	1	-1	-1	-1	1
E''	2	-1	0	-2	1	0

Table B.1: Character table of the D_{3h} point-symmetry group. Schönflies symbols are used to denote the symmetry operations (Leech & Newman 1969).

D_{3h}	C_{3h}	C_{3v}	C_{2v} $\sigma_h \to \sigma_v$	C_s σ_h	C_s σ_v
A_1'	A'	A_1	A_1	A'	A'
A_2'	A'	A_2	B_2	A'	A''
E'	E'	E	$A_1 + B_2$	$2A'$	$A' + A''$
A_1''	A''	A_2	A_2	A''	A''
A_2''	A''	A_1	B_1	A''	A'
E''	E''	E	$A_2 + B_1$	$2A''$	$A' + A''$

Table B.2: The behaviour of the irreducible representations of the D_{3h} group as the symmetry is reduced. The $\sigma_h \to \sigma_v$ denotes a change in the plane of the reflection symmetry when going from C_{3v} to C_{2v}.

in a single slab of $MoTe_2$, *i.e.*, the D_{3h} point-symmetry group. Table B.1 shows the D_{3h} character table. Along the top of the table are the Schönflies symbols representing the symmetry operations under which the symmetric object would be unchanged, and down the left are the irreducible representations of the group (which can be used to classify the symmetry of either the electronic states or the atomic distortions). In this notation the E representations are doubly degenerate, the others are non-degenerate. This table shows, for example, that the A_1' representation transforms exactly into itself under all D_{3h} operations—this representation is called the identity representation for this reason; a more

complicated example is that of the A_1'' representation which transforms into itself under the E, $2C_3$ and $3C_2$ operations, but transforms into *minus* itself under all other operations in the group. For a detailed explanation of group theory and its uses see, *e.g.*, Leech & Newman (1969). This table is used to calculate the symmetry of various states from PAW calculations, where the transformation of the overlap of the projector functions (related to spherical harmonics) with the wavefunctions provides the necessary information.

In Chapter 5 the Jahn–Teller distortion about the Mo vacancy in $MoTe_2$ is a result of a double degeneracy in an orbital pair which transform like the E''. Table B.2 shows how the irreducible representations of the D_{3h} group are affected by a reduction in symmetry. This table is used in Section 5.3.2 to show that the D_{3h} point-symmetry must be reduced to at least C_{2v} in order to remove the E'' orbital degeneracy at the Fermi level.

Appendix C

Mo-Cluster Tip Calculations

C.1 Tip Only Calculations

C.1.1 Tip Geometry

The STM tip used in the atom-extraction simulations consisted of a five-atom cluster of molybdenum atoms. Bulk molybdenum forms in the body-centre-cubic (bcc) structure, with a lattice parameter of 3.147Å. The tip structure used in the atom-extraction simulations was a pyramid of five Mo atoms, initially in the bcc structure shown in Figure C.1a, with the geometry relaxed under the sole constraint that the four base atoms remain in a plane. Figure C.1b shows the final structure used in all calculations involving a tip.

C.1.2 Electric Field with Tip

The tip is a metallic object and therefore no electric field can exist within it. Figure C.2 shows the difference in electrostatic potential between the tip systems with and without the field, and the polarisation charge on the tip for an applied field of 0.0015au (0.077VÅ^{-1}). Figure C.3 shows the same electrostatic potential difference along a line through the tip apex in the c direction. As expected, the electric field has been screened within the tip by the polarisation

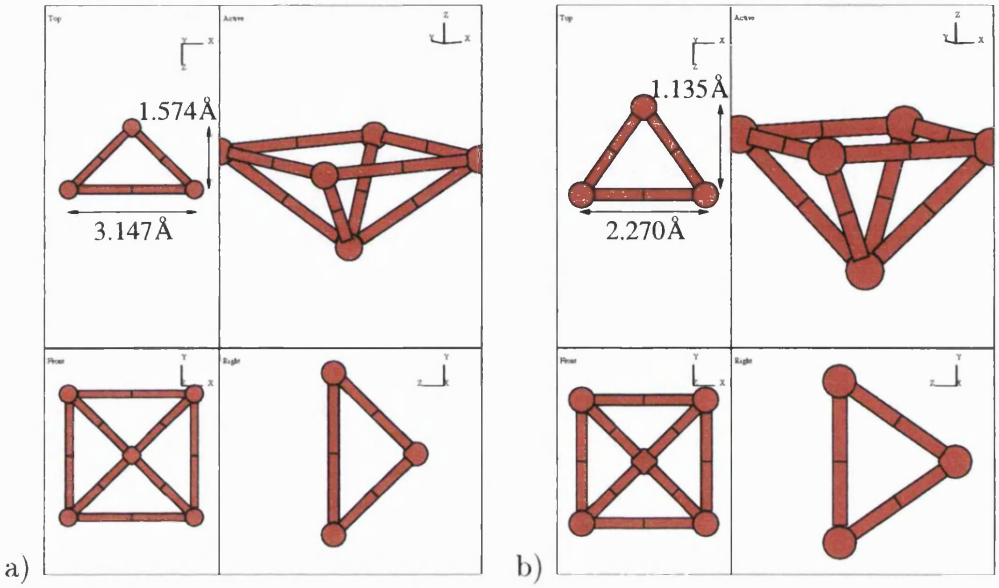

Figure C.1: a) the initial (bulk bcc) and b) the relaxed geometry of the Mo cluster tip. The latter structure was used in all simulations involving a tip.

of the surface. The net field in the vacuum region is 0.002au ($0.103\text{V}\text{Å}^{-1}$).

The field used above is ten times smaller than that used in the main tip–sample simulations. This field was chosen to illustrate the correct behaviour of the tip and field within the PAW technique. When the field is increased to 0.015au (the value used for the tip–sample calculations) electrons 'leak' from the tip to the artificial well at the cutoff boundary, screening the field below the tip—the equivalent of field emission in a static calculation.

C.2 Calculations of the Tip and Adsorbates

C.2.1 Equilibrium Tip–Adsorbate Separation

The equilibrium separations between the Mo cluster tip (Appendix C) and single adsorbed molybdenum and sulphur atoms were calculated. The simulation cell used was the same as that for the atom-extraction simulations

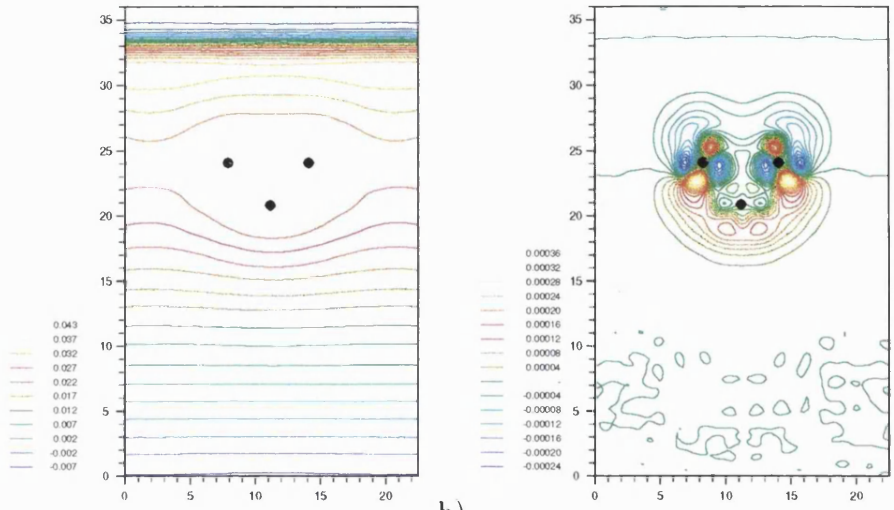

Figure C.2: a) Electrostatic potential difference (between the system with an external field of 0.0015au ($0.077\text{V}\text{Å}^{-1}$) and zero field) for a Mo-cluster tip in a plane through the tip apex and two diagonally opposite base atoms. b) The polarisation charge density of the tip under an applied bias of 0.0015au in the same plane as (a). The results of this quantum-mechanical simulation are those expected from a simple classical view of a conductor in an electric field, *i.e.*, polarisation of the surface with total screening of the field within the metal. Closed black circles represent the Mo atoms in the plane.

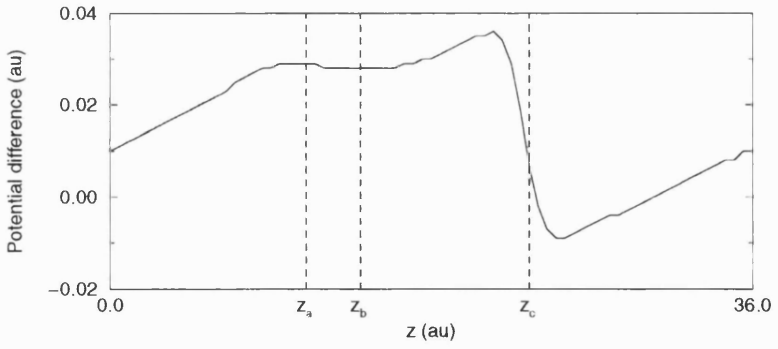

Figure C.3: Electrostatic potential difference in a line through the tip apex in the c direction for an applied field of 0.0015au ($0.077\text{V}\text{Å}^{-1}$) (See Figure C.2 for a definition of potential difference). z_a and z_b represent the z-coordinate of the tip apex (11.0au) and base (14.04au)respectively; z_c is the applied field cutoff (23.5au) (see Section 6.2). The effective field in the vacuum region is 0.002au ($1.03\text{V}\text{Å}^{-1}$).

Adsorbate	d_{TX} (au (Å))	E_B (au (eV))
sulphur	4.19 (2.22)	0.185 (5.04)
molybdenum	4.02 (2.12)	0.168 (4.58)

Table C.1: Equilibrium tip–adsorbate separations (d_{TX}) and binding energies (E_B) for S and Mo adsorbed on the Mo cluster tip. These values are calculated assuming the tip is held rigid and the adsorbate is constrained to move along a line through the tip apex perpendicular to the tip.

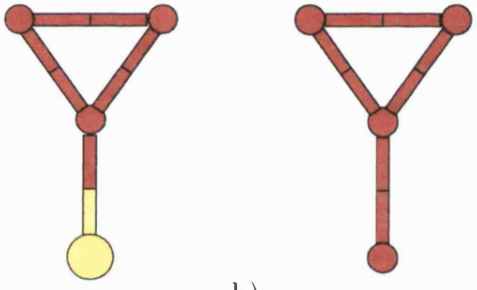

a) b)

Figure C.4: Equilibrium tip–adsorbate structure for adsorbed a) sulphur and b) molybdenum assuming the tip is held rigid and the adsorbate is constrained to move along a line through the tip apex perpendicular to the tip.

(see Section 6.3), but containing only the five tip atoms plus the adsorbate. A planewave cutoff of 15Ry was used for the wavefunctions which were calculated only at the Γ-point. To maintain relevance to the atom-extraction simulations (Chapter 6), the adsorbed atoms were constrained to a line through the tip apex in the c direction and the tip was held rigid.

Table C.1 shows the equilibrium tip–adsorbate separations and the tip–adsorbate binding energies for sulphur and molybdenum extraction; the atomic structures are shown in Figure C.4. The binding energies are calculated according to

$$E_B = E_T + E_X - E_{TX} \tag{C.1}$$

Adsorbate	ΔE (au (eV))	Δr (au (Å))
Sulphur	-7.0×10^{-5} (-1.9×10^{-3})	0.42 (0.22)
Molybdenum	-5.3×10^{-3} (-1.4×10^{-1})	1.2 (0.64)

Table C.2: Relaxation energy (ΔE) and motion (Δr) of S and Mo atoms adsorbed on a Mo tip and allowed to relax in a plane perpendicular to the tip through the equilibrium tip–adsorbate position.

where E_{B} is the binding energy, E_{T} is the total energy of the tip, E_{X} is the total energy of the adsorbate atom alone, and E_{TX} is the tip–adsorbate total energy (all for the same cell and planewave cutoff).

C.2.2 3D Structure of the Tip–Adsorbate Potential

The atom-extraction simulations reported in Chapter 6 assumed that the atom being extracted moved along a straight line towards the tip apex (*i.e.*, along the z direction). In reality, the lowest energy path may be more complicated than this, particularly as the extracted atom gets close to the tip. This appendix details some calculations intended to reveal the important features of the three-dimensional atom-extraction barrier for use in the arguments of Chapter 6.

The first calculations involved the rigid tip (Appendix C.1.1) and either a sulphur or molybdenum adsorbate, in the equilibrium structure with the adsorbate constrained to line through the apex perpendicular to the tip (Appendix C.2.1). The adsorbate atom was then allowed to relax in the plane perpendicular to the tip through the equilibrium adsorbate position. Table C.2 shows the relaxation energy (ΔE) and the distance which the atom moved in the plane (Δr). The very small relaxation energies and atom movements show that the extracted atoms do indeed follow a (nearly) straight line along the z-axis until they reach their equilibrium tip–adsorbate positions.

Despite the fact that the extracted atoms approach the tip apex almost

Adsorbate	ΔE (au (eV))
Sulphur	-0.086 (-2.34)
Molybdenum	-0.147 (-4.00)

Table C.3: Energy change after allowing tip–adsorbed S and Mo atoms to relax fully from their equilibrium apex positions.

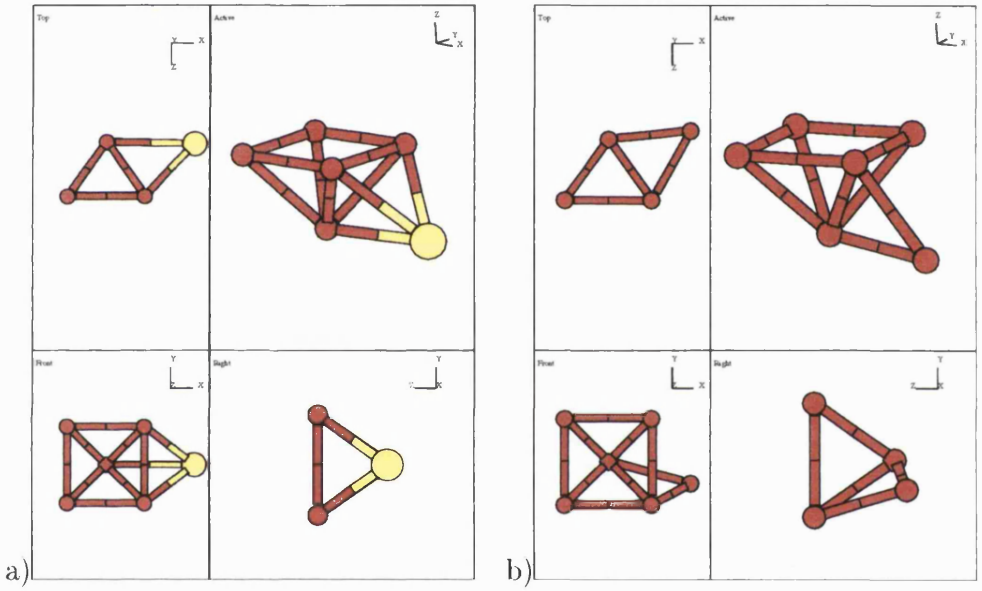

Figure C.5: Preferred structure of a) sulphur and b) molybdenum atoms adsorbed on a fixed molybdenum-cluster tip.

directly up to the equilibrium tip–adsorbate separations, it seems unlikely that the adsorbed atom would stay balancing on the tip apex were it allowed to relax around the tip. The second set of calculations allow full relaxation of the adsorbate around the fixed tip. Table C.3 shows the relaxation energies of the adsorbates around the tip with respect to the equilibrium apex-position energy. Figure C.5 shows the final tip–adsorbate structures for both sulphur and molybdenum adsorbates. The relaxation here is much larger than that seen for the relaxation in the plane, leading to the general conclusion that extracted atoms approach the tip in a straight vertical line up to roughly the

equilibrium tip–adsorbate separation, at which point the adsorbates will relax around the tip into a more stable, lower-energy position.

Appendix D

Extra MoS_2 Slab Calculations

D.1 Surface Polarisation and Effective Electric field

Application of an electric field to a slab of dielectric material will cause a rearrangement of electrons in the material to reduce the effect of the field within it. This is equivalent to setting up an electric field within the slab which opposes the applied field. In general, the electric field within the slab, $\mathcal{E}_{\mathrm{s}}$, is related to the electric field in the vacuum, $\mathcal{E}_{\mathrm{v}}$ by

$$\mathcal{E}_{\mathrm{v}} = \epsilon_r \mathcal{E}_{\mathrm{s}}, \tag{D.1}$$

where ϵ_r is the relative permittivity of the slab material. In periodic boundary conditions, the electric field is included by adding a sawtooth potential to the total potential (Ness & Fisher (1997a) and Section 6.2)—this imposes a fixed potential drop across the simulation cell, regardless of the polarisation of the surface. As a result of this, the field in the vacuum is also dependent on the

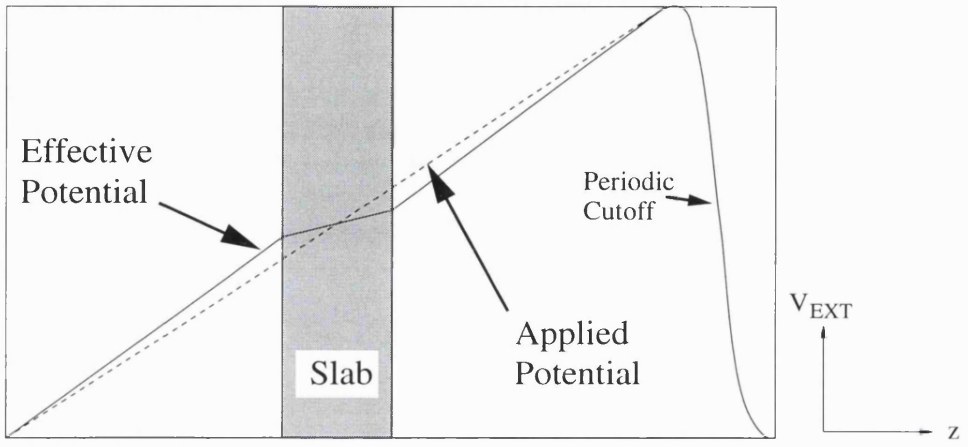

Figure D.1: In a supercell geometry, the effective external field will be larger than the applied external field. The magnitude of the difference depends on the polarisability (or the relative permittivity) of the slab (Ness & Fisher 1997a).

permittivity of the surface. Equation (D.1) can be expanded into

$$\mathcal{E}_{\mathrm{APP}} + \mathcal{E}_{\mathrm{v}}^{\mathrm{ind}} = \epsilon_r(\mathcal{E}_{\mathrm{APP}} + \mathcal{E}_{\mathrm{s}}^{\mathrm{ind}}), \tag{D.2}$$

where $\mathcal{E}_{\mathrm{s}}^{\mathrm{ind}}$ and $\mathcal{E}_{\mathrm{v}}^{\mathrm{ind}}$ are the induced fields in the surface and vacuum regions respectively, which are related by

$$d_{\mathrm{s}}\mathcal{E}_{\mathrm{s}}^{\mathrm{ind}} + d_{\mathrm{v}}\mathcal{E}_{\mathrm{v}}^{\mathrm{ind}} = 0, \tag{D.3}$$

where d_{s} and d_{v} are the slab and vacuum sizes respectively. In summary, the addition of a external field to the simulation induces an opposing field within the slab which then induces an increase in the applied field (and so-on to self-consistency); Figure D.1 shows schematically how the surface polarisation increases the effective applied field.

Figure D.2 shows the polarisation charge density and electrostatic potentials for a 3×3-cell slab of MoS_2 with and without an external applied field of 0.015au ($0.77\mathrm{V\AA}^{-1}$); also shown are the applied potential (blue curve) and the

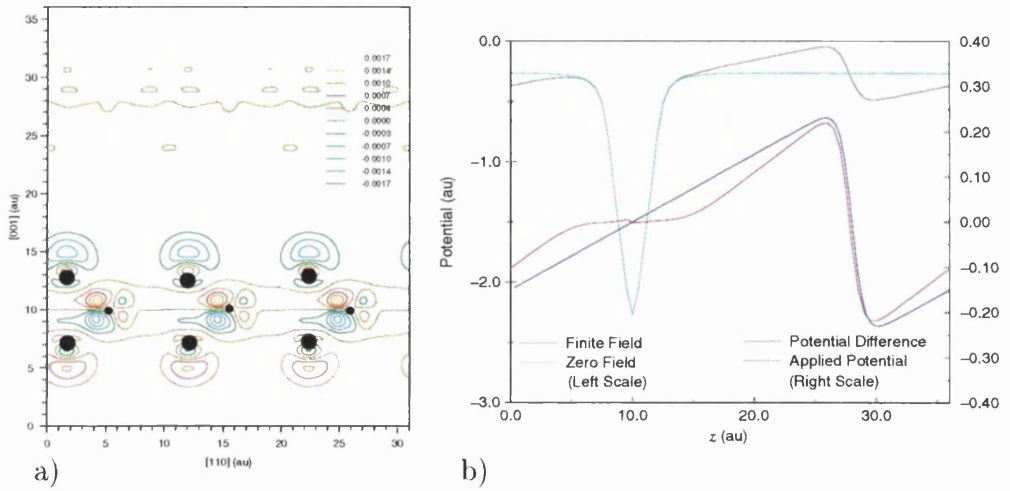

Figure D.2: The MoS_2 surface in the presence of an external applied field of 0.015au ($0.77V\text{Å}^{-1}$). a) Polarisation charge density in a vertical slice through the Mo–S bonds. b) Electrostatic potentials for the surface with and without the external field, the difference between the two, and the actual applied potential in a line through a Mo atom in the c direction. The periodic boundary conditions combined with the surface polarisation result in an effective field in the vacuum gap of 0.021au ($1.08V\text{Å}^{-1}$).

electrostatic potential difference between the systems with and without the field (red curve). The effect described above can be seen occurring here—from the gradient of the potential in the vacuum region (red curve), the effective applied field is 0.021au ($1.08V\text{Å}^{-1}$).

D.2 Evaporation of Mo and S Atoms from the MoS_2 Surface

Chapter 6 is concerned with the extraction of single sulphur and molybdenum atoms from the MoS_2 surface in the presence of a tip. It is useful to be able to compare the calculated barrier heights against atom transfer from the surface to the tip with the energy required to remove an atom from the surface without

Species	E^{evap} (au (eV))
Sulphur	0.31 (8.45)
Molybdenum	0.83 (22.6)

Table D.1: Evaporation energy (E^{evap}) for sulphur and molybdenum from the MoS_2 surface.

a tip (the evaporation energy). The evaporation energy $E_{\text{X}}^{\text{evap}}$ for the atomic species X (sulphur or molybdenum) can be calculated from

$$E_{\text{X}}^{\text{evap}} = E_{\text{X}} + E_{\text{X}}^{\text{vac}} - E^{\text{surf}}, \tag{D.4}$$

where E_{X} is the total energy of a lone atom of species X, $E_{\text{X}}^{\text{vac}}$ is the total energy of the surface with a species X vacancy, and E^{surf} is the total energy of the perfect surface. All calculations were carried out in the same cell with a 15Ry planewave cutoff for the electrons, and a 3×3 single-slab surface where required. The calculated evaporation energies are listed in Table D.1 (strictly speaking, these are the evaporation energies per atom to remove one atom per 3×3 unit-cell area) .

D.3 Surface Relaxation During Atom Extraction

The calculations described in Chapter 6, where the barriers against extracting single atoms from the MoS_2 surface were calculated, did not include any atomic relaxation. Whilst this is justified when the extracted atom is clear of the surface (the surface reconstruction around vacancies is extremely small on MoS_2—see Chapter 5), it will introduce errors as the atoms are actually in the process of being extracted. The barrier calculated excluding atomic relaxation

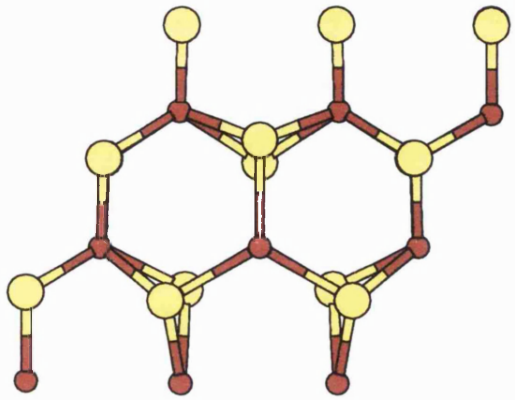

Figure D.3: Relaxed structure for the MoS_2 surface with one of the Mo atoms displaced by 2.8au in the c direction.

is, in effect, an upper bound on the actual barrier.

Atomic relaxation effects are likely to be large for the case of molybdenum extraction, where the Mo atom has to be 'squeezed' through the upper sulphur layer. This effect will be largest at the point where the Mo atom is actually in the same plane as the surface S atoms. Calculations were carried out on the 3×3 surface cell MoS_2 system (no tip) with one of the Mo atoms displaced 2.8au in the c direction (this is not quite in the plane of the surface sulphur, but corresponds to one of the atom displacements in the barrier calculations). The Mo atom and the third nearest-neighbour S atoms (to the vacancy site) were then fixed in position whilst all other atoms were allowed to fully relax. The tip was excluded from these calculations since the slight attraction of the tip to the surface would introduce some extra surface relaxation not accounted for in the barrier calculations. (Actually, full tip and surface relaxation starting from the tip and surface in their separate equilibrium structures resulted in a lowering in energy of only 10^{-4}au, but the effect would probably be larger when the surface Mo atom is displaced towards the tip). After atomic relaxation, the energy of the system had lowered by 0.339au (9.24eV). Figure D.3 shows the final structure—the sulphur atoms nearest the displaced Mo atom have moved

away from the atom in a symmetry conserving manner with the relaxation restricted largely to the sulphur plane.

D.4 Effects of Surface Charging and Electric Field on the Atom-Extraction Barrier

In Section 6.5.2 it was found that the electric field between the tip and sample is screened in the PAW calculations by charge transfer between the tip and sample. This charge transfer occurs because the Fermi levels of the tip and sample must be equal at static equilibrium and is the static limit of an electric current. The calculations presented here are intended to demonstrate that the charge transfer observed in the static calculations affects the atom-extraction barrier in a similar way to the presence of an electric field.

Here, the Mo-extraction barrier is considered for the Mo atom 2.8au from the Mo plane under several different situations. At this point the atom-extraction barrier is at its maximum value of 0.643au and 0.591au for the zero- and finite-field (including tip) calculations respectively. This is also the point at which the artificial peak occurs in the barrier owing to the lack of atomic relaxation in the calculations, but this is not important as it is only energy differences that are of concern here. This point was chosen as the influence of the tip was expected to be minimal, allowing the use of slab-only (no tip) calculations, but effect of the field on the barrier was maximal. By eliminating the tip from the calculation it is possible to look explicitly at the effects of both surface charging and electric field on the barrier, because they are no longer linked by charge-transfer from the tip.

The extraction barrier height with the Mo atom at $z_{\mathrm{Mo}} = 2.8$au was calculated under the following tip-free situations: i) Zero field; ii) Finite field (0.015au); iii) Zero field with charged slab (1 electron); iv) Finite field (0.015au)

Tip	Field	Charge	Barrier (au)
★	×	×	0.643
★	★	×	0.591
×	×	×	0.649
×	×	★	0.620
×	★	×	0.619
×	★	★	0.614

Table D.2: Calculated molybdenum-extraction barrier height with the Mo atom 2.8au from the Mo plane (*i.e.*, within the surface sulphur plane) under various situations. The ★ represents a feature present in the calculation, and the × represents a feature absent from the calculation.

with charged slab (1 electron). The charged slab calculations contained an extra electron per simulation cell, with the resulting infinite electrostatic energy removed by ignoring the $\mathbf{g} = 0$ component of the extra charge in the Ewald sum. The results of the calculations are shown in Table D.2 which also gives the barriers for the calculations including the tip for comparison.

The first thing to note about Table D.2 is that the barrier with a tip included is only 0.006au (0.16eV) lower then the tip-free barrier indicating that the tip effect on the barrier at this point is indeed small as required. The important point is that the barrier heights for both the charged (field free), and the finite-field (non-charged) calculations are essentially the same. Also, a combination of a charged slab and an applied electric field does not reduce the barrier significantly further.

In conclusion, the charge transfer effects seen when a field is applied to the atom-extraction simulations in Chapter 6 have a similar effect on the barrier to the presence of an electric field between the tip and the sample.

Appendix E

Acronyms

AE	All Electron (wavefunction)
APW	Augmented Plane Wave
BO	Born Oppenheimer (surface)
DFT	Density Functional Theory
CC	Constant Current (Mode)
CH	Constant Height (Mode)
CP	Car–Parrinello (Algorithm)
CITS	Current Imaging Scanning Tunnelling Spectroscopy
DoS	Density of States
EHTB	Extended Hückel Tight Binding
ES	Electrostatic (potential)
HOMO	Highest Occupied Molecular Orbital
KS	Kohn–Sham (equations/wavefunctions)
LAPW	Linear Augmented Plane Wave
LDA	Local Density Approximation
LUMO	Lowest Unoccupied Molecular Orbital

MD	Molecular Dynamics
PAW	Projector Augmented Wave
PS	Pseudo (wavefunction)
SPM	Scanning Probe Microscope/Microscopy
STM	Scanning Tunnelling Microscope/Microscopy
STS	Scanning Tunnelling Spectroscopy
TB	Tight-Binding
TH	Tersoff–Hamann (approximation)
TX_2	Transition-Metal (T) Dichalcogenide (X_2)
XC	Exchange–Correlation (energy)

Appendix F

Atomic Units

Unit	Atomic Units	SI equivalent
Charge	e	1.602177×10^{-19} C
Mass	m_e	9.109407×10^{-31} kg
Angular Momentum	$\hbar$	1.054597×10^{-34} Js
Length	a_0	5.291773×10^{-11} m
Energy	Ha	4.359757×10^{-18} J
Time	$\hbar$/Ha	2.418887×10^{-17} s

F.1 Useful Conversions

Length: 1 $a_0 = 0.529177$ Å

Electric field: 1 Ha/$a_0 = 51.4913$ V/Å

Energy: 1Ry = $\frac{1}{2}$Ha = 13.6eV

Bibliography

M. Allen, D. Tildesley. *Computer Simulation of Liquids.* Oxford, (1987).

A. Altibelli, C. Joachim, P. Sautet. *Surface Science*, 367, 209–220, (1996).

N. Ashcroft, N. Mermin. *Solid State Physics*, chapter 17, pp. 329–352. Saunders College Publishing, (1976a).

N. Ashcroft, N. Mermin. *Solid State Physics*, chapter 18, pp. 353–371. Saunders College Publishing, (1976b).

P. Avouris, R. Walkup, A. Rossi, H. Akpati, P. Nordlander, T. Shen, G. Abeln, J. Lyding. *Surface Science*, 363, 368–377, (1996).

G. B. Bachelet, D. R. Hamann, M. Schlüter. *Phys. Rev. B*, 26(8), 4199–4228, (1982).

J. Bardeen. *Phys. Rev. Lett.*, 6(2), 57–59, (1961).

L. Baskin, A. Drozdov, G. Vladimirov. *Surface Science*, 369, 386–392, (1996).

P. Beton, P. Moriarty, A. Dunn, Y.-R. Ma, M. Upward. Manipulation of molecules on semiconductor surfaces using a scanning tunnelling microscope. (1996). Presentation at CMMP 1996 Conference, University of York.

G. Binnig, H. Rohrer. *Reviews of Modern Physics*, 59(3), 615–625, (1987).

P. Blöchl. *Phys. Rev. B*, 50, 17953, (1994).

R. Car, M. Parrinello. In *Simple molecular systems at very high densities*, edited by A. Polian, P. Loubeyre, N. Boccara, pp. 455–476. Plenum Publishing Corp., (1989).

J. Caulfield, A. Fisher. *J. Phys.: Cond. Matter*, 9, 3671–3686, (1997).

D. Ceperley, B. Alder. *Phys. Rev. Lett.*, 45, 566, (1980).

C. Chen. *Phys. Rev. B*, 42(14), 8841–8857, (1990).

S. Ciraci, A. Baratoff, I. Batra. *Phys. Rev. B*, 42(12), 7618–7621, (1990).

M. Crommie, C. Lutz, D. Eigler, E. Heller. *Surface Science*, 362(1–3), 864–869, (1996).

A. Crossley, S. Myhra, C. Sofield. *Surface Science*, 318, 39–45, (1994).

W. Dawson, D. Bullet. *J. Phys. C: Solid State Phys.*, 20, 6159–6174, (1987).

E. Delawski, B. Parkinson. *J. Am. Chem. Soc.*, 114, 1661–1667, (1992).

G. Doyen. *Scanning Tunnelling Microscopy III*, chapter 3, pp. 23–50. Springer, 2nd edition, (1996).

D. Eigler, C. Lutz, W. Rudge. *Nature*, 352, 600–603, (1991).

D. Eigler, E. Schweizer. *Nature*, 344, 524–526, (1990).

P. Fleischauer. *Thin Solid Films*, 154, 309–322, (1987).

H. Fuchs. (1996). Private Communication.

H. Fuchs. 9th International Conference on Scanning Tunneling Microscopy/ Spectroscopy and Related Techniques, (1997). Private Discussion.

H. Fuchs, T. Schimmel, S. Akari, L. Eng, M. Anders, M. Lux-Steiner, K. Dransfield. In *Nanosources and Manipulation of Atoms Under High Fields and Temperatures: Applications*, pp. 293–309. Kluwer Academic Publishers, (1993).

H. Fuchs, T. Schimmel, M. Lux-Steiner, E. Bucher. *Ultramicroscopy*, 42–44, 1295–1302, (1992).

G. Galli. *Current Opinion in Solid State and Materials Science*, 1(6), 864–874, (1996).

J. Garnaes, S. Gould, P. Hansma, R. Coleman. *J. Vac. Sc. & Tech. B*, 9(2), 1032–1035, (1991).

R. Godby, M. Schlüter, L. Sham. *Phys. Rev. Lett.*, 56, 2415, (1986).

D. Goldhaber-Gordon, M. Montemerlo, J. Love, G. Opiteck, J. Ellenbogen. *Proc. of the IEEE*, 85(4), 521–540, (1997).

H. Goldstein. *Classical Mechanics.* Addison Wesley, (1950).

R. Gomer. *The Journal of Chemical Physics*, 31(2), 341–345, (1959).

R. Gomer, L. Swanson. *The Journal of Chemical Physics*, 38(7), 1613–1629, (1963).

O. Gunnarsson, I. Lundqvist. *Phys. Rev. B*, 13(10), 4274–4298, (1976).

M. Hara, Y. Iwakabe, K. Tochigi, H. Sasabe, A. Garito, A. Yamada. *Nature*, 344, 228–230, (1990).

V. Heine. *Solid State Physics*, 74, 1, (1970).

K. Hirose, M. Tsukada. *Phys. Rev. Lett.*, 73(1), 150–153, (1994).

P. Hohenberg, W. Kohn. *Phys. Rev.*, 136, B864, (1964).

S. Hosaka, S. Hosoki, T. Hasegawa, H. Koyanagi, T. Shintani, M. Miyamoto. *J. Vac. Sc. & Tech. B*, 13(6), 2813–2818, (1995).

S. Hosoki, S. Hosaka, T. Hasegawa. *Appl. Surf. Sci.*, 60/61, 643, (1992).

D. Huang, F. Grey, M. Aono. *Surface Science*, 331–333, 365–369, (1995).

R. Jones, O. Gunnarsson. *Reviews of Modern Physics*, 61(3), 689–746, (1989).

A. Kobayashi, F. Grey, E. Snyder, M. Aono. *Surf. Sci. Lett.*, 291, L739–L744, (1993).

K. Kobayashi. Theory of sub-surface structures observed in scanning tunneling microscopy. (1997). Poster presentation at 9th International Conference on Scanning Tunneling Microscopy/ Spectroscopy and Related Techniques, Hamburg.

K. Kobayashi, J. Yamauchi. *Phys. Rev. B*, 51, 17085–17095, (1995).

W. Kohn, L. Sham. *Phys. Rev.*, 140, A1133, (1965).

K. Laasonen, A. Pasquarello, R. Car, C. Lee, D. Vanderbilt. *Phys. Rev. B*, 47(16), 10142–10153, (1993).

R. Landauer. *IBM J. Res. Devolp.*, 1, 223, (1957).

N. Lang. *Phys. Rev. B*, 45(23), 13599–13606, (1992).

N. Lang. *Phys. Rev. B*, 49(3), 2067–2071, (1994).

D. Lawunmi, M. Payne. *J. Phys.: Cond. Matter*, 7(27), 5155–5162, (1995).

C. Lebreton, Z. Wang. *Scanning Microscopy*, 8(3), 441–448, (1994).

J. Leech, D. Newman. *How to use groups.* Science Paperbacks, (1969).

X. Li, W. Nunes, D. Vanderbilt. *Phys. Rev. B*, 47(16), 10891–10894, (1993).

C. Lieber, X. Wu. *Acc. Chem. Res.*, 24, 170–177, (1991a).

C. Lieber, X. Wu. *J. Vac. Sc. & Tech. B*, 9(2), 1044–1047, (1991b).

A. Livshits, A. Shluger. *Faraday Discuss.*, 106, (1997). To be published.

I. Lyo, P. Avouris. *Science*, 253, 173–176, (1991).

S. Magonov, M. Whangbo. *Adv. Mater.*, 5, 355–371, (1994).

H. Mamin, P. Guethner, D. Rugar. *Phys. Rev. Lett.*, 65(19), 2418–2421, (1990).

L. Mattheiss. *Phys. Rev. B*, 8(8), 3719–3740, (1973).

R. McWeeny. *Coulson's Valence.* 1979, (1979).

W. Mizutani, A. Ohi, M. MotoMatsu, H. Tokumoto. *App. Surf. Sci.*, 87–88(1–4), 398–404, (1995).

E. Müller, T. Tsong. *Field Ion Microscopy, Principles and Applications.* Elsevier, (1969).

H. Ness, A. Fisher. *Phys. Rev. B*, 55(15), 10081–10093, (1997a).

H. Ness, A. Fisher. *Phys. Rev. B*, (1997b). To appear in November issue.

D. Patrick, J. Victor, P. Thomas, J. Beebe. *Science*, 265, 231–234, (1994).

J. Pendry, A. Prêtre, B. Krutzen. *J. Phys.: Cond. Matter*, 3, 4313–4321, (1991).

J. Perdew, A. Zunger. *Phys. Rev. B*, 23(10), 5048–5079, (1981).

R. Pool. *Science*, 247, 634–636, (1990).

W. Press, B. Flannery, S. Teukolsky, W. Vettering. *Numerical Recipes.* Cambridge University Press, (1986).

J. Ryckaert, G. Ciccotti, H. Berendsen. *J. Comput. Phys.*, 23, 327, (1977).

G. Salam, M. Persson, R. Palmer. *Phys. Rev. B*, 49(15), 10655–10662, (1994).

A. Shluger, L. Kantorovich. *Phys. Rev. B*, (1997). Accepted for publication.

R. Superfine. The nanomanipulator. Talk at the 9th International Conference on Scanning Tunnelling Microscopy/ Spectroscopy and Related Techniques, Hamburg, (1997).

A. Sutton. *Electronic Structure of Materials.* Oxford, (1993).

A. Sutton, M. Finnis, D. Pettifor, Y. Ohta. *J. Phys. C: Solid State Phys.*, 21(1), 35–66, (1988).

J. Tersoff, D. Hamann. *Phys. Rev. B*, 31(2), 805–813, (1985).

T. Todorov, G. Briggs, A. Sutton. *J. Phys.: Cond. Matter*, 5(15), 2389–2406, (1993).

T. Tsong. *Phys. Rev. B*, 44(24), 13703–13710, (1991).

M. Tsukada, N. Shime. *J. Phys. Soc. Jap.*, 56(8), 2875–2885, (1987).

H. Uchida, D. Huang, F. Grey, M. Aono. *Phys. Rev. Lett.*, 70(13), 2040–2043, (1993).

D. Vanderbilt. *Phys. Rev. B*, 32, 8412, (1985).

D. Vanderbilt. *Phys. Rev. B*, 41(11), 7892–7895, (1990).

D. Vanderwalle, P. Blöchl. *Phys. Rev. B*, 47(8), 4244–4255, (1993).

VASP. Vienna *Ab-initio* Simulation Package, http://tph.tuwien.ac.at/~vasp. (1997).

R. Weisendanger. *Scanning Probe Microscopy and Spectroscopy.* Cambridge, (1994).

M. Whangbo, J. Ren, S. Magonov, H. Bengel, B. Parkinson, A. Suna. *Surface Science*, 326, 311–326, (1995).

M. Whangbo, J. Ren, S. Magonov, H. Bengel, B. Parkinson, A. Suna. *Surface Science*, 326, 311–326, (1995).